NEUTRON SCATTERING AND TRANSPORT STUDIES OF QUANTUM MATERIALS

By

Heda Zhang

A DISSERTATION

Submitted to
Michigan State University
in partial fulfillment of the requirements
for the degree of

Physics - Doctor of Philosophy

2022

ABSTRACT

NEUTRON SCATTERING AND TRANSPORT STUDIES OF QUANTUM MATERIALS

By

Heda Zhang

Quantum material is an multi-disciplinary research topic that continues to thrive in recent years. The term *Quantum material* covers all systems which demonstrate physical phenomena beyond the scope of single-particle, semi-classical/quantum theory. Among many sub-fields of quantum materials, topological systems and strongly correlated systems are two topics which have receive growing attention from the scientific community.

We begin with a discussion on a van der Waals magnet VI_3 in chapter three. VI_3 hosts ferromagnetism on a honeycomb lattice, which was one of the proposed models for topological magnon bands. There have been ample theoretical studies on ferromagnetic honeycomb lattice. However, there has not been any physical realization of such model. In our study, we show that the is a strong anomalous thermal Hall effect in VI_3, the underlying mechanism of which is the non-trivial topological nature of the magnon bands.

In chapter four, we discuss our transport studies on some magnetic topological metals. The non-zero Berry curvature in the reciprocal space of topological metals can lead to anomalous transverse conductivities $(\kappa^A, \sigma^A, \alpha^A)$ in the system. We found large anomalous transverse conductivities in $TbMn_6Sn_6$ and verified its intrinsic nature through first-principle calculations. Furthermore, we have found large exchange-bias behavior in $TbMn_6Sn_6$, which renders it as a promising system for anomalous Nernst effect based thermoelectric device. We will also discuss the topological Nernst effect observed in Fe_3Sn_2, which is potentially due to the Skyrmion bubble phase revealed by the Lorentz transmission electron microscopic studies.

In chapter five, we discuss our inelastic neutron scattering study on a unique quantum spin chain system in $Cu_2(OH)_3Br$. The system hosts alternating ferromagnetic and antiferromagnetic spin chains with finite inter-chain couplings. This allows for the coexistence and interactions between magnons and spinons.

TABLE OF CONTENTS

LIST OF TABLES

LIST OF FIGURES

Chapter 1

Introduction

This chapter contains an introduction to *quantum material* based on my research experience. The word quantum has been so widely used by not only researchers in the scientific community, but also people from all walks of life.[1] The reason behind its popularity is that quantum material is a very broad term, it can encapsulate the essential physics of many different fields of studies. The vague nature of this term made it impossible to define. When two researchers from different fields used the same phrase quantum material, they may be referring to completely different physical phenomena. However, the reason for their usage of the phrase is the same: to convey to the readers in a concise manner that there are new physics at play in the system. Therefore, the only important thing in dealing with *quantum materials* is to understand the underlying new physics discussed by the authors.

The quantum materials that will be discussed in this thesis can be cast into two main categories: strongly correlated systems and topological materials [7]. Atomic, molecular and optical systems will not be discussed in this thesis.

[1] Even Ponzi schemes have to do quantum nowadays, can you imagine, a quamtum Ponzi scheme

1.1 Strongly correlated systems

1.1.1 What is a strongly correlated system?

In condense matter physics, a physical system is composed of atoms assembled in certain geometric orders called *lattice*. The atoms are made of nuclei and electrons. The electrons surrounding the nuclei have different spatial density profile which are called *orbitals* (or electron clouds). An electron possesses both a *spin* of $\hbar/2$ and a *charge* of 1.6×10^{-19} coulombs (C). When considered in isolation, each of the four degrees of freedoms (lattice-spin-charge-orbital) of an atom may be understood using quantum mechanics. However, atoms in a physical system inevitably interacts with each other. The *correlated* here refers to correlations within and between these four degrees of freedom among atoms in a physical system. When this correlation becomes strong enough that a physical system starts to demonstrate behaviors beyond what known theory can explain, an adjective *strongly* is added in front. Collecting these concepts together, we arrive at a loose definition of strongly correlated systems from my perspective.

The reason I qualify the aforementioned definition with 'loose' is two-fold: first, I could not find a more strict definition which would also cover the entire body of work on the subject. Second, I could not find a single consensus on the definition of a strongly correlated system from existing literature. The same sentiment was expressed in a manuscript posted on arXiv in the year 2020 called *The Future of the Correlated Electron Problem*[2] [8]. In the manuscript, the authors wrote in the first paragraph of the first chapter:

[2] "This manuscript is the result of the vigorous discussions and deliberations that took place at Johns Hopkins University during a three-day workshop January 27, 28, and 29, 2020 that brought together six senior scientists and 46 more junior scientists."

> There is no consensus on the role of strong electron correlations in solids. Moreover, at present, there is no agreed single definition as to what constitutes the correlated electron problem. As such, for the purposes of this manuscript, we adopt the following working definition: *a correlated electron problem is one in which interactions are so strong or have a character such that theories based on the underlying original "bare" particles fail even qualitatively to describe the material properties.*

The authors here further explain what "beyond known theory" means: the breakdown of "bare', single particle physics. For example, the celebrated Fermi liquid theory fails to explain the metal-insulator transition in many transition metal oxides. To correctly predict the band structure of these systems, the electron-electron correlation effect (i.e., the Coulomb repulsion of d-electrons) needs to be taken into account.

1.1.2 High Tc superconductor

Although there is no consensus on the definition of strongly correlated systems, most condense matter researchers may agree that the discovery of high T_c superconductors in Ba-La-Cu-O system [9] provided strong motivations for the following theoretical and experimental investigations in the study of strongly correlated systems. Looking in hindsight, the exciting nature of this discovery is not simply that the T_c (superconducting temperature) is high, but that the highest T_c was found in such a 'dirty' system. Following simple physical intuitions, one would try to avoid introducing any scattering centers when searching for superconductors (e.g., lattice defects, magnetic impurities, etc.), as these scattering centers may prohibits the electrons from traversing freely through the system[3] and cause high electric resistance. As remarked by B. Keimer et al in [1]: "... *the copper oxides would have seemed the least*

[3]The Bardeen-Cooper-Schrieffer (BCS) theory explains superconductivity as the condensation of Cooper pairs at low temperatures, which was the most accepted explanation at the time. In this sense, superconductivity is a coherent quantum state and cannot be thought of as electrons traversing freely through the system with no scattering.

likely materials in which to look for superconductivity: at room temperature they are such poor conductors that they can hardly be classified as metals ...". The discovery forced researchers to break from the paradigm of the BCS-theory and pointed to the new direction of cuprates. Since then, cupartes with higher and higher superconducting temperatures have been gradually indentified (Figure 1.1), culminating in finding HgBaCaCuO system with T_c = 165 K[4] under pressure.

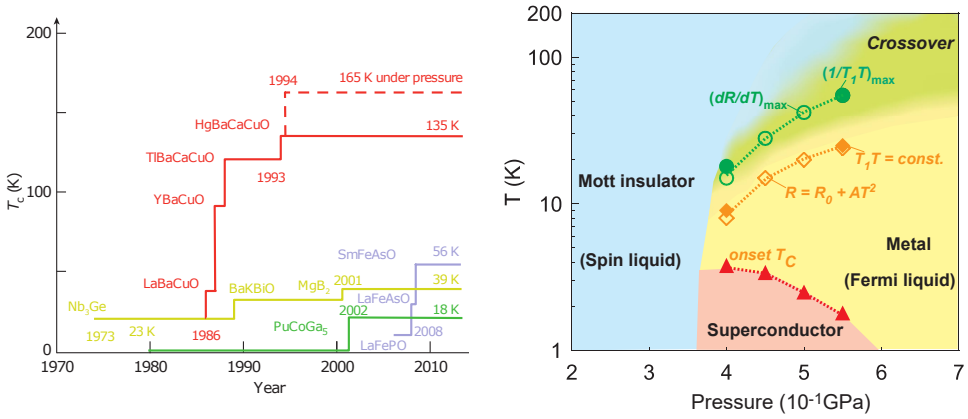

Figure 1.1: (Left)Development of superconducting temperatures over the years in different materilas. Addapted from [1]. (Right) Phase diagram of κ-$(ET)_2Cu_2(CN)_3$ under pressure. Adapted from [2].

After the discovery of cuprates, the importance of electron correlations has been gradually realized and accepted by the condense matter physics community. With electron correlations taken into account, we have seen even stranger tale of superconductivity in recent years. Unless you are a mad scientist, when trying to search for new superconductors, you should typically start with a conductor.[5] However, superconductivity was observed in an organic Mott insulator κ-$(ET)_2Cu_2(CN)_3$ under external pressure [2]. The pressure needed there

[4] "*Woah, We're halfway there; Woah, livin' on a prayer. - Mr. Bovine Joni*" - Frank Reynolds

[5] After all, the clue is in the name: a superconductor is a 'super' conductor. But as we shall see later, just like superman is not a 'super' man but an alien, an unconventional superconductor may be something of a completely different nature than a typical superconductor

was no more than 0.4 GPa, which is an incredibly small input for such a titanic response.[6] This, in fact, shows another characteristic of the strongly correlated systems, to which many researchers were drawn: that the simultaneously activation of the four degrees of freedom can result in complex energy landscapes, where many potential ground states may be in close proximity to each other. The implication of this is that when some parameters were tuned (e.g., temperature, field, pressure, chemical, etc), one may obtained a phase diagram such as the one on the right panel of Figure 1.1.

Although searching for superconductivity by simply tuning some parameters of a Mott insulator [10] may have seemed highly implausible, it was not without a supporting theory. In fact, the resonating valence bond (RVB) theory [11], which motivated the work on κ-$(ET)_2Cu_2(CN)_3$, predates the experiment by nearly two decades. The RVB theory was intended to explain the high-T_c superconductivity of La_2CuO_4, it caused a surging interests in another field of study called *quantum spin liquids* (QSL).[7]

1.1.3 Quantum spin liquids

What does 'liquid' in quantum spin liquid refer to? The 'liquid' here refers to a situation wherein a system of interacting spins does not develop magnetic long-range order ('solid'), even as the system temperature approaches absolute zero. Magnetic frustration plays an important role in preventing the onset of magnetic long-range order, but it is not the defining feature of a QSL. In recent years, more and more theoretical and experimental investigations on candidate QSL materials suggest that, a more appropriate description of QSL should be *a spin system whose ground state possesses long-range entanglement* [12].

[6] For reference, diamond anvil cells generally can reach between 10 GPa to over 100 GPa.

[7] In my opinion, quantum spin liquid can be considered as a sub-field of strongly correlated system, where the spin degree of freedom play the main role.

We begin our discussions with an isolated spin-1/2 system (Figure 1.2, left). In a spin-1/2 system, any spin wave function can be written as the superposition of two eigenstates $\{|\uparrow\rangle, |\downarrow\rangle\}$. In this way, one may obtain a geometrical interpretation of spin wave function in terms of a vector which can point to any direction on the globe.[8] Moving on to two spin-1/2 systems (Figure 1.2, middle). In this case, the eigenstates can be shown to be singlet $[(|\uparrow\downarrow\rangle - |\downarrow\uparrow\rangle)/\sqrt{2}]$ and triplet. I will not go into details about singlet/triplet but only point out that the singlet state is a maximally entangled state. Here, the concept of *entanglement* needs be introduced. Entanglement refers to the phenomenon when the state of a quantum mechanical system cannot be written as the direct product states of it constituting sub-systems.[9] This abstract concept can be quantified, for example by the Von Neumann entropy. However, we will take a more intuitive approach to see why the singlet state is maximally entangled. Imaging taking a single particle measurement of either of the spins in the singlet state, for any quantization axes (σ_x,σ_y,σ_z) chosen, the expectation value along that axis would have been zero. What this means is that there is no information to be gained by any single-particle measurement, and that all the information resides in the entanglement of the two spins in the singlet (i.e., they points to opposite directions). Finally, we consider a three-spin system with equal anti-ferromagnetic (AFM) Heisenberg interactions and discuss magnetic frustrations (Figure 1.2, right).[10] If we were given two known spins configured as shown, the spin on top would have been 'frustrated' in the sense that it could not find a preferred direction to point to, in order to lower the total energy.

[8] In my opinion, while the geometric interpretation makes for a good pedagogical analogy, it masks the peculiarity of superposition. For example, a spin which points to the equator is in fact pointing to both the north and the south pole instead. It is in a superposition state, to which we could find no classical analogy (you could not have the cake and eat it too). When we draw a vector pointing to the equator, we were given a very tangible and ordinary physical picture, when in fact the state to which it represents is highly intangible and extraordinary.

[9] From this definition, we immediately see that entanglement is impossible without superposition.

[10] I should add that the solution of triangular lattice AFM-Heisenberg model is the 120° configuration.

From this example, we see that magnetic frustration is one specific realization of the more abstract concept *degeneracy*.

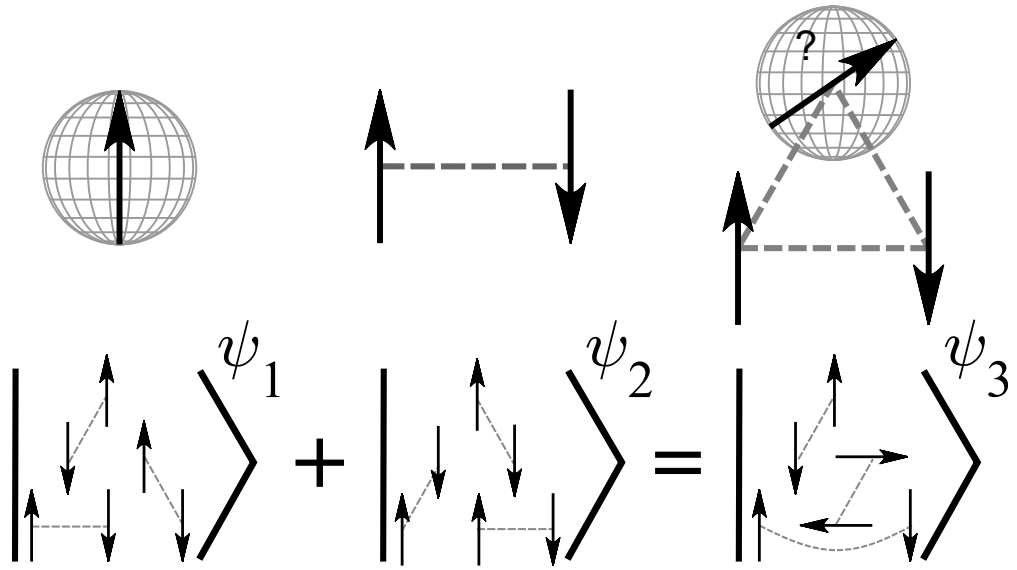

Figure 1.2: (Left) A single spin-1/2. (Middle) Two-spin system. (Right) Three-spin system with equal anti-ferromagnetic Heisenberg interactions. (Lower) Superposition of equally weighted ψ_1 and ψ_2 leads to ψ_3. One of the singlet in ψ_3 is separated by twice as before (ψ_1, ψ_2).

In microscopic systems, such degeneracy can be easily handled; However, in a physical system consisting of avogadro's number of particles, the proliferation of ground state degeneracy to a macroscopic level could lead to long-range entanglement and novel quasiparticles. To see this, consider the example (triangular lattice) shown as the bottom row of Figure 1.2. Two degenerate ground state ψ_1 and ψ_2 with 3 pairs of spin-singlets[11] (indicated by the gray dashline) were show, the superposition with equally weighted ψ_1 and ψ_2 is also a ground state (ψ_3). However, the entanglement has now grown in dimensions: a pair of singlet is now separated by twice the lattice constant. While the example here is only for a 9-spin system, it is not a hard exercise to see that the same principle could work for lattices of any size.

[11] Although I have drawn arrows here to represent the spin direction, we should recall from our previous discussion that singlet is a maximally entangled state and each individual spin points to no definitive direction.

This is the essential idea of resonating valence bond (RVB) theory, that the superposition of a highly degenerate ground states set could lead to entangled spin singlets separated by macroscopic distance.

An exact solvable model of QSL can be found in the celebrated Kitaev model [3]. The model consists of spins (S=1/2) on a honeycomb lattice with nearest neighbor anisotropic exchange-interactions (Figure 1.3). To understand the Kitaev model, we first note that a plaquette operator $W_p = \sigma_1^x \sigma_2^y \sigma_3^z \sigma_4^x \sigma_5^y \sigma_6^z$ takes on value of ± 1, commutes with each other and the Hamiltonian. Therefore, eigenstates of the Hamiltonian can be labeled by the locally conserved 'flux' through each plaquette. A plaquette with $W_p = -1$ is a 'vortex', and the ground state is the superposition of any spin configurations which are vortex-free[12] [3]. The spin Hamiltonian can be re-written in a form consisting of 4 Majorana operators: three of which are immobile ($b_j^{\gamma=x,y,z}$) and control the phase gain while the itinerant (c_j) one hops through that bond. A Majorana fermion is a fermion that is its own antiparticle. The dispersion relation for the itinerant Majorana fermion was $\epsilon(\vec{q}) = 2|K^x e^{iq_1 \cdot n_a} + K^y e^{iq_2 \cdot n_b} + K^z|$, which become gapless at K-pionts. Entanglement is a strange concept because of its implication of non-localilty. It is interesting to consider the creation of a long-range entangled spin pair as depicted in Figure 1.3. In the Kitave model, entanglement between the spin pair does not need to rely on 'action at a distance'; Instead, the entanglement is the result of a path operator (local at each lattice site) which connects the entangled spin pair. The spectrum for a more general gapped phase and non-Abelian Anyons[13] of the Kitave model has been discussed in length in [3]. I should not need to further belabor the rich physics

[12] An alternative description of the ground state is the superposition of the classical spin configurations shown as red, blue and green. The idea is very similar to the RVB model.

[13] Fermions and bosons are both Abelian, in that the exchange of two identical particles leads to a phase shift of π (Fermions) and 2π (Bosons) in the total wave function. For a non-Abelian Anyon, the phase shift of the total wave function can take on any value between 0 and 2π.

behind this deceivingly simple model [3, 13, 14].

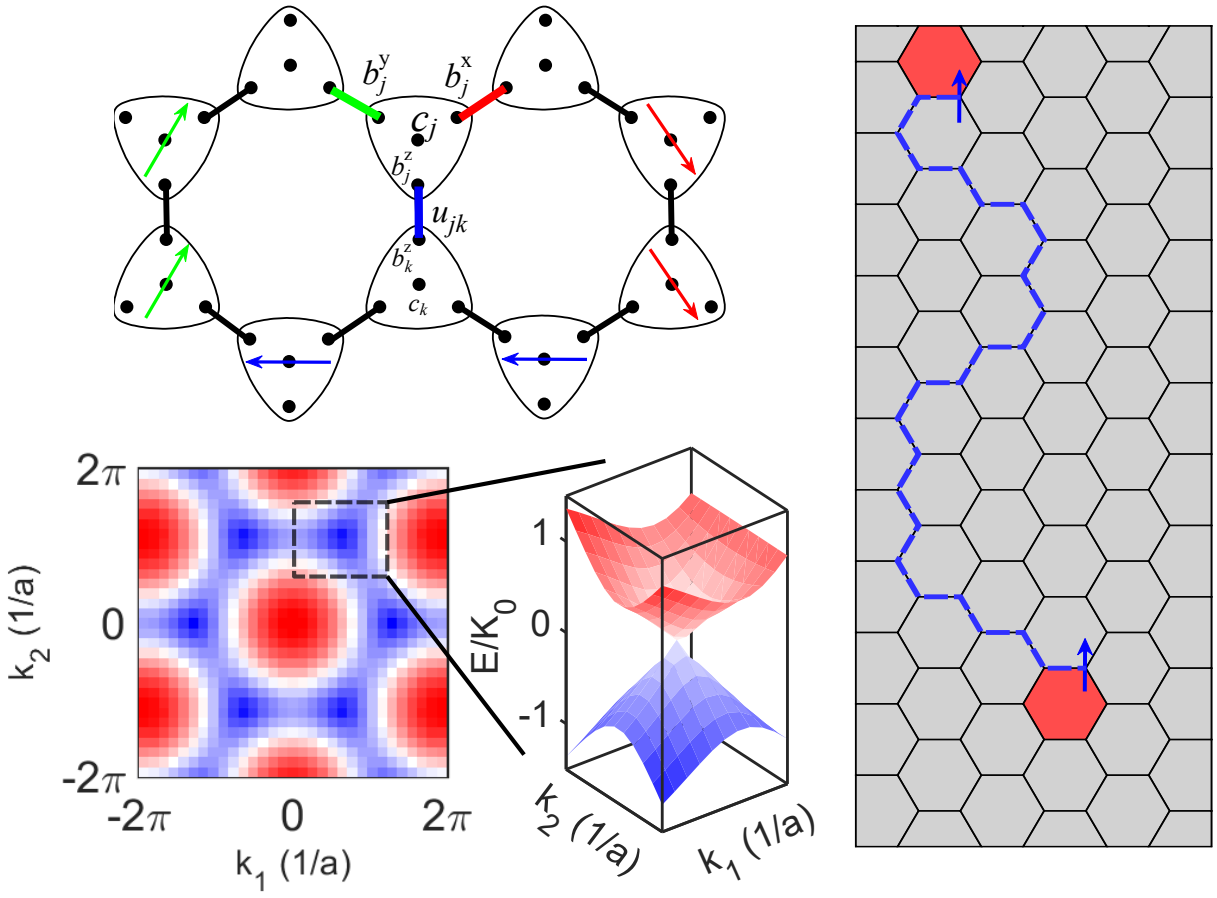

Figure 1.3: (Left, upper) A graphical representation of the Kitave model, modified from Figure 4 in [3]. The spin is fractionalized into four Majorana fermion. (Left, lower) Pseudocolor plot of the Band gap for $K^x = K^y = K^z = K_0$. A zoom in view of the Dirac-like dispersion near one of the K-points. (Right) Creation of a long-range entangled spin pair through the path indicated by blue dash line. Two vortices (red) were created.

1.2 Topological materials

1.2.1 What is topology?

Like many young researchers drawn to the concept of topological insulators (TIs), my first attempt to understand the topic was to read the review paper by M. Z. Hasan and C. L.

Kane [7]. At the beginning of this paper, a picture of an orange and a donut[14] was shown to illustrate the concept of topology. However, this was not the 'answer' to what I was hopping for: I can see that there are different numbers of holes in them, but how do I make the connection between 'holes' to *non-trivial band topology*?

To see the connection, we must first understand Topology on an elementary level. We begin by introducing *manifolds*: a topological space that locally resembles Euclidean space near each point.[15] For example, a piece of (infinitely thin) A4 paper is a 2D-manifold; And just like we can artistically fold a piece of paper into a swan or a frog (origami), we can continuously deform a manifold into almost any other manifolds. A question we can ask is: can we classify manifolds into different groups, such that manifolds within one group can be continuously deformed into each other , but not to manifolds outside the group?[16] One such way to categorize manifolds was by using the genus[17] (g) as the index for different groups. A more formal way to calculate the genus of a surface than 'counting the number of holes', was by integrating the Guassian curvature (K) over the surface.[18] The genus is a topological invariant: its value will remain the same during any deformations which does not change the compactness of the surface.

Returning to the context of condense matter physics: we can use the Berry curvature,

[14]During the Nobel Prize announcement event, a cinnamon bun, a donut and a pretzel were used to demonstrate the concept of topology... but I believe they were just too hungry.

[15]To get a sense of manifolds, consider the following: a circle is a 1D-manifold, a Lemniscate (∞) is not a manifold but a Mobius strip is a 2D-manifold.

[16]The task description here clearly indicates that this is a task for group theory. In fact, there have been efforts of high-throughput calculations using symmetry-indicators to identify new topological materials. It is very helpful to get a basic understand of group theory in CMP by reading the textbook: *Applications of Group Theory to the Physics of Solids* [15]. I particularly recommend the lecture notes by Daniel Arovas [16] for both deeper knowledge and some great jokes. (As written in the preface: "These lecture notes are intended to supplement a graduate level course in group theory applied to condensed matter physics. Or one can skip all the math and just read the jokes.")

[17]Technically, the genus is defined for a connected, orientable surface.

[18]They are related through the Gaussian-Bonnet theorem for a closed surface, $\int_S K = 4\pi(1-g)$

integrated over the first Brillouin zone as an index, to categorize different insulators into trivial and topological groups. The integrated value scaled by a factor of $1/2\pi$ is the Chern number, which always takes on integer value. We discuss the application of this topological invariant by studying its application on the Haldane model.

1.2.2 Berry curvature and Haldane model

The adiabatic theorem [17] states that, a system will remain in its instantaneous eigenstates (up to a phase), if the process is slow enough and does not admit any eigenstates mixing. Applying this theorem to a system whose Hamiltonian depends on some external parameters $H(\vec{p})$, we see that there can be a phase shift after an adiabatic evolution along a close path C in the parameter space. The phase shift between the initial and final state is the Berry's phase [18]. The concept can be generalized to Berry potential/connection $A(\vec{p}) = \langle u(\vec{p})| \, i\nabla \, |u(\vec{p})\rangle$. The curvature of Berry potential $\Omega = \nabla \times A(\vec{p})$ is the Berry curvature. The advantage of introducing Berry potential and curvature is that we can write them as scalar and vector fields in the parameter space, without the need to consider any specific loops or path. We can directly visualize these concepts by studying the Haldane model [19].

The Haldane model is a two-dimensional tight-binding model on a Honeycomb lattice (Figure 1.4, upper left). The Hamiltonian matrix writes $H(\vec{k}) = \begin{bmatrix} u & h \\ h^* & -u \end{bmatrix}$, where $h = 2t_1 * \sum_j e^{i\vec{k}\cdot\vec{a_j}}$ and $u = M + 2t_2 * \sum_j sin(\vec{k}\cdot\vec{b_j})$. By solving the eigenvalue problem $det|H - \lambda I| = \begin{vmatrix} u-\lambda & h \\ h^* & -u-\lambda \end{vmatrix} = 0$, we obtain the spectrum $\lambda = \pm\sqrt{|h|^2 + u^2}$. When u = 0, the spectrum reaches its maximum value at Γ and become gapless at K. A dispersion along $K - \Gamma - K$ and a contour map of the spectrum are shown in Figure 1.4 (upper, middle). We further

consider two ways of gapping out the model Hamiltonian to obtain an 'insulator'. The first way was to add a site specific potential energy $\pm M$, and the second way was to add an imaginary hopping energy (it_2) between second-nearest neighbors, whose sign depends on the hopping direction. Either method would produce a gap at K points, thereby ensuring that no eigenstates mixing would be allowed within the Brillouin zone. We can calculate the Berry potential and its curvature. The lower panel of Figure 1.4 shows the numerical results for the upper band (E>0). The black arrow represents the vector field of Berry potential $A(\vec{k})$, the pseudo-color map represents the Berry curvature $\Omega(\vec{k})$, both of which have been multiplied by a k-dependent scaling factor $|\lambda|\sqrt{(|h|^2+(|\lambda|+u)^2)(|h|^2+(|\lambda|-u)^2)}$.[19]

For the case of M = $0.1t_1$, $t_2 = 0$ (Figure 1.4, lower left), two types of vortices with opposite curling directions emerge near K-points. The Chern number for this 'insulator' phase is C = 0 (i.e., a trivial insulator). If we add in the second-nearest neighbor imaginary hopping integral t_2=$0.1t_1$, only one type of vortex arise (Figure 1.4, lower right), and the corresponding Chern number (for the positive energy branch) is +1. The model can be further generalized by allowing the second-nearest neighbor hopping integral to have arbitrary phase: $t_2 * e^{i\phi}$. The Chern number (C) is a topological invariant, in the sense that it does not vary continuously with changing M, t_2 or ϕ. As shown in the phase diagram from [19]: ϕ will control boundary between trivial and topological phase and there does not exist any intermediate value for the Chern number.

Up to this point, we have seen the analogy between band topology and 'mathematical' topology. They both feature a topological invariant which remains a constant during smooth transformations. We have not seen any connection between the topological invariant to

[19]This is done because the magnitude of Berry potential/curvature increase drastically near the smallest band gap points. Without the scaling factor, the plots in Figure 1.4 will be strongly emphasized only near each of the K-points.

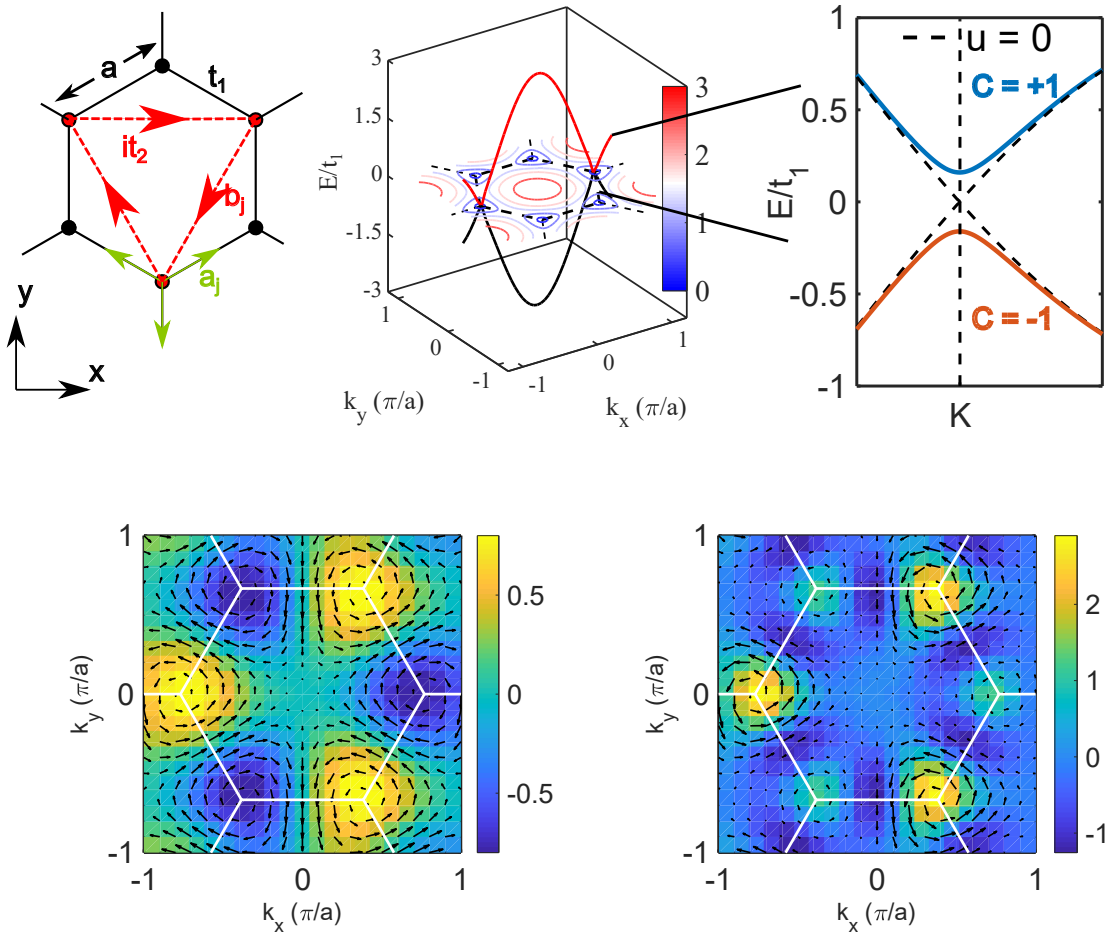

Figure 1.4: (Upper, left) A honeycomb lattice with lattice spacing denoted by a. (Upper, middle) Dispersion along $K-\Gamma-K$ and a contour map of the dispersion for the Hamiltonian H with u = 0. Berry potential $A(\vec{k})$ and the corresponding Berry curvature $\Omega(\vec{k})$ (scaled) for M = $0.1t_1$, $t_2 = 0$(Lower, left) and for M = $0.1t_1$, $t_2 = 0.1t_1$ (Lower, right).

anomalous transport phenomena. While an orange and a donut have different genus, there is no physical implication for this difference. In condense matter physics, the bulk-boundary correspondence dictates that there must exist a chiral edge state between two gapped bands with different topological invariants. For the Haldane model with $|M| < 3\sqrt{3}|t_2 sin(\phi)|$, the valence and conduction band has opposite C and a chiral edge state connecting them. The opposite situation is found for the case of $|M| > 3\sqrt{3}|t_2|sin(\phi)$. The existence of such chiral edge state is why an insulator with C = 0 is trivial, but an insulator with $C \neq 0$ is topological.

1.2.3 Berry curvature and anomalous transport

Berry curvature also plays an essential role in anomalous transports. Using the Kubo formula, it was found that electrons acquire an 'anomalous velocity' (perpendicular to electric field) due to the presence of non-zero Berry curvature. As such, the Berry curvature acts like an synthetic gauge field[20] in the reciprocal space. As an extreme case demonstration (for example, the TaAs system), this synthetic gauge field permits the existence of pairs of monopoles and anti-monopoles called Weyl points.[21] Surface state called fermi arcs connects Weyl points of opposite chirality and has been experimentally observed (see Figure 1.5).

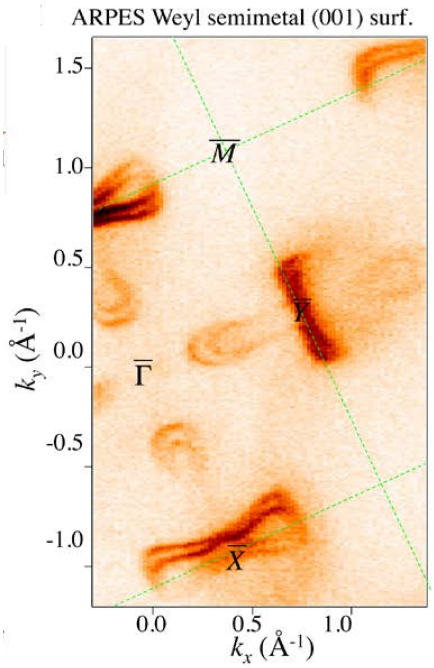

Figure 1.5: Fermi arcs of a Weyl semimetal TaAs observed by Angle Resolved Photoemission Spectroscopy [4].

[20] The Berry potential/curvature are related as $\Omega = \nabla \times A$. The Berry curvature interacts with an electron through $v \times \Omega$. For anomalous transport studies, the Berry curvature is a synthetic gauge field which acts as if it were a 'magnetic' field.

[21] It should be noted that the divergence of any curl field is identically zero, i.e. $\nabla \cdot (\nabla \times A) = 0$. For the case of Weyl physics, the Berry curvature is directly calculated from Berry phase, rather than Berry connection, which is shown to be $|\Omega| = \frac{\vec{k}}{|k|^3}$.

1.3 The scope of this thesis and beyond

The thesis - An introduction to the general theme of this paper, i.e. quantum materials is given in chapter one. Relevant experimental techniques used in this thesis (and related published papers) are discussed in chapter two. In chapter three, we introduce our work on a van der Waals ferromagnet VI_3 [6]. Transport data and theoretical calculations of two magnetic topological metals ($TbMn_6Sn_6$ [20], Fe_3Sn_2 [21]) are discussed in chapter four. Finally, the inelastic neutron scattering experiment results on a unique quantum spin chain system $Cu_2(OH)_3Br$ [22] is presented in chapter five. For future students of our lab, a manual for the transport measurement software can be found in chapter six.

Beyond this thesis - Not all original studies I carried out during my graduate research life has been included in this thesis. For example, we discuss our inelastic neutron scattering results and the relevant magnon band topology of YMn_6Sn_6 in [23]. We discuss the giant anomalous Hall effect observed of a magnetic half-Heusler metal DyPtBi in [24]. Detail discussion on these projects can be found in the published manuscripts.

Chapter 2

Experimental techniques

This chapter contains detailed information regarding the experimental techniques that I used during my time as a graduate student. There are two main sections: transport characterization and neutron scattering. The focus will be on the thermal and thermoelectric measurement system.

2.1 Transport measurements

A transport measurement quantifies the response of a system to an external drive. For example, an electrical resistance measurement quantifies the voltage drop across a system per unit current. These responses allow us to infer some physical properties of the system. Anomalous transport behavior refers to the situation wherein the system develops a response perpendicular to the direction along which the drive is applied. As discussed in chapter one, such anomalous response allows us to infer information regarding the Berry phase in the system's band structure.

2.1.1 Transport coefficients definitions

We begin by defining the transport coefficients. For an electrical measurement, we measure the resistance and Hall resistance of a material. The resistance is defined as $R_{xx} = \frac{V_2 - V_1}{I}$,

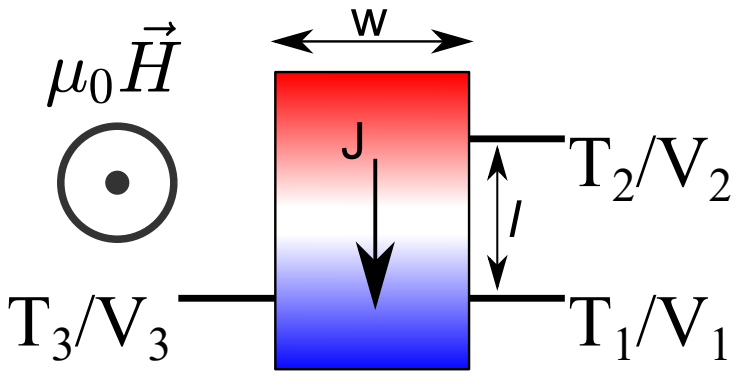

Figure 2.1: The sign conventions I adopted for my thermal and thermoelectric transport measurements.

and the Hall resistance is defined as $R_{xy} = -\frac{V_3 - V_1}{I}$, where I is the current passing through the sample. The resistivity ($\bar{\rho}$) are calculated by $R_{xx} = \frac{l}{wt} * \rho_{xx}$, $\rho_{yx} = -t * R_{xy}$, and the conductivity ($\bar{\sigma}$) by $\sigma_{xx} = \frac{\rho_{xx}}{\rho_{xx}^2 + \rho_{yx}^2} \approx \rho_{xx}^{-1}$, $\sigma_{xy} = \frac{\rho_{yx}}{\rho_{xx}^2 + \rho_{yx}^2}$, where t is the sample thickness. For a thermal measurement, the definition is identical to the electrical measurements through a simple mapping analogy: $\{V(voltage) \rightarrow T(temperature),\ I(current) \rightarrow P(power),\ \rho(resistivity) \rightarrow w(thermal\ resistivity),\ \sigma(conductivity) \rightarrow \kappa(thermal\ conductivity)\}$. For a thermoelectric measurement, we measure the Seebeck (S_{xx}) and Nernst (S_{xy}) coefficients of a material. The Seebeck coefficient is obtained by $S_{xx} = -\frac{V_2 - V_1}{T_2 - T_1}$. The Nernst coefficient is obtained by $S_{xy} = \frac{(V_3 - V_1)/w}{(T_2 - T_1)/l}$.

2.1.2 Hardware

Table 2.1 lists the Hardware for our transport measurements. The Physical Property Measurement System (PPMS) is a commercially available cryostat. We use the PPMS chamber to obtain the desired temperature and magnetic field for our measurements. The software to control PPMS was provided to us. Third-party control of the PPMS system is very simple:

Physical Property Measurement System (PPMS)
Resistivity option (PPMS)
Keithley 2182A nanovolt meter
Keithley 6220 current source
Keithley DMM6500 multimeter
Type-E thermocouple (chromel-constantan)
Cernox (CX-1070)

Table 2.1: A list of hardware necessary for transport measurements.

one can use the .vi files from Quantum design, or use the SCPI[1] commands directly.

The Keithley 2182A nanovolt meters were used to measure voltage signals. This meter has very good performance, with noise level typically at 5 nV to 10 nV. The Keithley 6220 current source was used to generate a current through a resistive heater during the measurement.[2] The Keithley DMM6500 multimeter was used to read out voltage drop across the resistive heater during thermal/thermoelectric measurements.

We use two types of thermometer for our measurements depending on the temperature range we aim to cover. We use Cernox for low temperature region (2 K - 150 K) and type-E thermocouple for high temperature region (20 K to 400 K).

2.1.3 Software

The hardware were controlled by a Labview project called TTO_v2. A typical user would only need to access the *maine.vi* program to take measurements. A manual of TTO_v2 is

[1] Standard Commands for Programmable Instruments

[2] In retrospect, this meter has far superior performance than necessary.

included in chapter six.

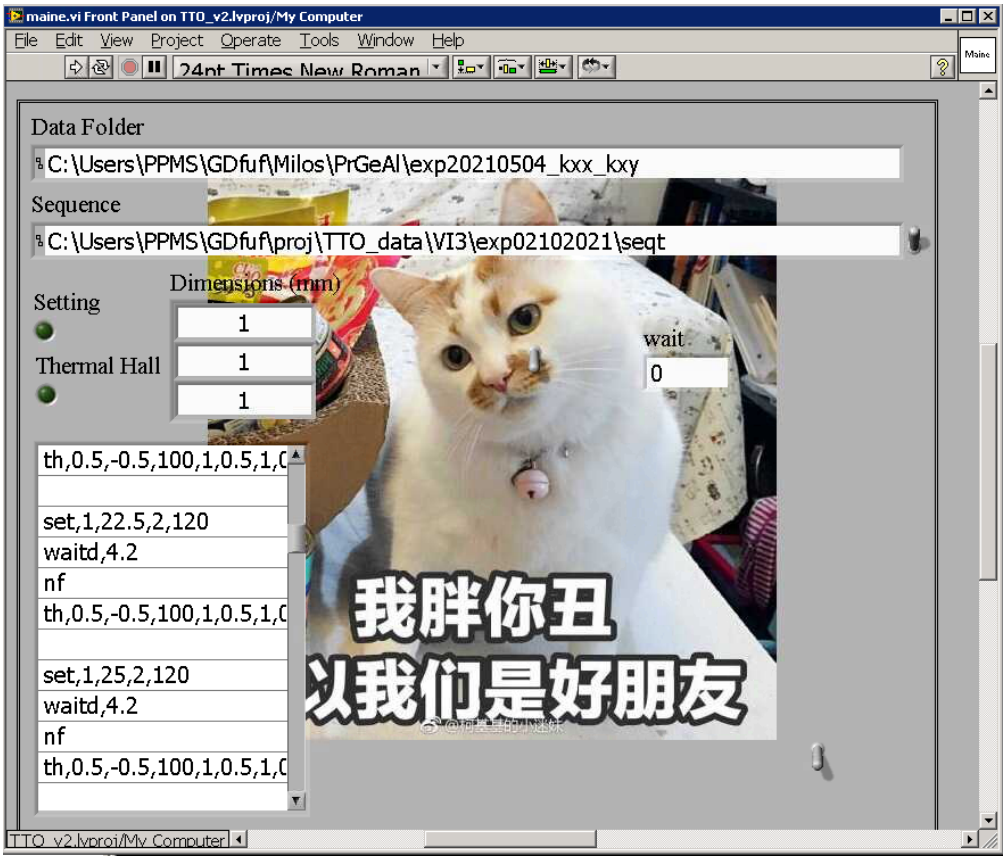

Figure 2.2: The front panel of *maine.vi*.

2.1.4 Radiation correction

During thermal conductivity measurements, the black body radiation may become an issue and needs to be calibrated. As an example, the figure on the right shows the thermal conductivity (κ) of $Fe_{3-x}GeTe_2$. The red and blue curves show clear bifurcation beginning at 100 K. The black body radiation follows $P \propto A\epsilon T^4$, where P is the radiating power, A is the surface area of a sample, and ϵ is a material dependent emissivity constant ($0 < \epsilon < 1$). During the experiment, the sample's temperature [defined as $T = (T_1 + T_2)/2$] is elevated to a higher value than the environment. The power loss through radiation would be

$P_{loss} = CT^3(T_{samp} - T_{env}) = CT^3\Delta T$, where C is a experiment dependent constant. Given the cubic proportionality between radiation power loss and temperature, we can carry out a calibration routine to infer the material dependent constant C. After a thermal conductivity measurement experiment, we keep every contacts on the sample except the connection to the heat sink. The puck was then put back into the chamber for calibration process: from 250 K to 300 K at 10 K step size, a constant heating power P_{heat} was applied to the sample.[3] After the sample temperature stablized (this can take several minutes), the temperature rise ΔT was then recorded.

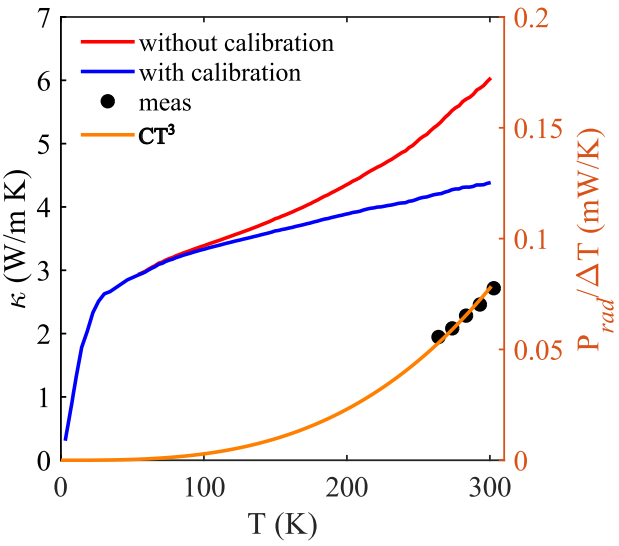

Figure 2.3: Radiation correction for thermal measurements. Blue and red curves showed the corrected and uncorrected data.

Note that at this point, it was only an assumption that the majority of the heating power was dissipated through radiation channel ($P_{heat} = P_{loss}$), rather than through the wires connected to the sample. We then plot the $P_{heat}/\Delta T$ as a function of temperature (black dots) and fit the measured data by a cubic function (CT^3, orange curve). If a good fit can be obtained, the assumption holds true. We extract the constant C and subtract out

[3] I usually manually chose a power which raise the sample temperature by 10 K.

a component from the total applied power using $P_{act} = P_{tot} - CT^3$. This constant C needs to be obtained for each experiment.

As a final remark, it is only necessary for a radiation calibration if the sample being measured is extremely thin and the thermal conductivity of the sample is relatively low. For a bar shape sample, the relative importance of $P_{loss}/P_{tot} \propto 1/t$, where t is the sample thickness. So the thinner a sample is, the more prominent radiation effect will become. Secondly, if the thermal conductivity of a sample is high, a large total power can propagate through the sample to the sink without substantially heating up the sample. In this case, the relative importance of radiation heat loss can also be omitted.

2.1.5 Thermal Hall effect measurement

The thermal Hall effect (THE) of insulating compounds is one of the most challenging transport measurements. The thermal Hall effect is the thermal counterpart of Hall effect. It refers to the production of a temperature difference ($\Delta T_{yx}//\vec{e}_y$) perpendicular to the heat current direction ($\vec{J}//\vec{e}_x$) in the presence of a magnetic field ($\vec{H}//\vec{e}_z$). The difficulty is mainly due to ΔT_{yx} being a very weak signal. Consider an illustration as shown in section 2.1.1. While T_1 and T_3 appear to be exactly perpendicular to the heat current direction in the schematic, this is impossible to achieve in a real experiment device. This means that the measured $\Delta T_{yx} = T_3 - T_1$ actually contains two components, i.e. $\Delta T_{yx} = \delta T_{yx} + \delta T_{xx}$. The δT_{yx} is the intrinsic signal we wish to measure, and the δT_{xx} is a component along the heat current direction we wish to separate out. For the magnetic materials that we are interested in, a method for separating these two components is available.

As an example, the figure on the right shows our data taken on $FeCl_2$. The longitudinal and transverse thermal resistivity ($w_{xx} = \frac{\Delta T_{xx}}{P}\frac{wt}{l} = \frac{T_2 - T_1}{P}\frac{wt}{l}$, $w_{xy} = \frac{\Delta T_{xy}}{P}t = \frac{T_3 - T_1}{P}t$)

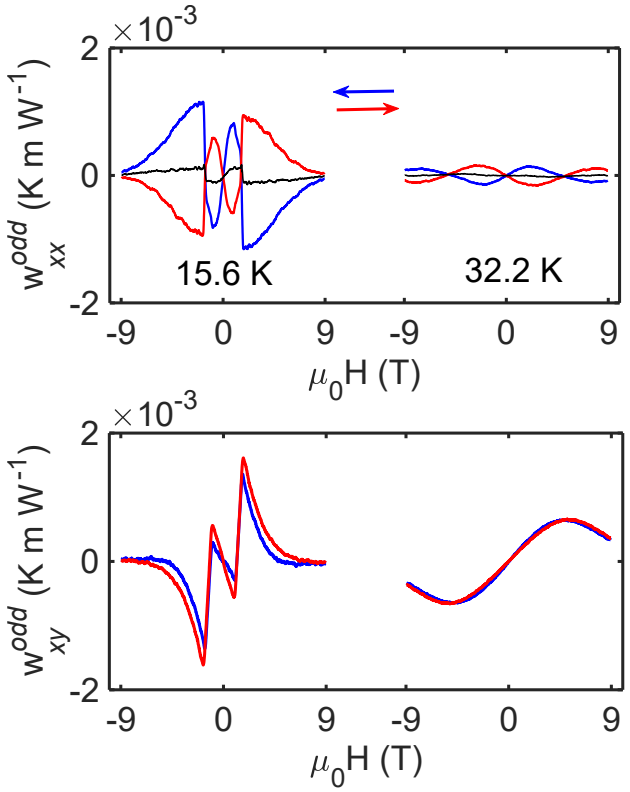

Figure 2.4: The hysteresis effect during a thermal Hall measurements on a piece of $FeCl_2$ sample.

data were collected during two field sweeps: {9 T → -9 T, -9 T → 9 T }. The sweeping directions were indicated by blue and red colors. In principle, we expect the intrinsic signal δT_{xy} to be odd with respect to the field direction $[\delta T_{xy}(H) = -\delta T_{xy}(-H)]$. We plot the odd components of $w_{xx}^{odd} = w_{xx}(H) - w_{xx}(-H)$ and $w_{xy}^{odd} = w_{xy}(H) - w_{xy}(-H)$ as the upper and lower panels in Figure 2.4. From the lower panel, we see that the signal in w_{xy} channel is largely dominated by an odd component. However, from the upper panel, we see that there is also an odd component in the w_{xx} channel. What this implies is that we could not simply take the odd component in w_{xy} as the intrinsic thermal Hall signal. A second observation we can make is by comparing the hysteresis behavior of this odd component in the longitudinal and transverse channels. By averaging the odd components of w_{xx} during a field ramp-up and ramp-down curve, we obtained the black curves shown in the upper panel.

We see that by this procedure, we can get rid of the major part of the odd component in the w_{xx} channel. Therefore, we can apply this method to the w_{xy} channel, by averaging the w_{xy}^{odd} during a field ramp-up and ramp-down process.

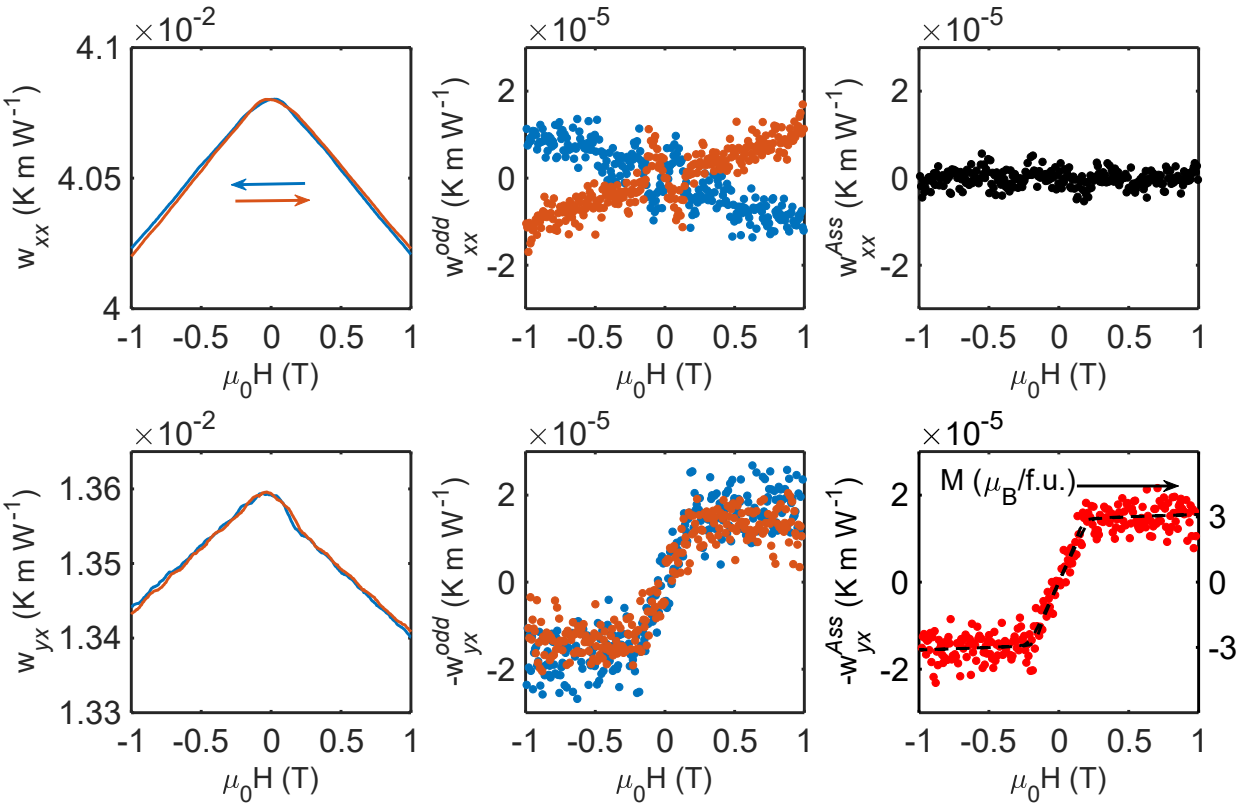

Figure 2.5: Anti-symmetry process for obtaining the intrinsic anomalous thermal Hall effect.

Why does this procedure matter? The left column in Figure 2.5 shows the raw data recorded during a measurement on CrI_3. While we can see the asymmetric feature from w_{yx} data if we squint at the curves, one may inevitably question the 'intrinsic' nature of this signal. For example, the middle column shows the odd component of the raw data. If we only measure them during field ramps from -1 T to 1 T (i.e., we only have the orange curve), I would seriously doubt the measured signal of $-w_{yx}^{odd}$, since there may be some unwanted signal due to misalignment of temperature leads. However, if we carry out the aforementioned procedure, the resulted signal w^{Ass} were shown in the right column, which

gave us much more confidence in the intrinsic nature of the thermal Hall signal.

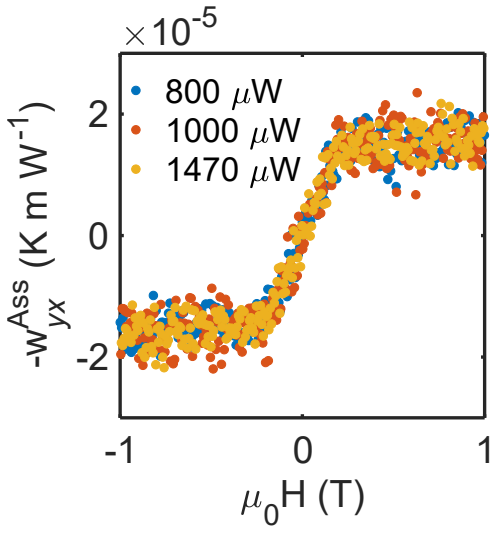

Figure 2.6: Effect of applied power on thermal Hall conductivity. The intrinsic thermal Hall effect should be independent of applied power.

Another test that we routinely carry out to verify the intrinsic nature of the thermal Hall signal was a power test. In principle, we expect the thermal Hall resitivity $w_{yx} = \frac{\Delta T_{yx}}{P} t$ to not depend on the applied power. A power test at T = 20 K for CrI_3 is shown in Figure 2.6. We see that the $-w_{yx}^{Ass}$ signal is independent of the applied power.

2.2 Neutron scattering

Neutron is a charge neutral particle with S = 1/2. Neutrons can interact with a system and the quasi-particle excitations in the system through scattering. Such scattering experiments allow one to infer information on the structural, magnetic and dynamical properties of a system. Different experimental techniques covers different length, time and energy scales where interesting physical phenomena could take place, as shown by the following figure[4]. In this thesis, we focus on neutron scattering and inelastic neutron scattering.

[4]https://europeanspallationsource.se/science-using-neutrons

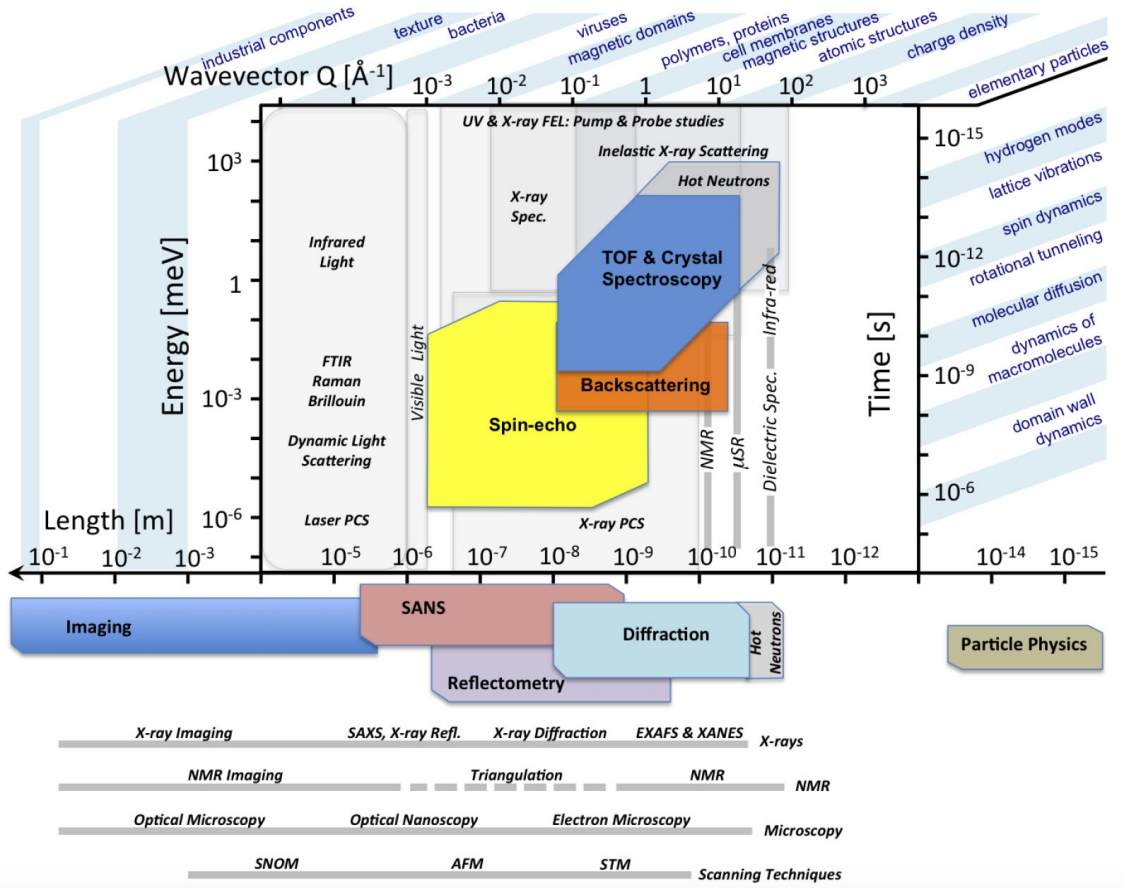

Figure 2.7: A figure summarizing the different scale of physical phenomena neutron scattering can study.

2.2.1 Neutron diffraction

In a neutron diffraction experiment, a beam of neutron with wavelength λ is guided to shine on the sample. Neutrons are then scattered off by the nuclei and the electrons' spins. The underlying principle for a neutron diffraction experiment is the well-known Bragg's law. When the neutron wavelength, lattice spacing and the diffraction angle satisfy the relation: $n\lambda = 2dsin(\theta)$, the scattered waves (neutrons) interferes with each other constructively. The result is a strong peak in the diffracted intensity, called Bragg peaks. Since neutron carries a magnetic moment, there will also be Bragg peaks due to the magnetic lattice. We can solve the magnetic structure of a material by refining these magnetic Bragg peaks.

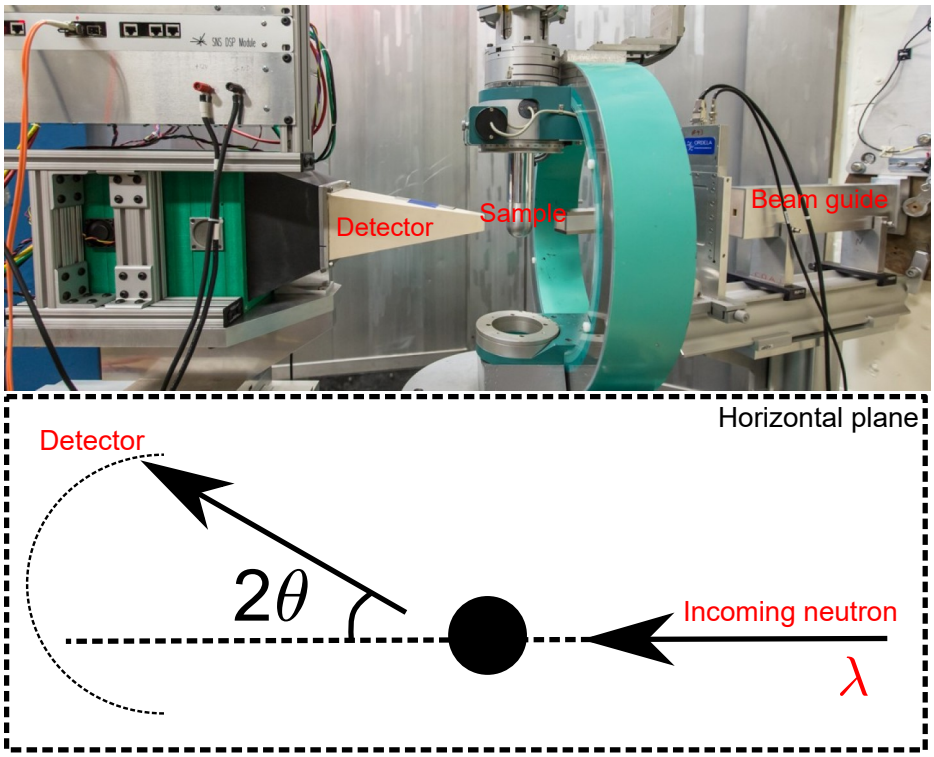

Figure 2.8: The Dimensional Extreme Magnetic Neutron Diffractometer.

Figure 2.8 shows a photo of the neutron diffractometer DEMAND[5] at Oak Ridge National Lab (ORNL). The instrument mainly consists of incoming beam guide, a sample holder and an area detector. We can cover different θ by rotating the detector, and cover different Bragg peaks (with different lattice spacing d) by rotating the sample. A schematic of the scattering plane (horizontal plane in this case) is also shown.

2.2.2 Inelastic neutron scattering

In an inelastic neutron scattering experiment, a beam of neutron with incident momentum and energy $(\vec{q}_i, E_i)$ is guided to shine on a sample. Different from a diffraction experiment, the scattered neutrons beam intensity were recorded as a function of their energy and momentum

[5]Dimensional Extreme Magnetic Neutron Diffractometer, https://neutrons.ornl.gov/hb3a/publications

change $I(\Delta\vec{q}, \Delta E)$. Figure 2.9 shows a photo of the neutron spectrometer HYSPEC[6] at ORNL and its simplified conceptual schematic. Pulses of neutron beams with initial energy and momentum $(E_i, \vec{q}_i)$ are sent through the beam guide to shine on the sample. The scattered beam first passes through a grid of radial collimators, such that the direction of its momentum is known $\frac{\vec{q}_f}{|\vec{q}_f|}$. When neutrons are recorded by the detector, its energy (E_f) and momentum's magnitude $(|\vec{q}_f|)$ are recorded and calculated. Combining these data, we can construct an intensity map as a function of energy and momentum transfer $I(E_f - E_i, \vec{q}_f - \vec{q}_i)$.

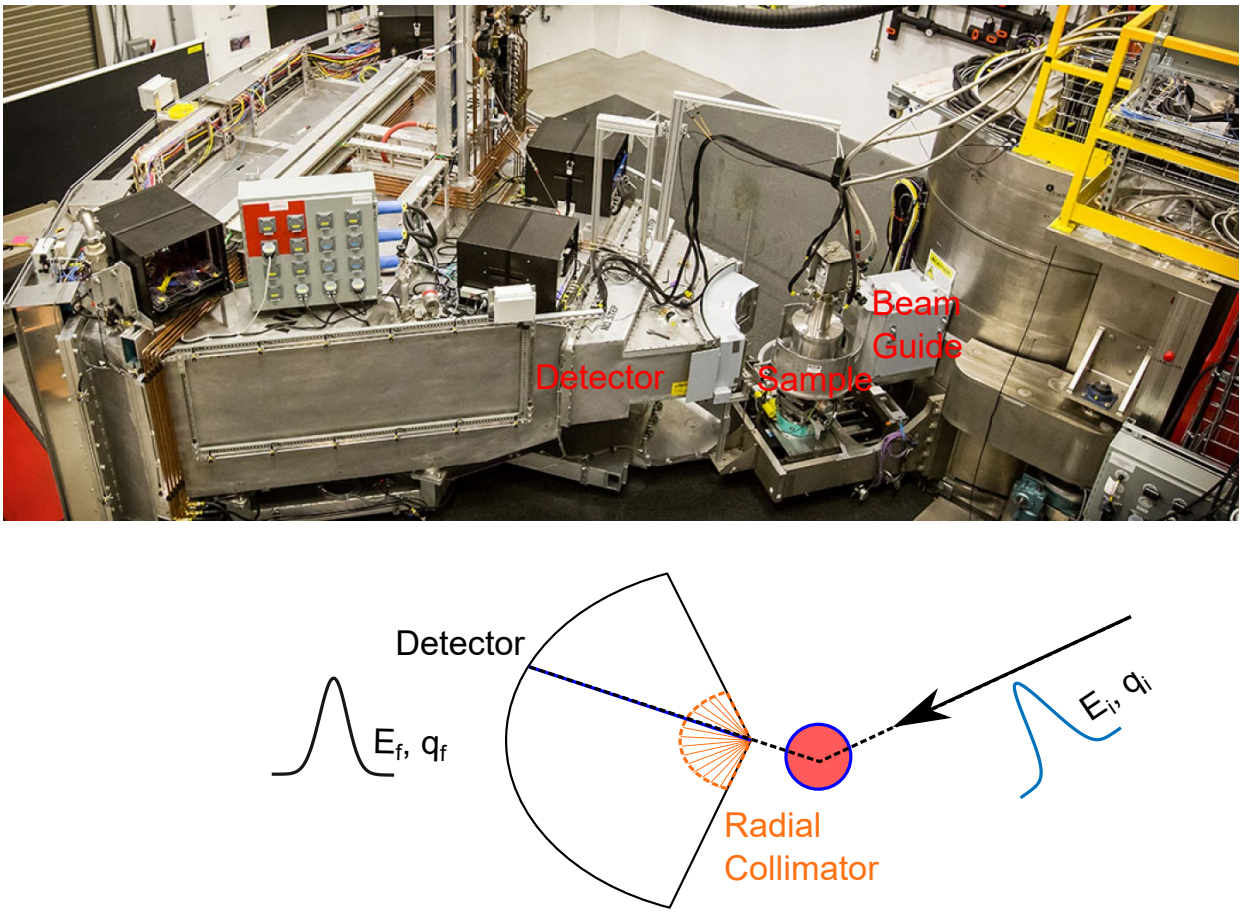

Figure 2.9: A photo and a simplified conceptual view of the Hybrid Spectrometer at oak ridge national laboratory.

[6]Hybrid Spectrometer, https://neutrons.ornl.gov/hyspec

Chapter 3

Anomalous thermal Hall effect of VI3

3.1 Introduction

The concept of non-trivial band topology originated from, but was not limited to, the pioneering studies on electron systems. The concept has been generalized to photon, phonon and magnon systems. One of the earliest experimental work on topological magnon was the observation of thermal Hall effect (κ_{xy}) in $Lu_2V_2O_7$ [25]. Although not stated explicitly, the theoretical calculations of this paper attributed the observed κ_{xy} to the Berry curvature of magnon bands. There have been rising interests in topological magnons due to its potential in offering dissipation-free spin transport channels [26].

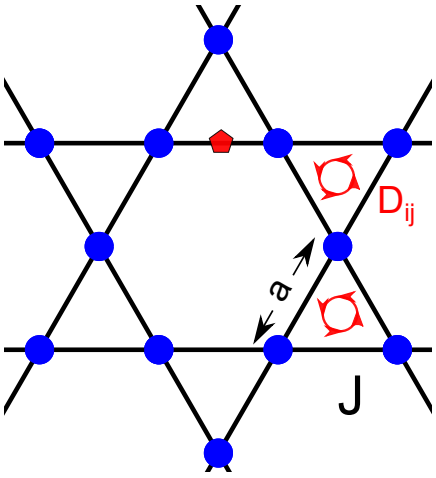

Figure 3.1: A kagome lattice with Heisenberg (J) and Dzyaloshinskii-Moriya (DM) interactions.

We discuss the theoretical backgrounds of a Chern type topological magnon 'insulator'[1] by examining a ferromagnet with Kagome lattice. A kagome lattice is shown in Figure 3.1, it is a 1/6 depleted triangular lattice. Each atom has four nearest neighbors. The center at each nearest neighbor bond (red pentagon) is not a center of inversion for the kagome lattice. This allows for a nearest neighbor Dzyaloshinskii-Moriya (DM) interaction in the kagome lattice. The DM interaction is an anti-symmetric exchange interaction, in that it involves the cross product of two neighbor spins, which is described as $\vec{D}_{ij} \cdot (\vec{S}_i \times \vec{S}_j)$.[2]

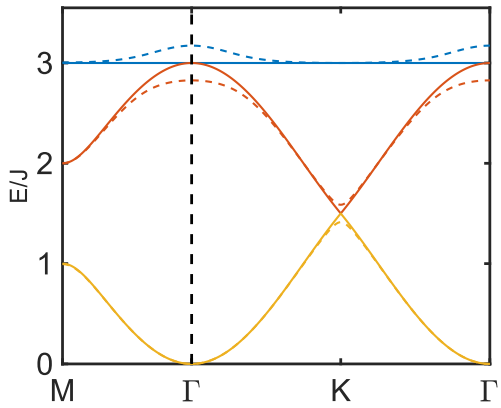

Figure 3.2: Magnon band structure for a kagome ferromagnet.

In the Haldane model we discussed in section 1.2.2, the second-neighbor imaginary hopping was an artificial construct, which may or may not be realized in a physical system. Here, the DM interaction is a physical realization of this imaginary hopping term.[3] For ferromagnetic kagome lattice with nearest neighbor Heisenberg interaction, the magnon dispersion along $M - \Gamma - K - \Gamma$ is shown in Figure 3.2. Without the DM interaction (solid lines), the magnon band feature a flat top band (blue) and a Dirac-like band touching at K. By adding in a finite DM interaction at $\vec{D} = (0, 0, 0.1J)$, all three bands become gapped.

[1] Magnon population follows the Bose-Einstein statistics, there is no well-defined metallic/insulator phases.

[2] As appose to Heisenberg/Ising type, which involves $-J\ \vec{S}_i \cdot \vec{S}_j$

[3] The DM interaction is represented by a pseudovector, the exact form of which needs to be determined by analyzing the space group symmetry of a material.

The corresponding Berry curvature, Chern number and the magnon edge states has been reported in [27]. Experimentally, the topological magnon bands of this model is proposed to be realized in a metal-organic material Cu(1,3-benzenedicarboxylate) [28, 29]. There are many theoretical models for topological magnon bands, and more experimental evidence are emerging. One of these theoretical models involves a magnetic honeycomb lattice with second-nearest neighbor DM interactions. The two-dimensional van der Waals magnets in transition-metal chalcogenides [30] often hosts a honeycomb lattice.

The intensity of currently available neutron beams is insufficient for the direct observation of magnon edge states. The thermal Hall effect was proposed to be one of the indirect way for observing the magnon edge states. These magnon edge states can act as heat carriers for anomalous transverse thermal transports. We aim to study the anomalous thermal Hall effect in VI_3 and understand its potential connection to topological magnons.

This section is adapted from [6]. Chunqiang Xu synthesized the material. Chunqiang Xu and Milos Sretenovic and I perfromed the experiments and analyzed the data. Caitlin Carnahan and Nishchay Suri performed the theoretical calculations with help from Di Xiao. Xianglin Ke and I wrote the manuscript with input/comments from all authors. Xianglin Ke supervised the project.

3.2 Results

Crystal structure - VI_3 crystallize in the space group R-3 (No. 148) at room temperature. Its crystal constants and crystal angles are $a = b = 6.8325$ Å, $c = 19.6776$ Å and $\alpha = \beta = 90°$, $\gamma = 120°$. The crystal structure can be visualized in Figure 3.3. Recent experiment has revealed a further lowering of crystal symmetry at lower temperatures [31, 32].

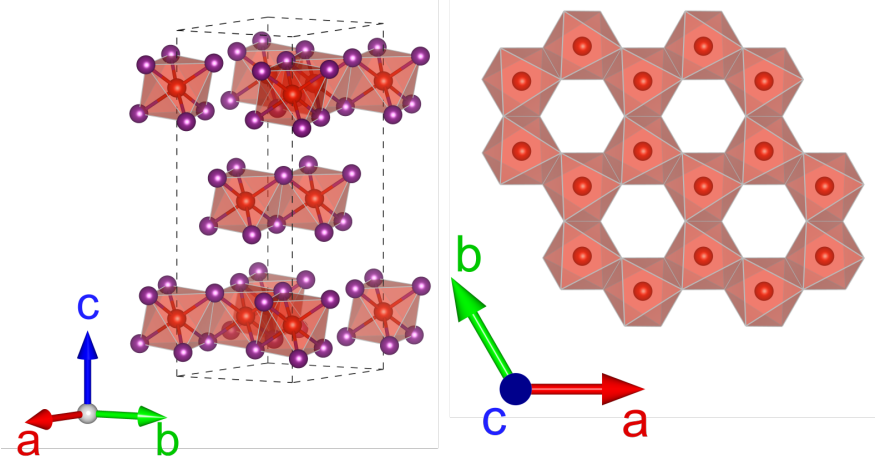

Figure 3.3: (left) Crystal structure of VI_3 at room temperature. Vanadium atoms are shown in red and Iodine atoms are shown in purple. (Right) View in the crystal ab-plane showing the Vanadium atoms assembled on a honeycomb lattice. Both figures are generated by VESTA [5].

Basic physical properties - VI_3 is a ferromagnetic insulator. Field cooled magnetic susceptibility (χ_c) data on a bulk sample is shown in the left panel of Figure 3.4. The Curie temperature determined by a peak in $|\frac{d\chi}{dT}|$ is $T_c = 50$ K. We have also measured the thermal conductivity (κ_{xx}) of VI_3 as shown in the right panel of Figure 3.4. The sudden increase of κ_{xx} around 77 K is due to the structural transition at this temperature [31, 32]. For 0T applied field, there is small anomaly in κ_{xx} near the Curie temperature. The thermal conductivity of VI_3 is strongly influenced by the applied field.[4]

For the magnetization data shown in the left panel of Figure 3.5, we see that VI_3 has Ising-type magnetic anisotropy, with an easy axis along the crystalline c-axis direction. The magnetic moment from our measurement is about 1.5 μ_B/V^{3+} below the Curie temperature. In the upper panel of Figure 3.5, we show both κ_{xx} and M measured at T = 20 K. At high fields, κ_{xx} increases monotonically. The increase of κ_{xx} at high fields (also shown by the data in Figure 3.4) indicates strong inelastic magnon-phonon scattering process. At low

[4]In this chapter, unless stated otherwise, the magnetic field will be applied along the crystalline c-axis.

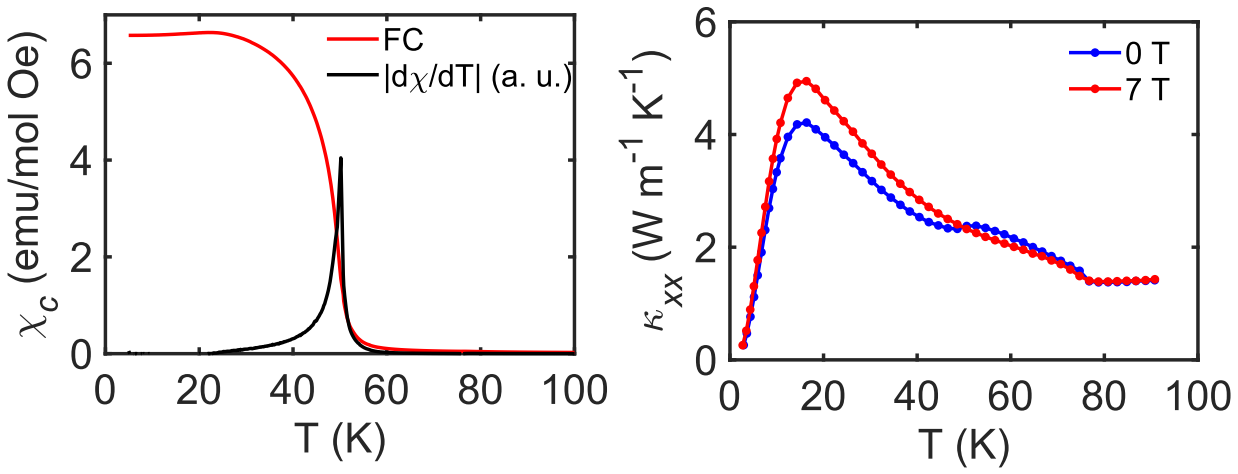

Figure 3.4: (Upper) The field-cooled magnetic (0.1 T) susceptibility and the absolute value of its temperature derivative of a VI_3 sample. (Right) The thermal conductivity of a VI_3 sample measured under 0 T and 7 T applied filed. The magnetic field is applied along the crystalline c-axis for both figures.

fields, there are two small dips in κ_{xx} coinciding with magnetization switching. A more detail profile of the low field behavior of κ_{xx} is shown in the right panel of Figure 3.5. The κ_{xx} clearly shows hysteresis behavior due to the switching of magnetic domains.

To summarize, VI_3 is a ferromagnetic insulator with Ising-type magnetic anisotropy, whose thermal conductivity is strongly influenced by the its internal magnetization.

3.3 The anomalous thermal Hall effect

The first curve - We aimed to investigate the potential magnon edge states in VI_3 using thermal Hall effect (THE) measurements. At the time, this was easier said than done. First, we had no experience in measuring THE of an insulating compound. There are many details which we need to learn through experimenting. Secondly, surveying through existing experimental data[5], we expect the thermal Hall signal κ_{yx} to be very weak and hard to detect. Thirdly, there have only been a handful of insulating materials with reported thermal Hall

[5]Please see Figure 4 in [33] for a summary of thermal Hall effects in insulators.

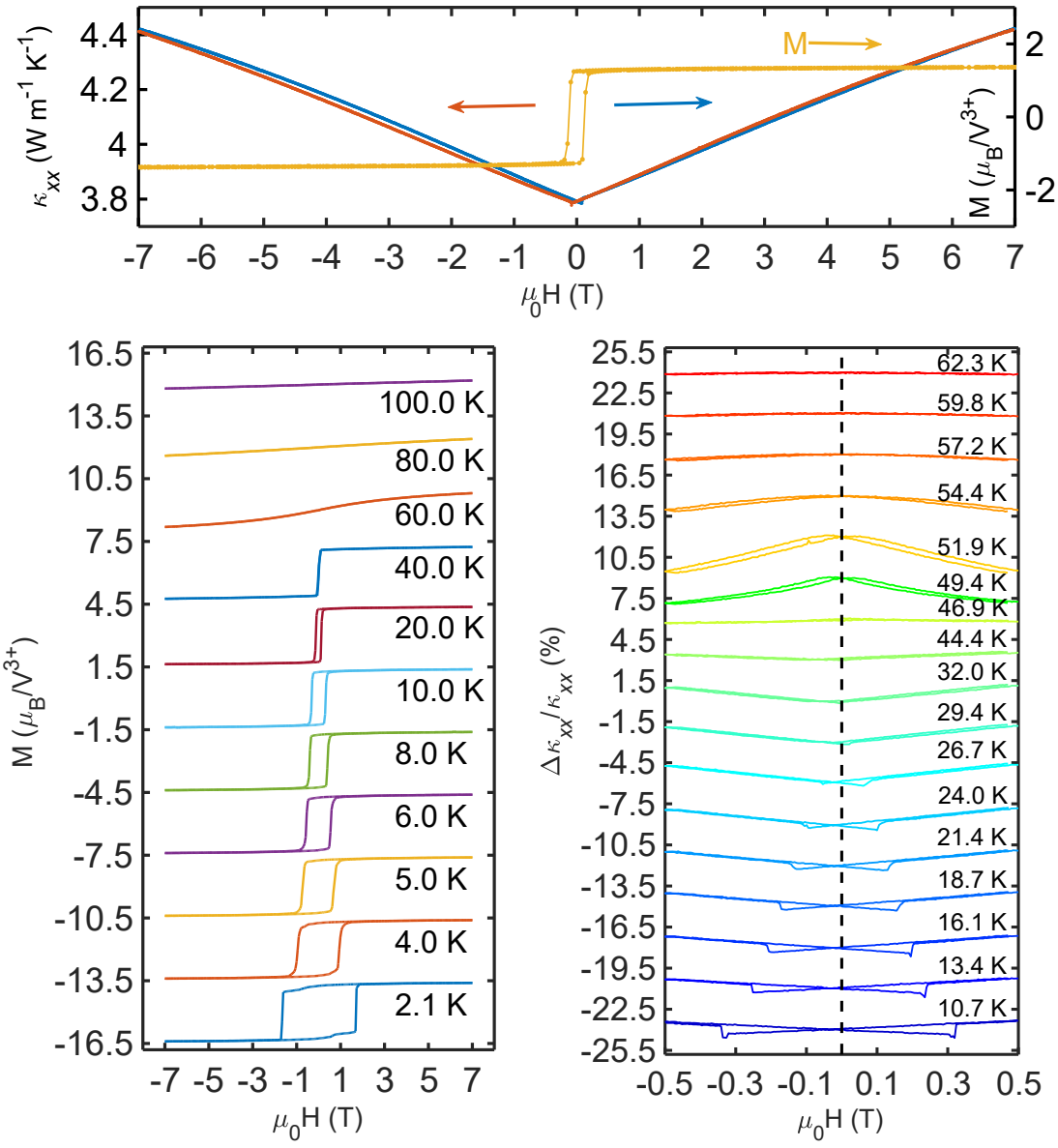

Figure 3.5: (Upper) Magnetization and thermal conductivity data measured at 20 K. For the thermal conductivity measurement, the sample is at 21.6 K due to heating. The orange/blue arrow indicates the field sweep direction. (Left) Magnetization data of VI_3 at selected temperatures from 2 K to 100 K. Each curve has been moved vertically by 3 μ_B/V^{3+} for clarity. (Right) Change of thermal conductivity in percentage as a function of magnetic field at different temperatures. Each curve has been moved vertically by 3 % for clarity.

effect. To actually observe THE in a material may requires an extensive search through many candidates.

Allow me to introduce the *first curve*, measured on a piece of VI_3 sample, whose sample

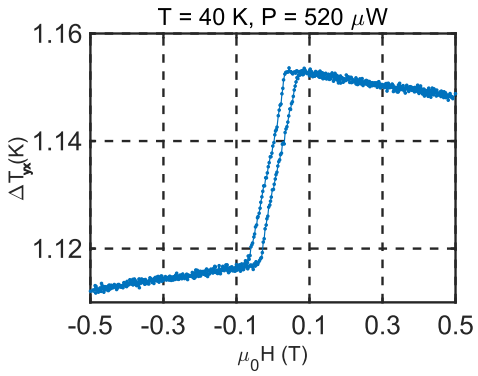

Figure 3.6: The *first curve*.

dimensions we forgot to measure, and no photo was taken before it was removed from the chamber. The experiment began at 2:48 p.m., January 29^{th}, 2021. During the cooling process, one of the temperature contact leads had fallen off. Luckily, it was the temperature lead at T_2, so we could process to measure thermal Hall effect. Prior to measuring VI_3, we have gone through only two materials: a vanadium oxide compound and $MnPSe_3$. We have learned two things from this experiment: first, the sample is hygroscopic. Second, there is a very strong[6] thermal Hall signal in VI_3.

Anomalous thermal Hall effect - We proceed to synthesize new batches of VI_3 single crystals and repeat the thermal Hall experiment on three samples. The data presented in Figure 3.7 was obtained on sample #2, with dimensional parameters at l = 1.19 mm, w = 1.33 mm and t = 0.084 mm. The anomalous nature of the observed signal is worth point out. The 'anomalous' here refers to the thermal Hall conductivity (κ_{xy}) being scaled with magnetization (M), rather than the applied magnetic field (μ_0H). Such behavior is critical for technological applications and has rarely been reported.

Below 10 K - Below 10 K, the effect of temperature contact mis-alignment (Section 2.1.5) becomes more apparent. In the left panel of Figure 3.8, we see clear hysteresis behavior in

[6]Easily measurable even by beginners.

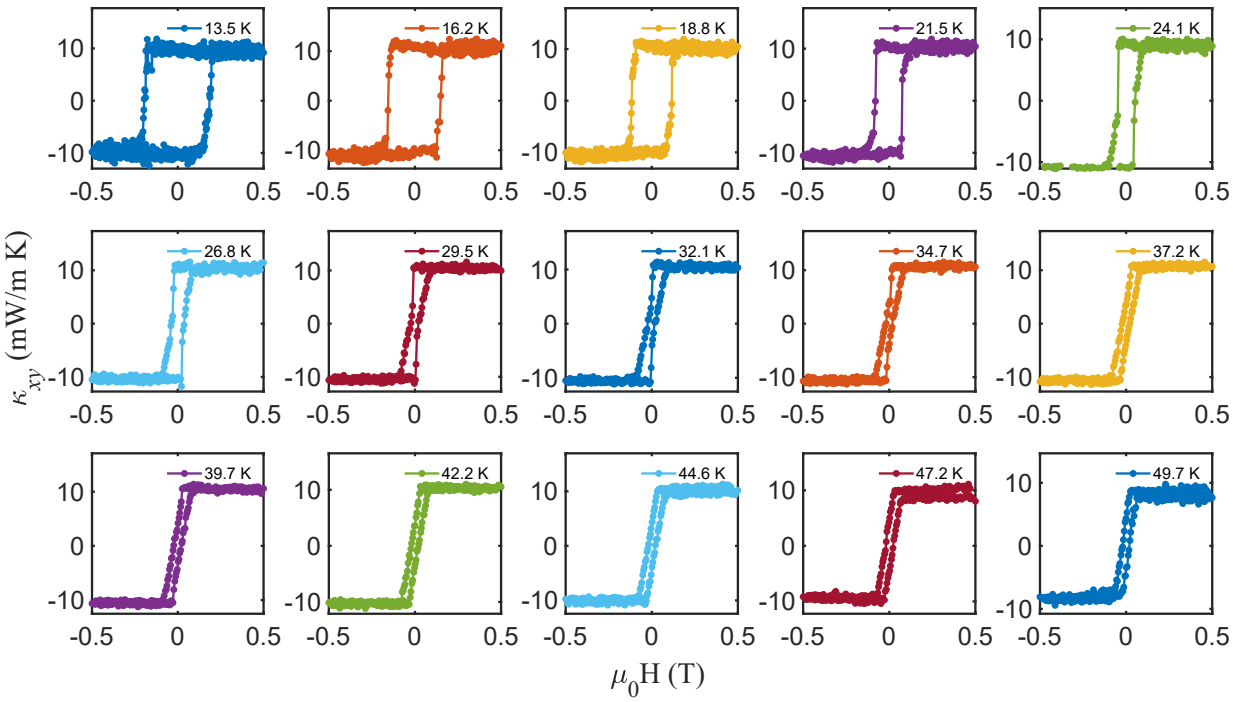

Figure 3.7: The anomalous thermal Hall effect measurement data at various temperatures between 10 K to 50 K.

Δw_{xx}. The signal in Δw_{xx} is inevitably also detected by the w_{yx} channel due to small mis-alignment of temperature leads (Middle panel, Figure 3.8). As a result, the w_{yx} curves show unwanted additional signals as temperature decreases. We adopted two methods to obtain the intrinsic value from the raw measurement data. The first way was described in Section 2.1.5. We applied this method to both w_{yx} and M, the data is shown in the upper right panel of Figure 3.8. This method will get rid of any hysteresis behavior and allow us to get the amplitude of the anomalous thermal Hall resistivity. The second method is described in [6], the data is shown in the lower right panel of Figure 3.8. Both methods yield identical results.

High field data - The thermal Hall conductivity (κ_{xy}) has also been measured up to 7 T. The orange and blue curve in Figure 3.9 shows κ_{xy} data measured for a typical hysteresis loop and up to 7 T at 21.5 K. The decrease of κ_{xy} at high fields can be fitted by a parabolic

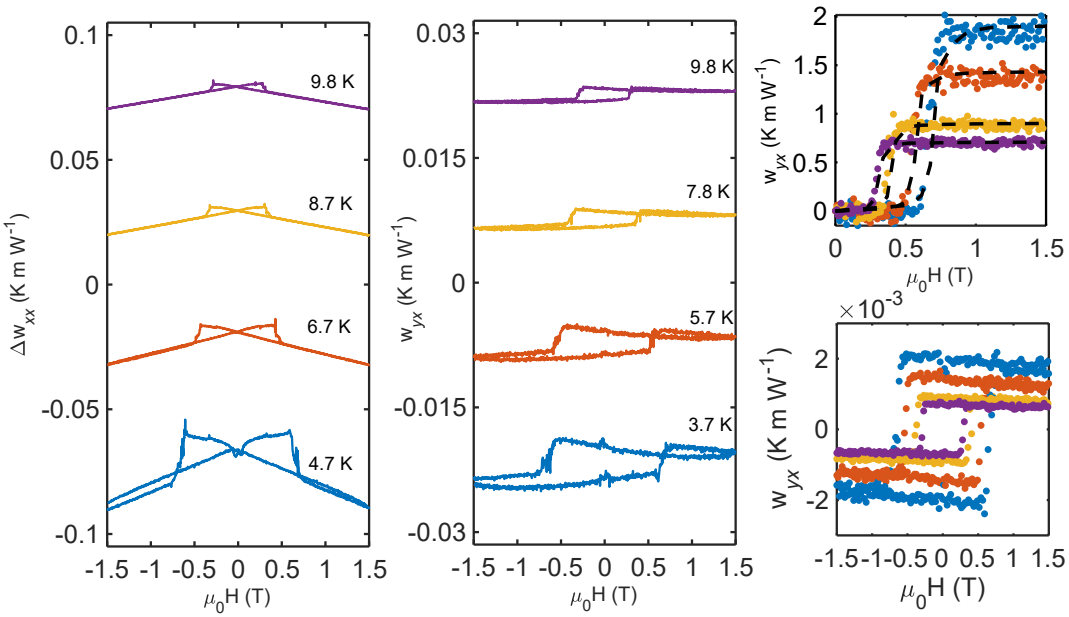

Figure 3.8: Thermal measurement data of sample #2 below 10 K. (Left) Change of thermal resistivity. Each curve is shifted vertically by 0.05 K m W^{-1} for clarity. (Middle) Thermal Hall resistivity. Each curve is shifted vertically by 0.015 K m W^{-1} for clarity. (Right, upper) Thermal Hall resistivity obtained by methods described in Section 2.1.5 The black dash lines are scaled magnetization data at each temperature. (Right, lower) Thermal Hall resistivity obtained by methods described in [6].

function $\kappa_{xy} = \kappa^o_{xy} + C(\mu_0 H)^2$, where was found to be C = -5.546*10^{-5} $Wm^{-1}K^{-1}T^{-2}$. On the other hand, κ_{xx} continue to increase with the applied field. These data suggests that the magnons in VI_3 is responsible for the observed thermal Hall effect.

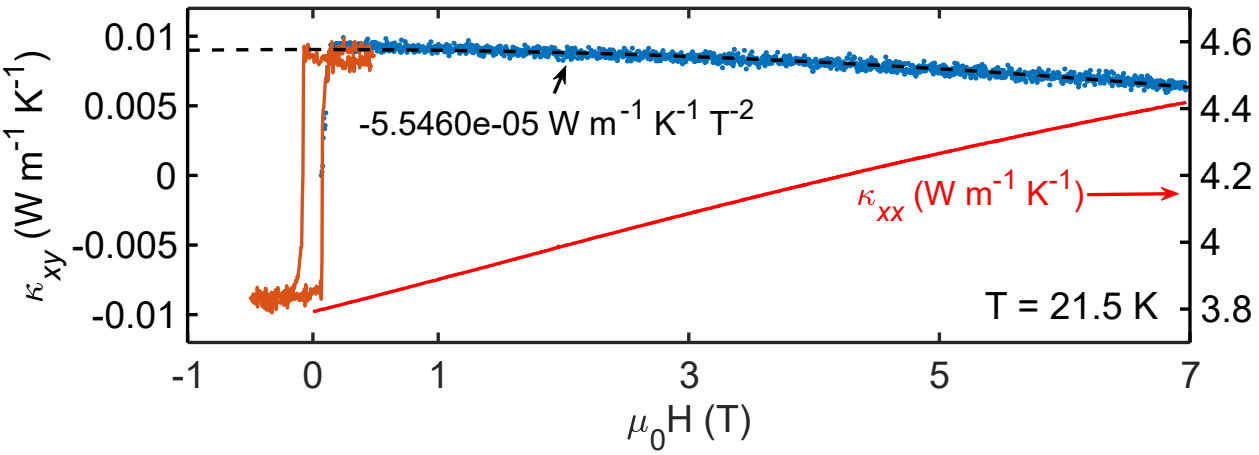

Figure 3.9: Thermal Hall conductivity (κ_{xy}, orange/blue) and thermal conductivity (κ_{xx}, red) measured up to 7 T.

Sample dependence - We have measured the thermal Hall effect on three pieces of VI_3 samples. We have observed experimental results with the same behavior, but different magnitude. The thermal conductivity of three samples are shown on the left panel of Figure 3.10. κ_{xx} display similar anomalies at the structural (78 K) and magnetic (50 K) transitions. The thermal Hall conductivity plateaus in a wide temperature range (middle, Figure 3.10) and has the hysteresis loop (right, Figure 3.10) for all three samples .

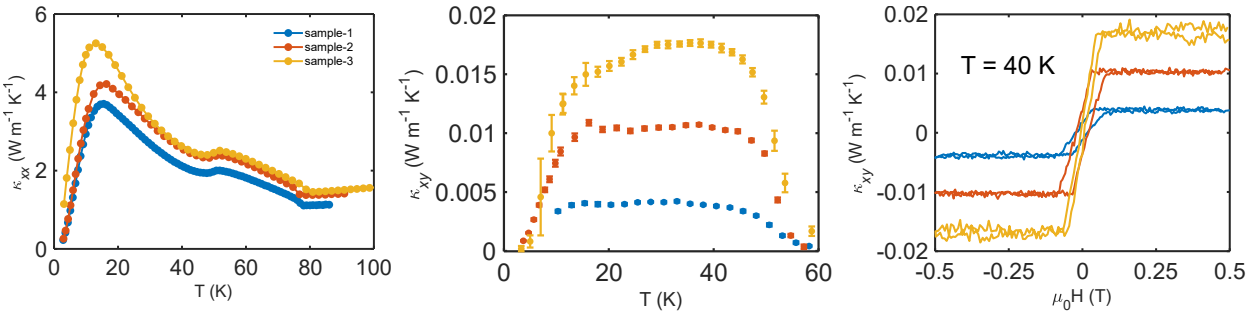

Figure 3.10: Temperature dependence of thermal conductivity (Left) and thermal Hall conductivity (Middle) for different samples. (Right) Magnetic field dependence of thermal Hall conductivity for different samples.

3.4 Theoretical interpretations

Magnon band structure and Berry curvature - We begin with a theoretical investigation of the band structure and potential Berry curvature of the magnons in VI_3. The system's Hamiltonian writes,

$$H = \sum_{\gamma=1,2,3} J_\gamma \sum_{i,j} \vec{S}_i \cdot \vec{S}_j + \sum_{\langle\langle i,j \rangle\rangle} \vec{D}_{ij} \cdot (\vec{S}_i \times \vec{S}_j) - K \sum_i S_{i,z}^2 - B \sum_i S_i^z \qquad (3.1)$$

We have included up to third neighbor Heisenberg interactions (J_γ), second neighbor Dzyaloshinskii Moriya interaction (DMI, $\vec{D}_{ij}$), easy axis single ion anisotropy (K) and an

external magnetic field (B). The exchange parameters used in our calculations are adapted from [34] tabulated in Table 3.1.

J_1	J_2	J_3	D	K
-2.746 meV	-0.169 meV	-0.210 meV	[-0.05, 0.95] meV	1.12 meV

Table 3.1: The set of exchange parameters used for magnon band calculations, including the Heisenberg interactions, Dzyaloshinskii Moriya interactions and single ion anisotropy.

The magnon band dispersion and the corresponding Berry curvature (Ω^z) are shown in Figure 3.11. Without DMI [$\vec{D}_{i,j} = (0, 0, 0)$ meV], the two magnon bands have a linear touching point at K, as shown by the blue and red lines. With finite DMI [$\vec{D}_{i,j} = (0, 0, 0.2)$ meV], the magnon bands become fully gapped. The corresponding Berry curvature (Ω_z) are shown on the right panel, where the upper half represents Ω^z for the upper band and lower half represents that of the lower band. The Chern number for these two bands are found to be +1 and -1, respectively.

Thermal Hall conductivity - More importantly, we aim to calculate the thermal Hall conductivity (κ_{xy}) due to the topological magnons. We adopt the method described in [35]:

$$\kappa_{xy} = -\frac{k_B^2 T}{\hbar A} \sum_n \int_{\vec{k}} c_2(\rho_n)\ \Omega_{n,z}(\vec{k}) \tag{3.2}$$

$$c_2(\rho_n) = (1+\rho_n)\left(log\frac{1+\rho_n}{\rho_n}\right)^2 - (log\rho_n)^2 - 2Li_2(-\rho_n) \tag{3.3}$$

Wherein ρ_n is Bose-Einstein distribution function for the n-th band, and Li_2 is the polylogarithm function of order two. The temperature dependence of κ_{xy} was taken into account by a mean-field method described in [36, 6]. In the upper panel of Figure 3.12, we

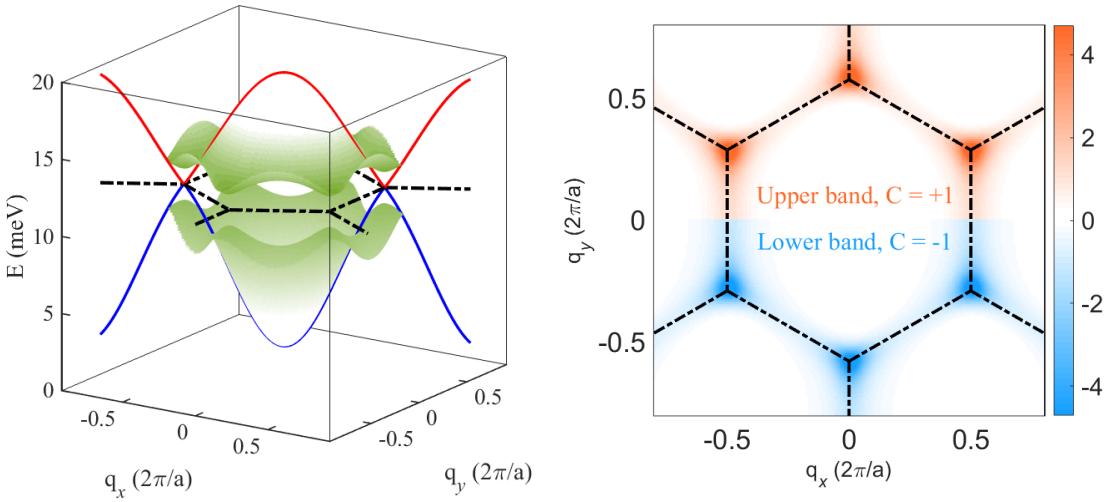

Figure 3.11: (Left) Magnon bands dispersion for $D_z = 0$ meV (red/blue curve) and $D_z = 0.2$ meV (green-white surface). The black dashline represents boundary of Brillouin zone. (Right) Z-component of the Berry curvature (Ω^z) for the upper and lower magnon band.

show the calculated results of κ_{xy} for various DMI strength. The calculated results show that κ_{xy} has a broad peak behavior as a function of temperature, and its magnitude should be on the order of 10^{-2} W m^{-1} K^{-1}. When compared with the experimental, we found that although the calculated data (with D = 0.2 meV) follows the same trend as the experimental data, there are two main discrepancies: one near the Curie temperature and another at the low temperatures region (lower panel, Figure 3.12). The difference of between experimental (blue) and theoretical (orange) values are shown as yellow markers. Near the magnetic phase transition, our mean-field approach is no longer valid. The magnetic short-range correlations may be responsible for the difference peaking at $T_c = 50$ K. In the lower temperature region, we found that κ_{xy}^{exp} rises much faster than κ_{xy}^{the}. The slow increase of κ_{xy}^{the} below 10 K was because non-zero Ω^z are mainly located at K-points and along K-M-K lines in the reciprocal space (Right panel, Figure 3.12). Magnons have relatively high energy and low population density ρ_n at these locations. Referring back to Equation 3.2, we see that some 'activation'

temperature is necessary for Berry curvature to take effect in the magnon system. With this observation, we investigate a potential mechanism which could give rise to non-zero Ω^z located at lower energy positions.

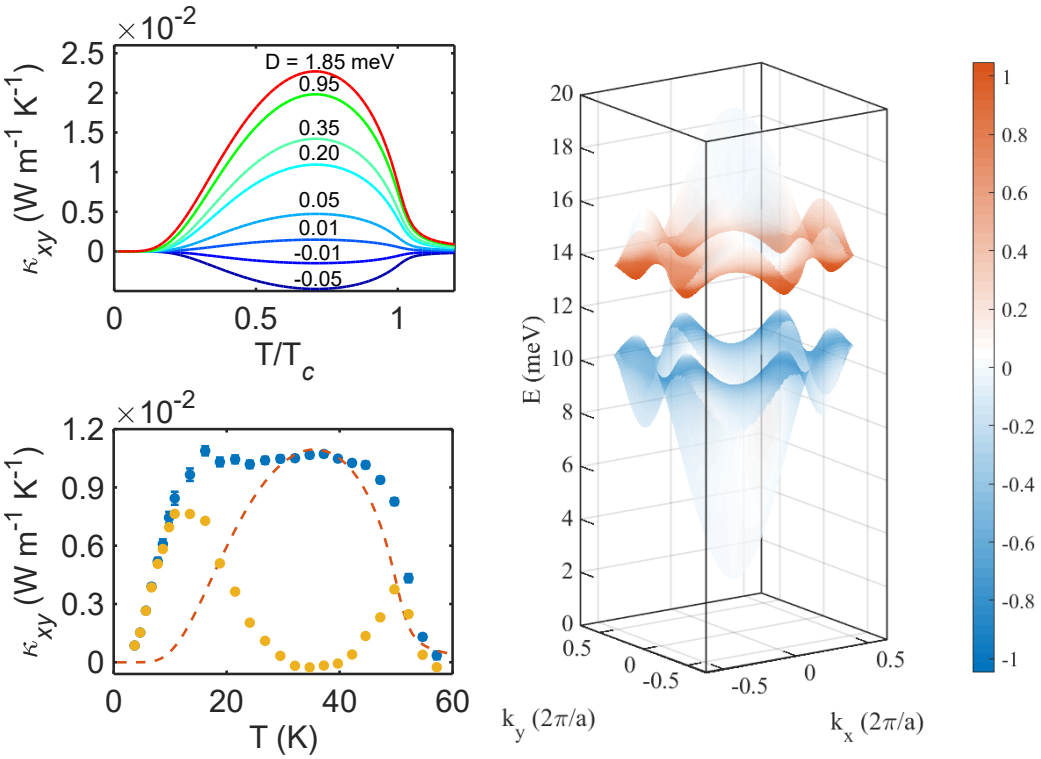

Figure 3.12: (Upper) Calculated thermal Hall conductivity due to topological magnon with various DMI strength. (Lower) Comparison between experimental data (blue) and theoretical predictions (orange) of thermal Hall conductivity. The difference between experimental and theoretical values are shown as yellow markers. (Right) Berry curvature distribution in the reciprocal space.

Magnon-phonon coupling - We consider the coupling between an out-of-plane phonon and in-plane magnon as described in [6], where g controls the coupling strength. The dispersion of the hybrid magnon-phonon band is shown in the left panel of Figure 3.13. There are anti-crossing regions near Γ-point and K-point due to magnon-phonon coupling. Furthermore, we have found that substantial Berry curvature emerging at the anti-crossing regions near Γ. The ring-shape region of Berry curvature near Γ is located at much lower energy and may be responsible for the observed κ_{xy} at low temperatures. In the right panel of Figure 3.13, we

show the comparison between experiment and theoretical values for various magnon-phonon coupling strength (g) [6]. We see that as the magnon-phonon coupling strength increases, the lower temperature region of κ_{xy}^{the} also increase, approaching the experimental values of κ_{xy}^{exp}. At present, we only considered an out-of-plane phonon mode, which couples to the in-plane magnons on a leading order. Future experiments to resolve the phonon spectrum may be an interesting study.

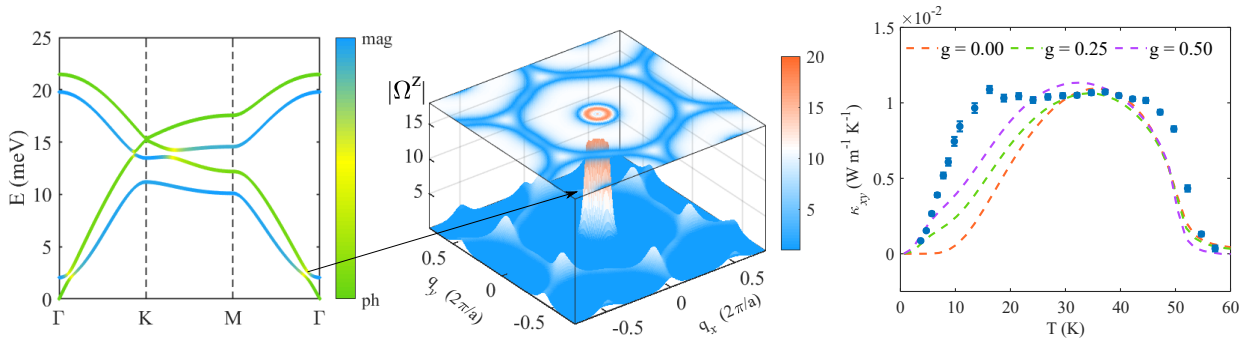

Figure 3.13: (Left) Total dispersion of the hybrid magnon-phonon band (g=0.5). (Middle) The absolute value of Berry curvature's ($|\Omega^z|$) distribution in the reciprocal space. The emergence of a ring-shaped region of Berry curvature is due to the magnon-phonon anti-crossing near Γ point. (Right) Comparison between experiment and theoretical values for various magnon-phonon coupling strength.

3.5 Summary and future perspectives

Summary - In conclusion, we report the observation of an anomalous thermal Hall effect (THE) with $\kappa_{xy} \approx 1 \times 10^{-2}\ WK^{-1}m^{-1}$ in an insulating van der Waals ferromagnet VI_3. The thermal Hall signal persists in the absence of an external magnetic field and flips sign upon the switching of the magnetization. By combining the theoretical calculations, we show that VI_3 exhibits a dual nature of the THE, i.e., dominated by topological magnons hosted by the ferromagnetic honeycomb lattice at higher temperatures and by phonons induced by the magnon-phonon coupling at lower temperatures. Our results not only position VI_3 as

the first ferromagnetic system to investigate both anomalous magnon and phonon THEs, but also render it as a potential platform for spintronics/magnonics applications.

Future perspectives - A potentially interesting topic for further investigation is to experimentally measure the spin currents in VI_3. The topological nature of the magnon bands can induce a transverse spin current. In our work, the evidence of this spin current is demonstrated through the thermal Hall effect (κ_{xy}) and the suppression of κ_{xy} at higher magnetic field. A direct measurement of the underlying spin currents is a more challenging, and rewarding approach for two main reasons. First, such measurement should, in principle, exclude all contributions from other factors (such as phonons). Therefore, one may obtain a direct comparison between the experimental data and theoretical predictions. This will serve as a one of the most convincing work in the study of topological magnons in general. Secondly, the direct observation of spin currents due to non-trivial magnon band topology in a van der Waals magnet has important implications to the field of magnonics. For example, proof-of-concept design of spin-wave diodes, spin-wave beam splitters, and spin-wave interferometers using topological magnons have been demonstrated by a recent theoretical study [37]. VI_3 provides a material platform for experimentally demonstrating such designs.

Inelastic neutron scattering experiment on VI_3 is another potential future directions. We have noticed a recent paper [38] on the effort, in which the authors investigated the spin dynamics of VI_3 using inelastic neutron scattering technique. However, better quality data is highly desired. This will require some more efforts from the material science community to achieve higher crystal quality as well as large crystal dimensions. High quality inelastic neutron scattering can provide insights on the magnon and phonon band structure of VI_3. These are crucial information for a deeper understanding for the anomalous thermal Hall effect in VI_3.

Chapter 4

Transport studies of magnetic topological metals

4.1 Introduction

Berry curvature and itinerant electrons - A charged particle experience a force $\vec{F} = q(\vec{E} + \vec{v} \times \vec{B})$ due to the presence of electromagnetic fields. From Maxwell's equations, we see that the magnetic B-field has zero divergence ($\nabla \cdot \vec{B} = 0$), meaning that there exists a magnetic vector potential ($\vec{A}$), such that $\vec{B} = \nabla \times \vec{A}$. Together with the electric potential ($\vec{E} = -\nabla\phi$), $(\phi, \vec{A})$ forms the electromagnetic potential. Although $(\phi, \vec{A})$ is a gauge field which cannot be measured directly, it has directly measurable effect on the phase of wave functions. This is known as the Aharonov-Bohm (AB) effect [39]. The AB-effect is a special application of the more general concept as Berry's phase [18]. In this sense, we can draw an analogy between magnetic fields and Berry curvature. The Berry potential is a gauge field representing the 'phase gradient' of a wave function in a parameter space, i.e., $\vec{A}(\vec{r}) = i \langle \phi(\vec{r}) | \nabla_{\vec{r}} | \phi(\vec{r}) \rangle$. As discussed in Section 1.2.2, the Berry curvature is the curl of Berry potential $\vec{\Omega}(\vec{r}) = \nabla_{\vec{r}} \times \vec{A}(\vec{r})$. Given the analogy, we can ask the following question: Does the Berry curvature exert a force on charged particles? And does it have a measurable physical effect?

To the first question, Berry curvature does not directly exert a force on a charged particle.

This is quite obvious since the gauge field (Berry connection, $\vec{A}$) does not directly couple to the charge. However, a more subtle point is that Berry curvature has a measurable physical effect for electrons in a crystalline lattice: the anomalous Hall effect (AHE) [40]. While $\vec{\Omega}$ does not couple to the charge directly, the Bloch electron group velocity acquires an 'anomalous' term ($q\vec{E} \times \vec{\Omega}$) due to the Berry curvature [40, 41, 42]. The 'anomalous' velocity give rise to an intrinsic contribution (σ^{int}) to the total anomalous Hall conductivity (σ_{xy}) and has been studied extensively.

This mechanism can also give rise to an anomalous thermoelectric conductivity (α_{xy}) [43]. The thermoelectric conductivity measures the anomalous current density driven by a temperature gradient ($\alpha_{xy} = j_x/\partial_y T$, $A\ m^{-1}K^{-1}$). The electric and thermoelectric conductivity tensor are correlated, as expressed in the Mott relation $\alpha_{xy}/T = \frac{\pi^2 k_b^2}{3e}\frac{d\sigma_{xy}}{dE}|_{\epsilon=\epsilon_f}$. For the study of topological metals, α_{xy} serves as a complementary tool to measure the Berry curvature distribution in the reciprocal space: α_{xy} is only sensitive to the Berry curvature in the vicinity of Fermi level. Experimentally, there have been rising interests in the anomalous Nernst effect (ANE) of magnetic topological metals. The Seebeck (S_{xx}) and Nernst (S_{xy}) coefficients have been defined in Section 2.1.1. We can write these coefficients in a compact form as a 2-rank tensor $\bar{S} = \begin{pmatrix} S_{xx} & S_{xy} \\ S_{yx} & S_{yy} \end{pmatrix}$, the formula $\bar{\alpha} = \bar{\sigma}\bar{S}$ relates the thermoelectric conductivity, conductivity and thermoelectric coefficients.

Anomalous Nernst effect based thermoelectric device - Another reason for the rising interests in ANE of magnetic topological metals is its potential applications in energy conversion device [44, 45]. There are two main merits of the ANE based device compared to its Seebeck based counterparts. First, the voltage gradient and temperature gradient are orthogonal to each other, allowing more freedom in device design. Secondly, given the same figure of merit

value (zT), Nernst effect based devices can achieve much higher energy conversion efficiency. First, the Nernst-based device output can be increased by increasing the thermoelectric module density [46]. This is in contrast to Seebeck-based device, whose output increases with the device's physical dimensions. Second, the Nernst-based device has a higher energy conversion efficiency than its Seebeck-based counterpart with the same thermoelectric figure of merit value (zT) [45]. For the development of ANE based devices, the greatest obstacle thus far is the extremely low zT value.[1]

4.2 Exchange-biased anomalous transport

Introduction - $TbMn_6Sn_6$ belongs to a family of the RMn_6Sn_6 (R = rare earth, Y, Sc, Lu) compounds. The manganese atoms in these compounds form a double-layer Kagome lattice structure. The unique Kagome lattice can give rise to flat bands and Dirac points in the band structure. The former provides an ideal platform for studying strongly correlated phenomena, while the latter is an interesting topological object by its own right. In particular, $TbMn_6Sn_6$ stands out as a ferrimagnet with out-of-plane magnetization where Tb moment aligns antiferromagnetically with Mn moment. As a result, the electronic band structure of $TbMn_6Sn_6$ exhibits spin polarized Dirac dispersion with a Chern gap. The massive Dirac bands near the Fermi energy can give rise to anomalous electric and heat transport phenomena.

This section is adapted from [20]. Chunqiang Xu synthesized the samples. Chunqiang Xu, Milos Sretenovic and I fabricated the devices and performed the measurements. I analyzed the data. Jahyun Koo performed theoretical calculations with support from Binghai Yan.

[1] It should be noted that the Nernst effect of Cd_3As_2 can reach zT = 0.7 at 350 K [47]. However, a sizable magnetic field (3 T) is required for obtaining such large zT value.

Xianglin Ke and I wrote the manuscript with inputs/comments from all authors. Xianglin Ke supervised the project.

Crystal and magnetic structure and basic physical properties of $TbMn_6Sn_6$ - $TbMn_6Sn_6$ (TMS) crystallize in space group P6/mmm (No. 191), with lattice constants a = b = 5.522 Å, c = 9.004 Å and crystal angles $\alpha = \beta = 90^\circ$, $\gamma = 120^\circ$. The terbium atoms are arranged in a triangular lattice, while the manganese atoms are arranged in a kagome lattice. The magnetic structure of TMS has been determined from a previous powder neutron diffraction experiment [48]. Both the terbium's and manganese's magnetic moments are ferromagnetic withing the ab-crystal plane. Along the crystalline c-axis, the terbium and manganese spins are anti-ferromagnetic to each other (left panel, Figure 4.1). TMS undergoes a spin-reorientation process near 310 K as shown by the inset in the right panel of Figure 4.1. The magnetic moments switch from an in-plane configuration at higher temperature to an out-of-plane one at lower temperature [48]. The bifurcation between field cooled and zero-field cooled susceptibility may be attributed to formation of anti-aligned ferrimagnetic domains [49]. The temperature dependence of some basic physical properties of TMS (lower panel, Figure 4.1) shows typical behavior for a magnetic metal.

Exchange-bias behavior of $TbMn_6Sn_6$ - Exchange-bias was first discovered by W. H. Meiklejohn and C. P. Bean [50], which was described as the following: '*The exchange anisotropy is a unidirectional anisotropy in that it produces one easy direction of magnetization.*' A typical magnetization curve of $TbMn_6Sn_6$ is shown in Figure 4.2 (field-cooled), demonstrating a clear exchange-bias (EB) behavior. The necessary ingredients for EB are: i) an uncompensated magnetic moment and ii) a mechanism for its pinning. This is typically realized by patterning thin layers of ferromagnetic/anti-ferromagnetic heterostructures. Exchange-Bias behavior has also been observed in single-phase, single-crystalline materials.

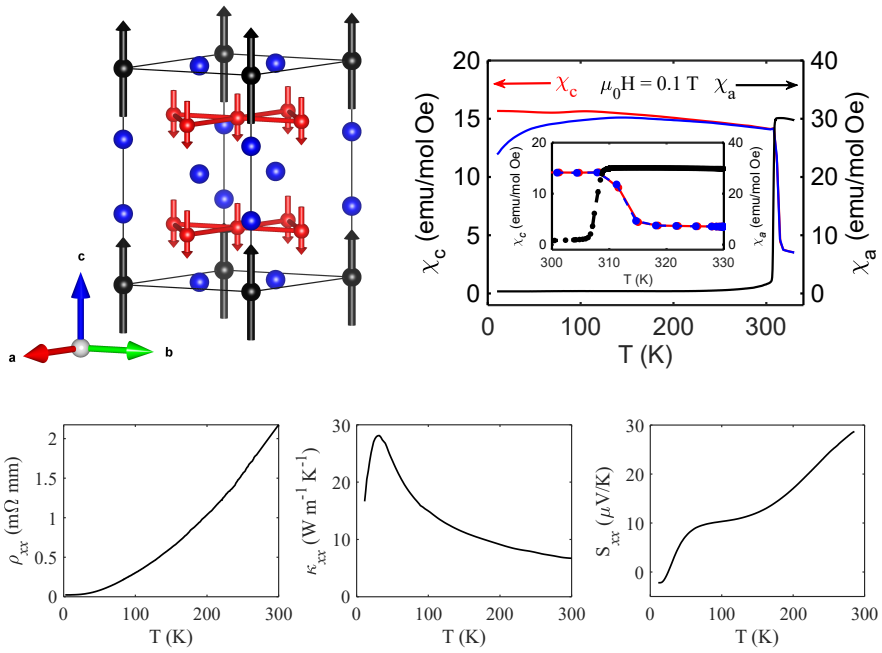

Figure 4.1: (Left) Crystal and magnetic structure of $TbMn_6Sn_6$. The terbium, manganese and tin atoms are represented by the black, red and blue spheres, respectively. The terbium and manganese's magnetic moments are represented by black and red arrows. (Right) Magnetic susceptibility data of $TbMn_6Sn_6$ measured along the crystalline c-axis (red, blue) and a-axis (black). (Lower) The temperature dependence of resistivity (ρ_{xx}), thermal conductivity (κ_{xx}) and Seebeck coefficient (S_{xx}) of $TbMn_6Sn_6$.

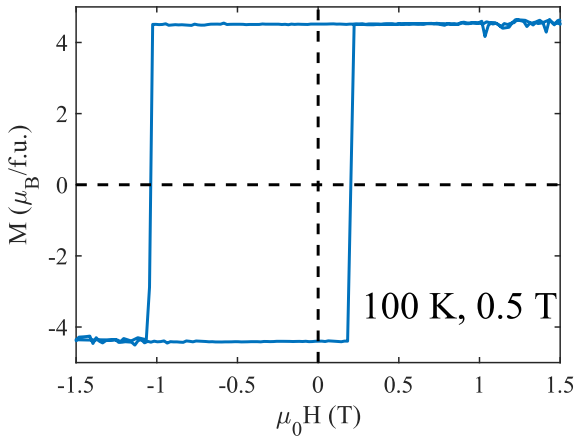

Figure 4.2: Exchange biased magnetization curve of $TbMn_6Sn_6$ at 100 K.

Exchange-bias behavior has rarely been observed in single-crystalline magnetic topological metals. In a ferromagnetic Weyl semimetal $Co_3Sn_2S_2$, exchange-bias behavior has been

observed and proposed to originate from the coexisting ferromagnet/spin glass orders. In $TbMn_6Sn_6$, a ferrimagnetic metal hosting a Chern gap, we have observed huge exchange-bias behavior. In the left panel of Figure 4.3, the magnetization of TMS after cooling to the respective temperatures with an applied field of 0.5 T were shown. The coercivity and exchange-bias field were found to increase in magnitude as temperature decreases. In the right panel of Figure 4.3, the magnetization of TMS after cooling to 100 K with the respective cooling fields were shown. The coercivity and exchange-bias field were found to increase with the cooling field. The coercive fields are signified by a switch in magnetization and the bias-field (H_{EB}) is defined as the average of the coercive fields ($H_{EB} = \frac{H_{c1}+H_{c2}}{2}$). The exchange-bias field of TMS has reached considerable magnitudes.

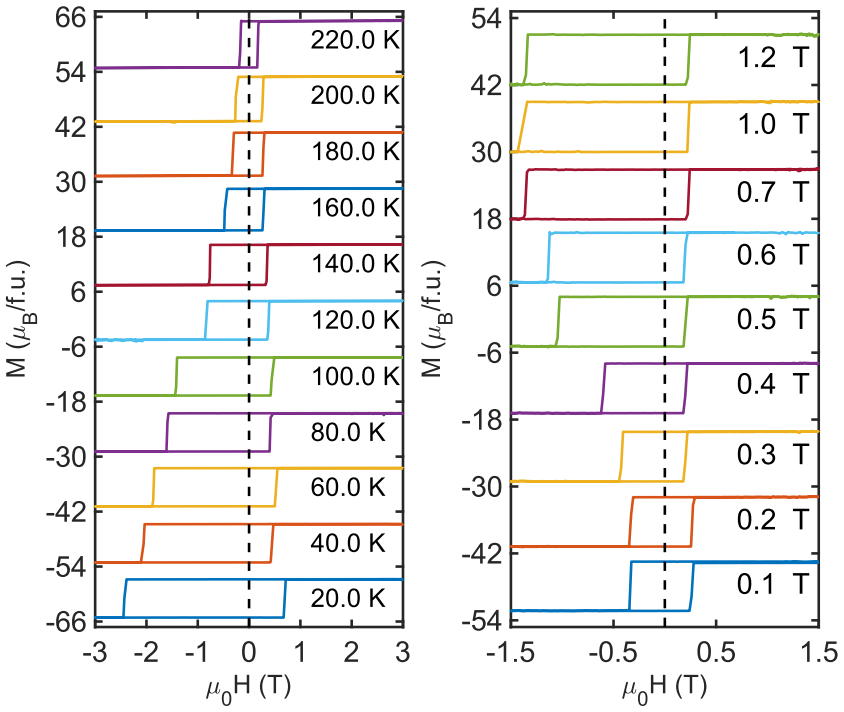

Figure 4.3: (Left) Magnetization data after cooling to the respective temperatures with an applied field of 0.5 T. (3 T → -3 T → 3 T) (Right) Magnetization data after cooling to 100 K with the respective applied fields. (1.5 T → -1.5 T → 1.5 T)

The exchange-bias field's temperature and field dependence have been summarized in

the left panel of Figure 4.4. One of the key challenges in ANE-based thermoelectric device design was the stray field problem during miniaturization. The stray field originating from neighboring magnetic thermoelectric material sets the upper limit for thermopile density. Exchange-bias can provide a solution to this issue if the exchange-bias field is strong enough. In Figure 4.4, we see that the exchange-bias field can exceed the magnetization below 120 K. In reality, it is only necessary for the exchange-bias field to be comparable to magnetization. We also see that the exchange-bias field increases with the cooling-field, saturating at $\mu_0 H_{FC} = 0.7$ T. This effect could be further increased by increasing the sweeping field range. In the right panel of Figure 4.4, we see the filed-reversal and training effect (hysteresis loop depends on the number of repeating measurements, [51]) of the exchange-bias behavior. The potential mechanism for the exchange-bias behavior may be a co-existing spin-glass phase in the system [20].

Anomalous transports - In Figure 4.5 we summarize the AHE effect[2] in $TbMn_6Sn_6$. In the left panel, the field dependence of σ_{xy} were shown. In the intermediate temperature range (e.g., T = 240 K), we observe the effect of magnetic metastable states as sudden jumps in σ_{xy}. The single-ion anisotropy of Tb/Mn and the inter-layer exchange interactions may be responsible for the complex energy landscapes and the metastable states. The ordinary contribution ($\sigma^o_{xy} \propto \mu_0 H$) to the total Hall conductivity (σ_{xy}) only become visible at much lower temperature (e.g., 100 K). The temperature dependence of the anomalous Hall conductivity ($\sigma^A_{xy} = \sigma_{xy} - \sigma^o_{xy}$) was shown in the upper right panel. The anomalous Hall conductivity decrease with temperature, indicating the there is a skew-scattering component ($\rho^{sk}_{yx} \propto \rho_{xx}$) in the total anomalous Hall signal. We extract the intrinsic AHE component

[2]All transport data shown from this point on have been trained by repeating field sweeping sequence three times.

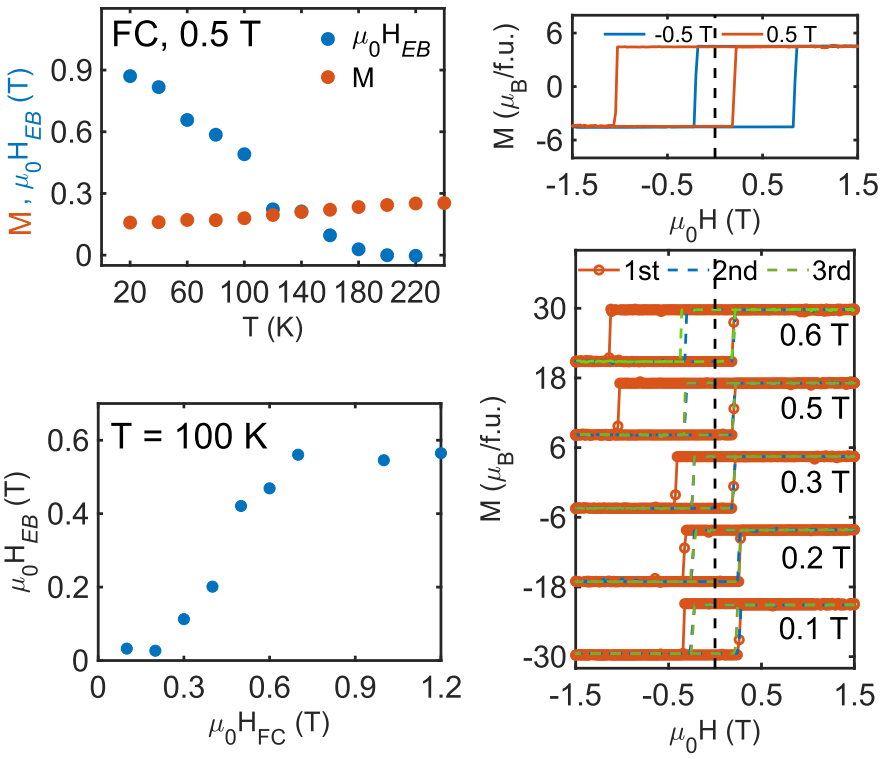

Figure 4.4: (Left) Temperature and field dependence of the bias-field and magnetization. (Right) Field-reversal and training effect of the exchange-bias behavior.

($\rho_{xy}^{int} \propto \rho_{xx}^2$) by fitting the total Hall resistivity as $\rho_{yx} = A\rho_{xx} + B\rho_{xx}^2$ as shown in the lower right panel. The red line is the fitting curve and the blue dash lines are the 95% confidence bound. The intrinsic component was found to be $131 \pm 20\ (\Omega\ cm)^{-1}$. This value is consistent with a previous report [52].

We have also measured the anomalous thermal Hall effect and anomalous Nernst effect of $TbMn_6Sn_6$ as shown in Figure 4.6. The field dependence of κ_{xy}^A and S_{xy}^A/T at a few selected temperatures were shown in the left and middle panels of Figure 4.6. Similar features were observed in these measurements. The temperature dependence of κ_{xy}^A is shown in the upper-right panel of Figure 4.6, which also decreases with temperature. We show the anomalous Lorentz number ($L^A = \frac{\kappa_{xy}^A}{\sigma_{xy}^A T}$) in units of the Lorentz number ($L_0 = 2.44 \times 10^{-8}\ V^2K^{-2}$) as the blue markers. L^A remains close to the Lorentz number in the measured temperature

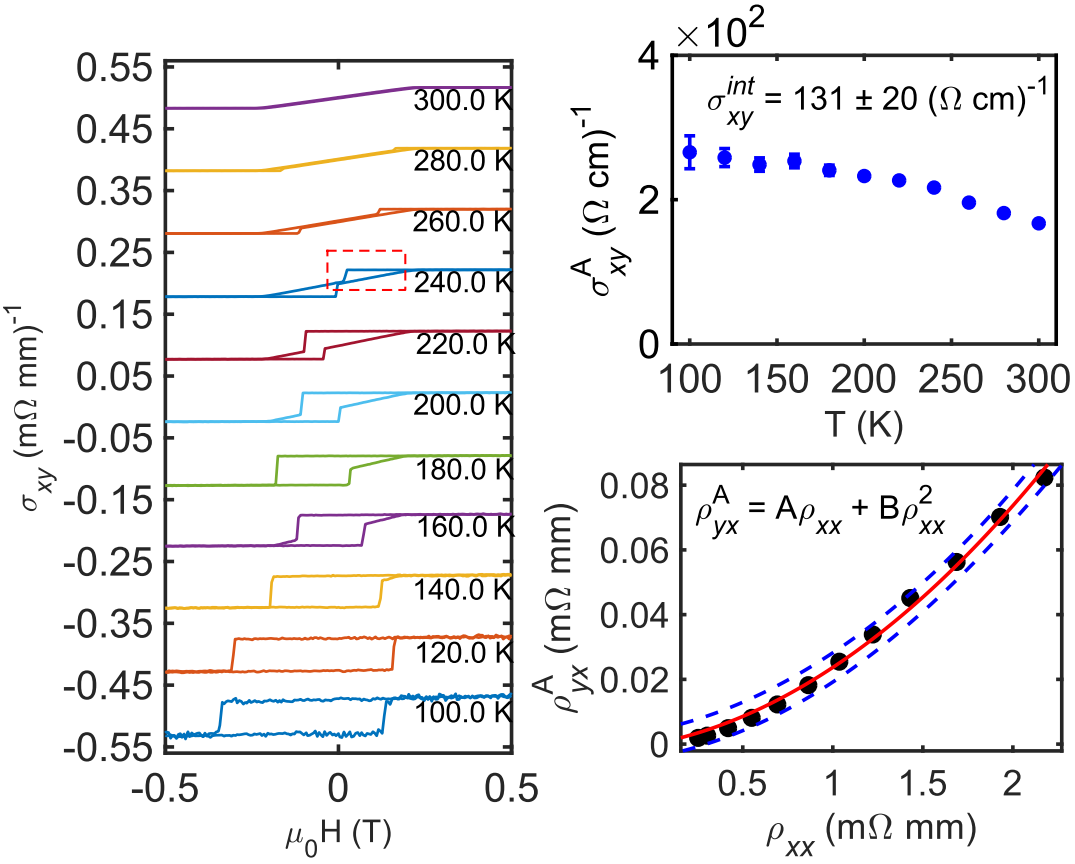

Figure 4.5: (Left) Magnetic field dependence of σ_{xy} measured at various temperatures. (Upper, right) Temperature dependence of σ^A_{xy}. (Lower, right) Fitting result of the anomalous Hall resistivity.

range. The anomalous Nernst coefficient monotonically increases with temperature.

Theoretical interpretations - We investigate the band structure and its Berry phase by carrying out density functional theory (DFT) calculations on $TbMn_6Sn_6$. The DFT calculations are done within the generalized gradient approximation (GGA) framework. The Berry phase were evaluated by an effective Hamiltonian, obtained through projecting the Bloch wave functions into Wannier functions. In the upper left panel of Figure 4.7, we show the band structure as well as its Berry phase ($-\Omega_{xy}$). With spin-orbit interactions (SOC) taken into account, there are multiple anti-crossing points with non-zero Berry phase near the Fermi level. We further calculate the anomalous Hall conductivity due to Berry phase

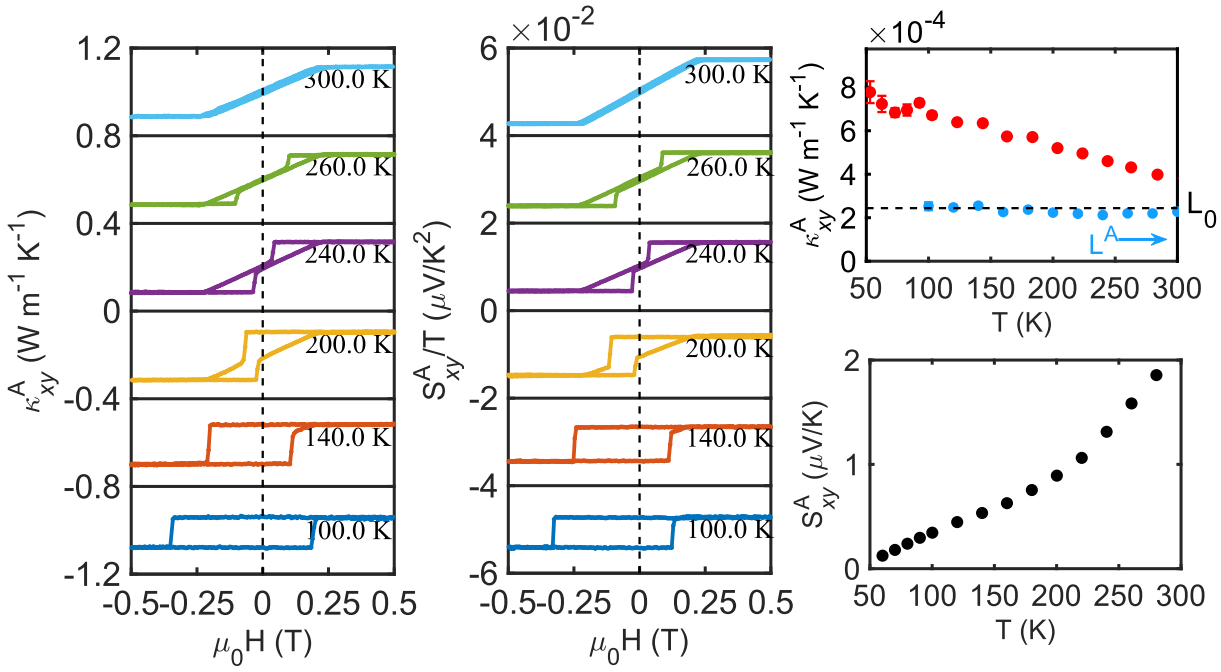

Figure 4.6: (Left) Field dependence of anomalous thermal Hall conductivity. (Middle) Field dependence of anomalous Nernst coefficient . (Upper, right) Temperature dependence of anomalous thermal Hall conductivity and anomalous Lorentz number. (Lower, right) Temperature dependence of anomalous Nernst coefficient.

using the Kubo formula, as shown in the upper right panel of Figure 4.7. The calculated result is $\sigma_{xy} = 120\ (\Omega\ cm)^{-1}$, close to the intrinsic value extracted from the experiment data at $\sigma_{xy}^{inc} = 131 \pm 20\ (\Omega\ cm)^{-1}$. A surface plot of Berry phase at the Fermi level with kz = 0 is shown in the lower left panel of Figure 4.7. The Berry phase at Fermi level was dominated by contributions from the anti-crossings at K-points, as suggested by a previous scanning tunneling microscopy (STM) study. However, we found $TbMn_6Sn_6$ to be a multi-band system beyond the simple kagome model base on our DFT results. In the lower right panel of Figure 4.7, a comparison between the experimental and theoretical thermoelectric linear response tensor is shown. Compared to the calculated results (blue line), the experiment data (blue markers) shows a much faster rise of α_{xy}^A/T as temperature decreases. It has been shown that skew-scattering may contributes significantly to the total α_{xy}^A for

magnetic topological metals. The orange curve shows the 'adjusted' theoretical results, by multiplying a temperature dependent variable $\beta = \sigma_{xy}^{A}/\sigma_{xy}^{inc}$ to the calculated results. The 'adjusting' factor β takes into account the effect of skew-scattering in a naive manner. At the lower temperature region, the effect of skew-scattering is more prominent as a result of the enhanced conductivity (σ_{xx}), and the experiment data approaches the adjusted theoretical predictions.

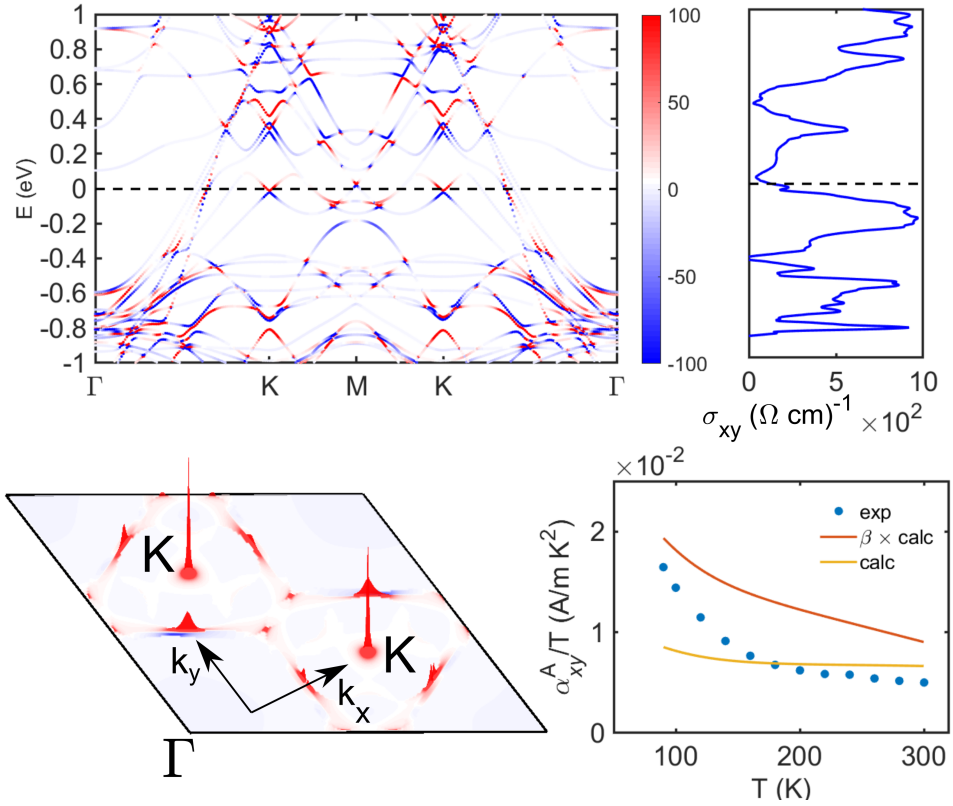

Figure 4.7: (Upper, left) Band structure and Berry phase ($-\Omega_{xy}$) of $TbMn_6Sn_6$. (Upper, right) Calculated anomalous Hall conductivity. (Lower, left) Berry phase at the Fermi level with kz = 0. (Lower, right) Experimental and theoretical thermoelectric linear response tensor.

The stray field problem - Previous discussions on the *The stray field problem* has remained qualitative. Numerical evaluation of the stray field (demagnetization field) produced by the candidate magnetic topological metals will provide crucial insight for application purposes.

For an anomalous Nernst effect based thermoelectric device, a typical thermopile consists of neighboring modules with alternating magnetization (Left, Figure 4.8). Here, the direction of magnetization plays the same role as the n-type/p-type materials in Seebeck based thermoelectric device. The problem with such design is that the stray field produced by one module will always work against its neighboring module. As a result, there needs to be sufficient separation between each module, causing a lower energy conversion density.

The magnetic stray field produced by a bar-shape sample has been analytically solved [53]. Using the analytical formulas, I performed numerical evaluation of the magnetic stray field as shown in Figure 4.8. A module with length, width and thickness at l = 6 μm, w = 3 μm, t = 2 μm were assumed (Black solid box in Figure 4.8). The magnetization of the module is assumed to be parallel to y-axis, with strength at M_0. Following results are carried out at z = 0.5 μm. The in-plane stray fields are indicated by black arrows with $\vec{H} = (H_y, H_x)$, the color indicates the out-of-plane stray field component (H_z). In the design shown in the left panel of Figure 4.8, the y-component of the stray field is the main concern. Two spatial profiles of H_z at (x=0 μm, cut along y-axis) and (y = 2 μm, cut along x-axis) were also shown in Figure 4.8. From the spatial profile at y = 2 μm, we see that H_y is limited to [-l/2, l/2] (i.e., confined to the sample length). The stray field also decreases rapidly along the y-axis direction, with field strength reaching one-tenth of M_0 at y = 2.2 μm.

The separation distance (x) between neighboring modules depends on the magnetization and the coercive field of the candidate material. For topological magnets with no hysteresis (inset of left panel in Figure 4.9, Fe_3Sn_2), the stray field is a very serious problem since very little field is required to begin the flipping process of neighboring modules. For topological magnets with hysteresis, the ratio between its magnetization and coercive field will determine

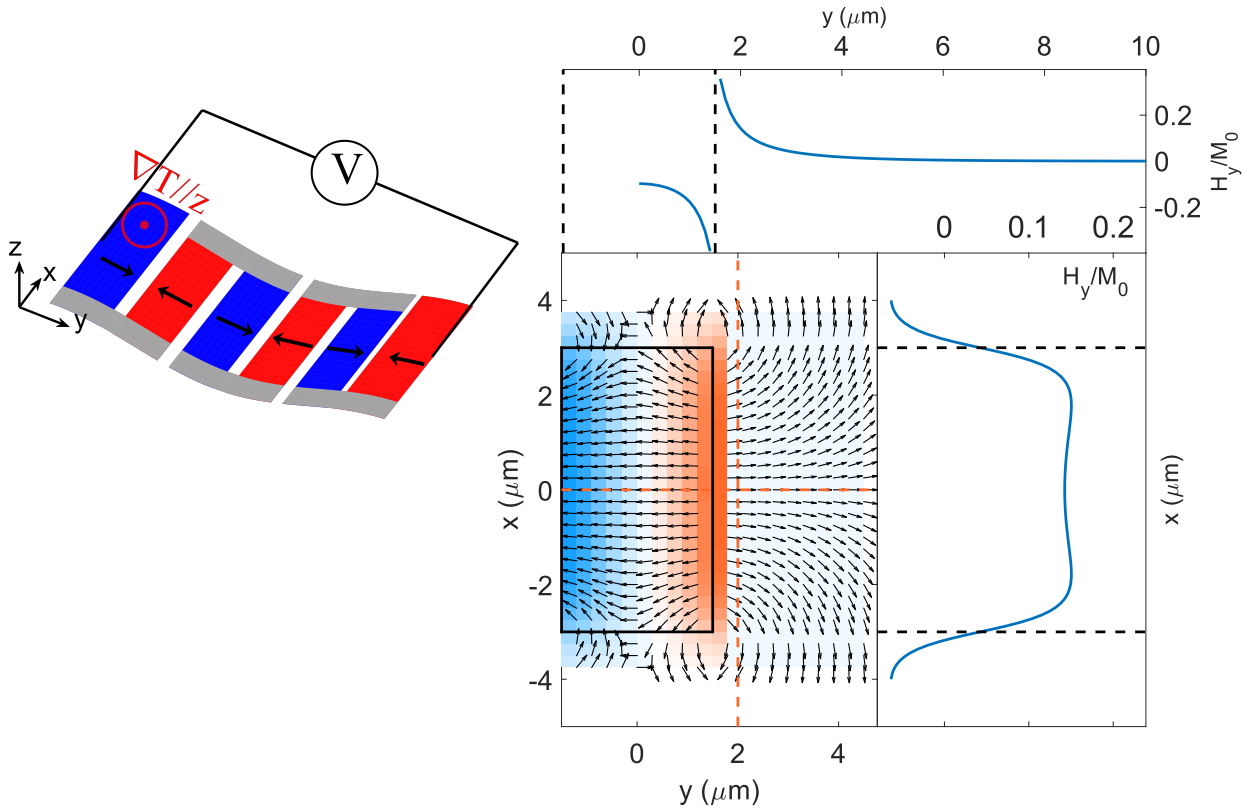

Figure 4.8: (Left) A illustration of typical design for ANE based thermoelectric device. (Right) Stray field produced by one of the module in the thermopile.

the separation distance. In Figure 4.9, the H_c/M is shown as a function of separation distance. The black dash line indicates sample boundary at x = 0.5w. In $TbMn_6Sn_6$, both the coercive field and bias-field can exceed magnetization and the minimum separation approaches zero (i.e. they could be patterned as close as desired). The same claim holds for Mn_3Sn and Mn_3Ge, with magnetization at M $\approx$ 20 Oe and coercive field at $\mu_0 H_c \approx$ 50 Oe.

Another important factor is the ANE coefficient magnitude (S_{xy}), and there is an trade-off between the two issues. While materials with large S_{xy} and small M is ideal, they are extremely rare. In conventional ferromagnets, the two are typically governed by a scaling constant between 0.05 $\mu V K^{-1} T^{-1}$ to 1 $\mu V K^{-1} T^{-1}$. For topological magnets, this scaling can be surpassed. A summary plot of $S_{xy} - M$ is shown in Figure 4.9.

Summary and future perspectives - In conclusion, we report the prominent AHE, ANE

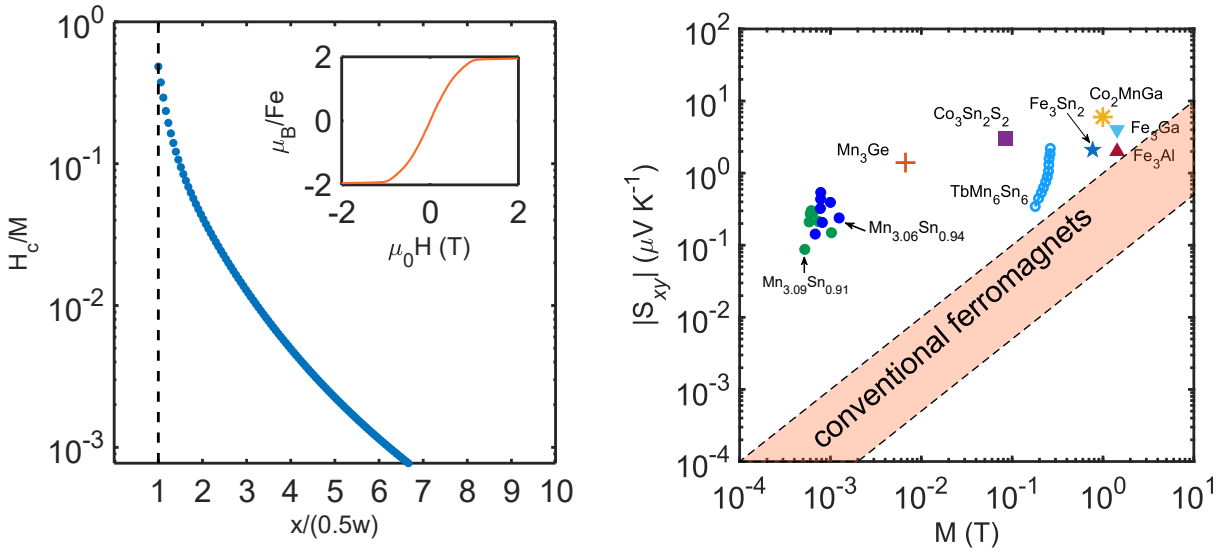

Figure 4.9: (Left) Ratio of coercive field (H_c) to magnetization (M) as a function of minimum separation distance. The separation distance is plotted in units of sample boundary. For example, at x/(0.5w) = 1 is the sample boundary. (Inset, left) Magnetization of Fe_3Sn_2 at 2 K. (Right) Summary of the $S_{xy} - M$ scaling for conventional and topological magnets.

and ATHE behavior of $TbMn_6Sn_6$ which is ferrimagnetic Kagome metal hosting a Chern gap near the Fermi level. We show that these anomalous transverse conductivities are associated with large Berry phase in the reciprocal space. Furthermore, we find that $TbMn_6Sn_6$ exhibits an exchange-bias feature in both magnetization and transverse conductivity measurements. This, combined with the large ANE, places $TbMn_6Sn_6$ as a promising system for transverse thermoelectric devices based on the Nernst effect.

An interesting further step is to make a proof-of-concept device using $TbMn_6Sn_6$. We can make a first estimate of such device. We aim to build a Nernst-based device operating at 150 K using $TbMn_6Sn_6$: $\sigma_{xx} \approx 2\ m\Omega^{-1}mm^{-1}$, $S_{xy} \approx 0.5\ \mu VK^{-1}$, $\kappa_{xx} \approx 10\ Wm^{-1}K^{-1}$. The nominal thermoelectric figure of merit z_NT for each module is approximately 0.015×10^{-3}. To reach applicable performance ($z_NT = 1$), approximately 6×10^4 modules need to be incorporated onto the device. Assuming the physical dimension for this device is at 10 cm, each module needs be made at approximately 1 μm in width. This can be easily achieve using

the current lithography technology. It is worth mentioning that such Nernst-based device with $z_N T = 1$, in theory, should operates at a much higher efficiency than its Seebeck-based counterparts [45].

Two immediate challenges that future study may address are: how to increase the Nernst coefficients (S_{xy}) and how to increase the exchange-bias field ($\mu_0 H_{EB}$). The proof-of-concept device proposed above is supposed to operate at 150 K: the temperature here is chosen to strike a balance between S_{xy} and $\mu_0 H_{EB}$. At lower temperature, S_{xy} decreases linearly, causing device performance to go down. At higher temperature, the $\mu_0 H_{EB}$ is weaken, and the stray-field from neighboring modules will cause a decrease in performance. Through chemical doping, more ideal performance of the proposed device may be achieved.

4.3 Topological Nernst effect in Fe3Sn2

Introduction - Thermoelectricity is the study of conversion between thermal and electric signals [54]. Well-known thermoelectric effects include Seebeck ($S_{\alpha\alpha}$), Nernst ($S_{\alpha\beta}$), Peltier ($\Pi_{\alpha\alpha}$) and Ettingshausen ($\Pi_{\alpha\beta}$) [54]. In thermoelectric material research, the primary focus has been on exploring materials hosting ever larger longitudinal thermoelectric coefficients ($S_{\alpha\alpha}$ and $\Pi_{\alpha\alpha}$). Although devices with desirable energy efficiency can already be built from these materials, such devices share an unfortunate bottleneck in their designs: miniaturization problem. This can be naturally circumvented by utilizing the transverse thermoelectric effects [55]. Recently, there have been reviving interests in the anomalous Nernst effect (ANE) from the condensed matter community, following the pioneering study by D. Xiao et al [56] which showed that Berry phase in the band structure could induce anomalous thermoelectric transport.

This section is adapted from [21]. Chunqiang Xu synthesized the material. Chunqiang Xu and I performed the measurements and analyzed the data. Xianglin Ke and I wrote the manuscript with comments from Chunqiang Xu. Xianglin Ke supervised the project.

In contrast to the normal Nernst effect which is proportional to the applied magnetic field, anomalous Nernst signal emerges when charge carriers acquire an anomalous transverse velocity in the presence of a longitudinal temperature gradient and a finite Berry phase [56]. In this respect, ANE is a thermoelectric counterpart of the anomalous Hall effect (AHE), both of which are associated with the Berry curvature in the momentum space [57]. On the one hand, ANE and AHE are intimately related to each other via anomalous thermoelectric linear response tensor α^A. On the other hand, compared to AHE which probes the Berry curvature of the whole Fermi sea, ANE is sensitive to the Berry curvature near the Fermi surface. As a result, ANE may become the dominant term of the total Nernst signal in topological semimetals with an enhanced Berry curvature near the Fermi energy. For instance, large ANE has been observed in Dirac and Weyl semimetals, such as $Co_3Sn_2S_2$ [58], Cd_3As_2 [59], Co_2MnGa [60], which offer promising applications as the new generation of thermoelectric energy conversion devices. In addition to the normal and anomalous Nernst effect, a third potential contribution to the Nernst signal is coined as topological Nernst effect (THE). THE is by far the most elusive phenomenon among these three possible contributors. Up to date it has been only observed in MnGe [61] and Gd_2PdSi_3 [62], both of which were attributed to Berry phase in real space associated with non-zero spin chirality arising from the field-induced magnetic skyrmion lattice.

In this section, we report comprehensive electrical, thermal and thermoelectric measurement results on Fe_3Sn_2, a three-dimensional frustrated ferromagnetic Kagome metal hosting massive Dirac fermion [63]. We show that anomalous thermal and thermoelectric response

are present in Fe_3Sn_2, in addition to the previously reported AHE. We find that Fe_3Sn_2 exhibits TNE in the low field regime above 120 K, which is attributable to the skyrmion bubble phase revealed by Lorentz transmission electron microscopy (TEM) [64, 65]. Furthermore, we observe prominent thermal Hall effect and large anomalous Nernst signal (2.1 μV/K at room temperature), a value that is comparable to the largest ANE observed thus far [66, 67, 58, 60, 55]. The corresponding anomalous thermoelectric linear response tensor α^A is found to increase with temperature, reaching a value of around 1 A/m K at room temperature. These features highlight the synergic effects of Berry phase in both real and momentum space in Fe_3Sn_2.

Results - Fe_3Sn_2 crystalize in the trigonal crystal system, space group R-3m (No. 166), with crystal constants at a = b = 5.338 Å, c = 19.789 Åand crystal angles at α=β=90°, γ=120°. The crystal structure of Fe_3Sn_2 is shown in Figure 4.10 (a), wherein iron atoms are represented by red spheres and tin atoms are represented by blue spheres. The iron atoms form a double-layer kagome lattice, which hosts topological flat bands and Dirac fermions [68, 69, 63]. Neutron powder diffraction measurement showed that while Fe_3Sn_2 is ferromagnetic, its spin Hamiltonian is frustrated within the Kagome plane, which resulted in non-collinear spin structures [70]. Recently, skyrmion bubble states were directly observed in Fe_3Sn_2 by Lorentz TEM [65]. Regarding its electronic properties, large anomalous Hall conductivity σ_{xy}^A was observed, which contains a nearly temperature-independent, intrinsic anomalous Hall conductance σ_{xy}^{int} on the order of 0.27 e^2/h per Kagome bi-layer (250 Ω^{-1} cm^{-1}). In addition, ARPES study revealed the existence of two Dirac points at E = -70 meV and E = -180 meV below the Fermi energy, which were argued to be responsible for the intrinsic anomalous Hall conductance [63].

Fe_3Sn_2 single crystals were grown using the chemical vapor transport (CVT) method [63].

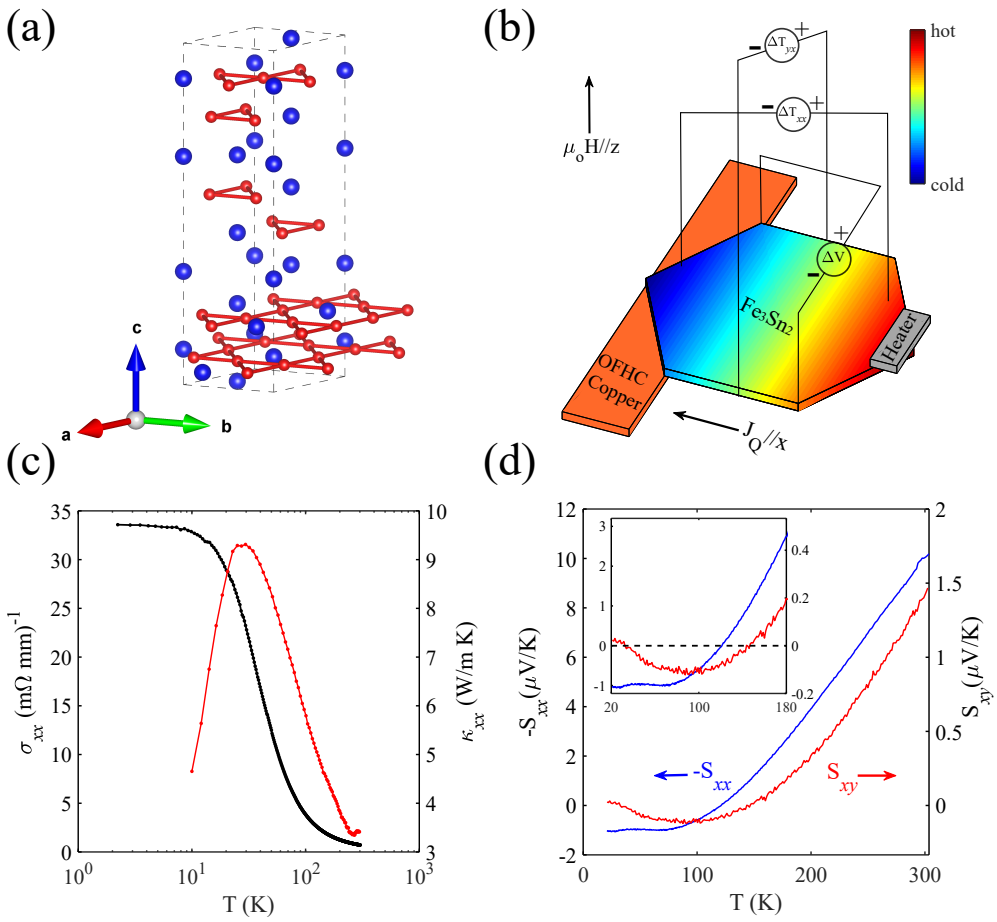

Figure 4.10: (a) Schematic crystal structure of Fe_3Sn_2; iron atoms are represented by red spheres forming Kagome planes, tin atoms are represented by blue spheres. (b) Illustration of the experimental set-up. The temperature gradient is indicated by color scale, the heat sink used is oxygen free high conductivity (OFHC) copper, and the heater used is a thin film resistor (1 kΩ) (c) Temperature dependence of longitudinal electrical (σ_{xx}, black) and thermal (κ_{xx}, red) conductivities. (d) Temperature dependence of Seebeck (blue) and Nernst (red, 1.5 T) coefficients. Inset shows an expanded view below 160 K.

Magnetic susceptibility measurements of Fe_3Sn_2 were carried out using a Superconducting Quantum Interference Device (SQUID) magnetometer from Quantum Design. Resistivity and Hall effect measurements were conducted using a Physical Property Measurement System (PPMS) from Quantum Design. Thermoelectric measurements were performed using a homemade sample puck designed to be compatible with the PPMS cryostat. For temperature below 40 K, calibrated Cernox sensors were used to measure the temperature gradient,

while type-E (Chromel-Constantan) thermocouples were used for temperature above 10 K up to room temperature. The thermoelectric voltage was measured using K2182A Nanovoltmeters. An illustration of the experimental set up is shown in Figure 4.10 (b). The sample is attached to a piece of oxygen-free high conductivity copper used as the heat sink using silver epoxy. A heater (1 kΩ resistor) is attached to the other end of the sample and applies heat current J_Q parallel to the a-axis. The magnetic field is applied along the out-of-plane direction (c-axis). The (Nernst/)Seebeck coefficients are obtained by (anti-)symmetrizing the thermoelectric voltages measured in the presence of positive and negative field separately.

We first present temperature dependence of electronic and thermal transport properties of the Fe_3Sn_2 sample measured in this experiment. Figure 4.10 (c) shows the longitudinal electrical conductivity (σ_{xx}, black) and thermal conductivity (κ_{xx}, red) measured as functions of temperature. The sample exhibits metallic transport behavior down to T = 2 K with a residual resistance ratio [RRR = ρ(300K) / ρ(2K)] of 46.7, indicating good crystal quality. And κ_{xx} shows a characteristic broad peak around T = 26 K, which arises from the competition between the Umklapp phonon scattering dominating at high temperature and the phonon scattering by defects dominating at low temperature. Note that the measured κ_{xx} is slightly larger than the value calculated based on the Wiedemann-Franz law [71, 72], suggesting the loss of heat current due to inelastic phonon scattering. In Figure 4.10 (d) we present the temperature dependence of Seebeck ($S_{xx} = -\partial_x U/\partial_x T$) coefficient, wherein U is the thermoelectric voltage and T is the measured temperature. A sign change of S_{xx} at T = 110 K can be clearly seen in the inset of Figure 4.10 (d). The sign change of S_{xx} has been described previously by Q. Du et al [64]. It is the result of two competing components in the total S_{xx}: the electron diffusion contribution (negative, dominant at high temperature) and the phonon drag contribution ($\propto T^{2.67}$, positive, dominant at low temperature) [64].

Overall, these features in the temperature dependence of σ_{xx}, κ_{xx}, and S_{xx} are similar to the observations in recent reports [64, 70, 63] , affirming good quality of our sample. In Figure 4.10 (d) we also plot the first measurement of Nernst coefficient [$S_{xy} = \partial_y U/\partial_x T$] of Fe_3Sn_2 as a function of temperature. Here the sign of Nernst coefficient follows the Bridgman's "Ampere current" conventions [73, 59], that is, the vector cross product of magnetic field ($\vec{B}$) and heat current ($\vec{J_Q}$) is parallel to the Nernst electric field ($\vec{E}_N$). One can see that S_{xy} changes the sign at T = 145 K. As to be discussed latter on based on the field dependent S_{xy} measurements, such a sign change in S_{xy} arises from the competition between the normal Nernst effect and the anomalous Nernst effect.

Next, we discuss the field dependence of longitudinal thermoelectric and other thermal responses of Fe_3Sn_2. Figure 4.11 (a-b) show the field dependent $-S_{xx}/T$ and κ_{xx} measured at various temperatures, respectively. Interestingly, both these two longitudinal quantities exhibit similar field dependent behaviors: there is a broad peak in the low field region at low temperatures (below 200 K) while both longitudinal quantities are nearly field independent at high temperatures (also seen in Fig. S1(b-c) [21]). Similar feature in thermopower behavior was observed recently [64], although the signal reported is not as clear as the data shown in Figure 4.11 (a). The broad peak feature was presented as a signature of skyrmion bubbles existing in Fe_3Sn_2, since the gained entropy associated with the formation of skyrmion bubble lattice enhances S_{xx} by providing an extra driving force to the thermal diffusion of conduction electrons [64]. The formation of skyrmion bubbles in the low field region is presumably responsible for the broad peak observed in σ_{xx} as presented in Fig. S1(a) [21], via the spin-scattering process, a feature that is consistent with an early report [74]. Intriguingly, as shown in Figure 4.11 (b) and Fig. S1(c-d) [21], κ_{xx} (H) shows a hump feature in low field region at 100 K $<$ T $<$ 250 K while it monotonically decreases at low field prior to near

saturation at T < 100 K. Such a field dependent κ_{xx} suggests that various quasiparticles of this system, including phonon, electron, magnon, and skymion, play a non-negligible role in thermal transport in different field-temperature regions. For instance, the hump feature in the low field region at 100 K < T < 250 K can be related to the skyrmions either by serving as heat carrier or via the electron/phonon-skyrmion interaction.

Now we focus on the transverse responses (S_{xy}, κ_{xy}) and their relation to the Berry phase of Fe_3Sn_2, as shown in Figure 4.11 (c-d). In addition to the normal term that is linearly proportional magnetic field, for topological materials there is an anomalous contribution to the transverse electric, thermoelectric and thermal responses that arises from an intrinsic mechanism associated with the Berry curvature. Compared to the vast amount of studies of AHE [57], ANE has only recently emerged as another sensitive probe in identifying topological semimetals [58, 60, 59, 75, 76, 77, 56, 78], and anomalous thermal Hall effect has only been observed in a few topological semimetals recently [79, 80]. Figure 4.11 (c) presents the field dependence of S_{xy} /T measured at various temperatures. Similar to the σ_{xy} shown in Fig. S2(a-b) [21], at high temperatures the Nernst signal is dominated by an anomalous contribution ($\propto$ M), which saturates near 0.8 T. At lower temperatures, the contribution from normal Nernst effect ($\propto$ H) dominates in the high field regime, as evidenced by the linearly increasing negative value at high field. Interestingly, in the low field region, a clear broad hump emerges at 100 K < T < 200 K, the origin of which will be discussed next. Note that the competition between normal Nernst effect and ANE leads to the sign change at T = 145 K in S_{xy} measured at 1.5 T magnetic field as plotted in Figure 4.11 (d). The field dependent thermal Hall effect $\kappa_x y$ (H) is shown in Figure 4.11 (d). Only anomalous thermal Hall component is present, which increases with temperature and reaches a value of around 0.086 W/mK. Anomalous thermal Hall effect have been observed in other topological

materials such as Mn_3Sn, Co_2MnGa [79, 80]. The anomalous transverse thermal response is the result of Berry curvature summed over the inverse of thermal de Broglie length of electrons ($\lambda = h/\sqrt{2\pi m k_B T}$) [80]. AHE feature has also been observed in Fe_3Sn_2 previously [81, 63] and is shown in Fig. S2 [21]. All these (electric, thermoelectric, thermal) transverse transport coefficients are dominated by anomalous contributions.

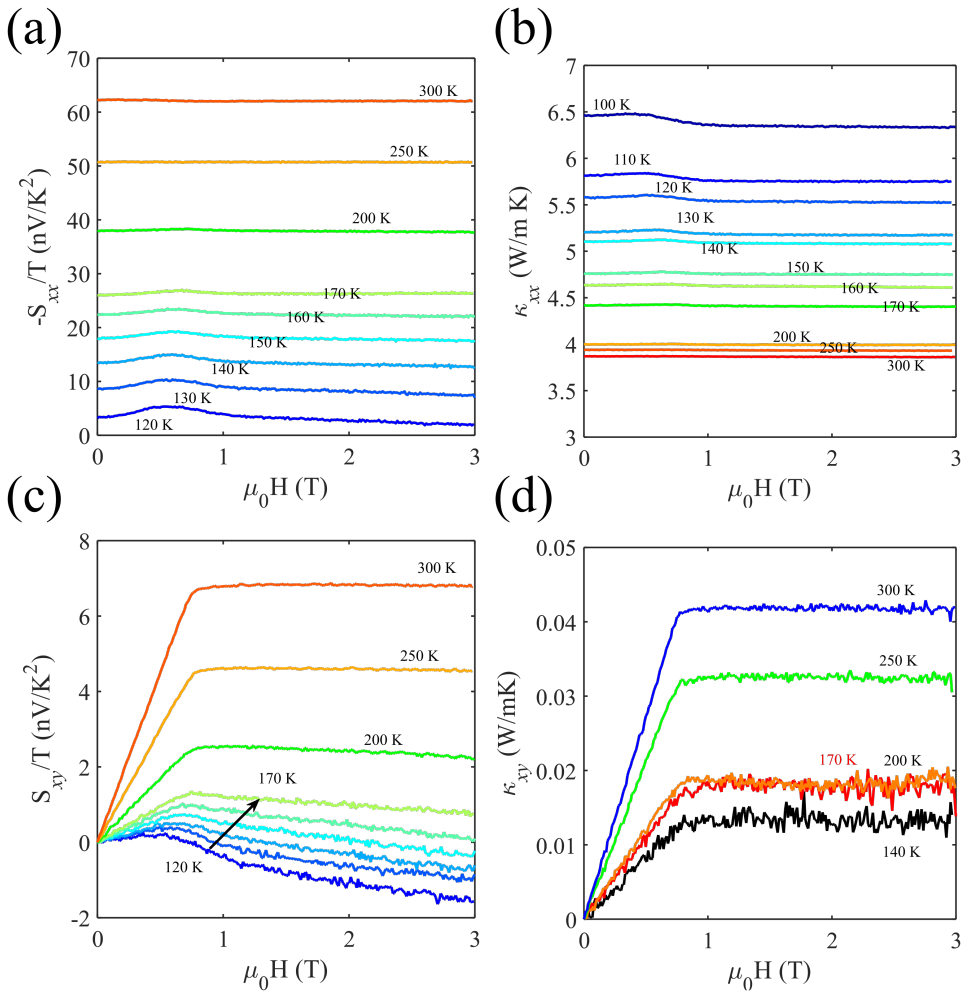

Figure 4.11: Magnetic field dependence of Seebeck coefficient scaled by temperature -S_{xx}/T (a) and thermal conductivity κ_{xx} (b); Magnetic field dependence of Nernst coefficient scaled by temperature S_{xy}/T (c) and thermal Hall conductivity κ_{xy} (d). Data were measured at various temperatures.

Topological Nernst - The origin of the hump feature observed in Nernst measurement at the low field region shown in Figure 4.11 (c) presents a puzzle. By performing linear fitting

using the high field data, we subtract the contribution from the normal Nernst effect. The obtained ΔS_{xy}/T is shown in Figure 4.12 (a). The broad hump feature at low temperatures (e.g., T = 120 K) is clearly confined to magnetic field smaller than 1 T. Note that 1 T is the upper limit of skyrmion bubble phase observed in the Lorentz TEM experiment [65, 82]. This observation should not be coincidental; instead, this feature is the result of electron-skyrmion interactions [83]. Since the skyrmion bubble phase persists up to room temperature, we anticipate that there should be topological contribution in the observed Nernst signal even though ΔS_{xy} is dominated by the anomalous term at high temperature. To verify this conjecture, the magnetization data M(H) measured at T = 300 K is overplotted in Figure 4.12 (a) as thick black dashed line [additional magnetization data measured at various temperatures are shown in Fig. S4(b) [21]]. By comparing ΔS_{xy} /T(H) and M (H) curves measured at 300 K, it is clear that there is a topological contribution to the observed Nernst signal in the low field region. Assuming the proportionality of anomalous Nernst signal to the magnetization at the same temperature, we further subtract the anomalous Nernst contributions to extract the topological Nernst signal S_{xy}^{T}/T which is shown in the left panel of Figure 4.12 (b). To the best of our knowledge, there have only been two clear-cut reports on TNE, one on MnGe (T_N=150 K) and another on Gd_2PdSi_3 (T_N 22 K). Compared to the two previous reports [62, 61], Fe_3Sn_2 is a high-temperature frustrated ferromagnet, whose skyrmion phase region expands well above room temperature [64, 65].

Considering the skyrmion bubble lattice in Fe_3Sn_2, topological Hall effect (THE) is also anticipated. Indeed, THE has recently been reported by Li et al [81]. In order to study the thermoelectric linear response tensor (to be discussed latter on), in the right panel of Figure 4.12 (b) we plot the topological Hall resistivity ρ_{yx}^{T} after subtracting the both normal Hall effect and AHE components (see Fig. S2 [21]), which is consistent with the previous

report [81]. Remarkably, S_{xy}^T/T and ρ_{yx}^T seem to have a simple scaling constant between them (0.137 A/m K^2) in the temperature range between 200 K to 300 K. The unit of this constant is the same as that of thermoelectric linear response tensor divided by temperature, α/T. This simple proportionality suggests a common origin for the two observed topological responses in electric and thermoelectric sectors of Fe_3Sn_2, which is presumably attributed to non-zero Berry curvature arising from the non-zero spin chirality of the skyrmion spin structure. In contrast, the two topological responses S_{xy}^T /T and ρ_{yx}^T at lower temperatures (T = 150 K and 120 K) exhibit rather different behaviors. At T = 150 K, there is a sign change in TNE, while THE maintains the same sign. At T = 120 K, ρ_{yx}^T is barely detectable, whereas the S_{xy}^T/T still shows a broad peak with a positive amplitude of around 0.4 nV/K^2. As noted in the introduction and many other review papers [84, 56], the 'drive' for thermoelectric response is a temperature gradient, a macroscopic, statistical force; on the other hand, the 'drive' for electrical response is a voltage gradient, a microscopic, electro-mechanical force. Thus, the difference in behavior of S_{xy}^T and ρ_{yx}^T at low temperature is naturally anticipated. To fully understand these topological responses, especially the thermoelectric topological response S_{xy}^T, one needs to take into account the electron-skyrmion interactions in the Boltzmann transport theory, which calls for future theoretical investigation.

The observation of both anomalous and topological components in Hall effect and Nernst effect measurements, together with the simple scaling between TNE and THE at high temperature, raises an intriguing issue regarding the thermoelectric linear response tensor $\bar{\alpha}$, a revealing quantity in the study of magnetic topological semimetals which incorporates anomalous contributions from both AHE and ANE [77]. In a typical thermoelectric measurement set-up, there is no electric current flowing through the material, i.e., $\vec{J} = \bar{\sigma}\vec{E} + \bar{\alpha}(-\nabla T)$=0.

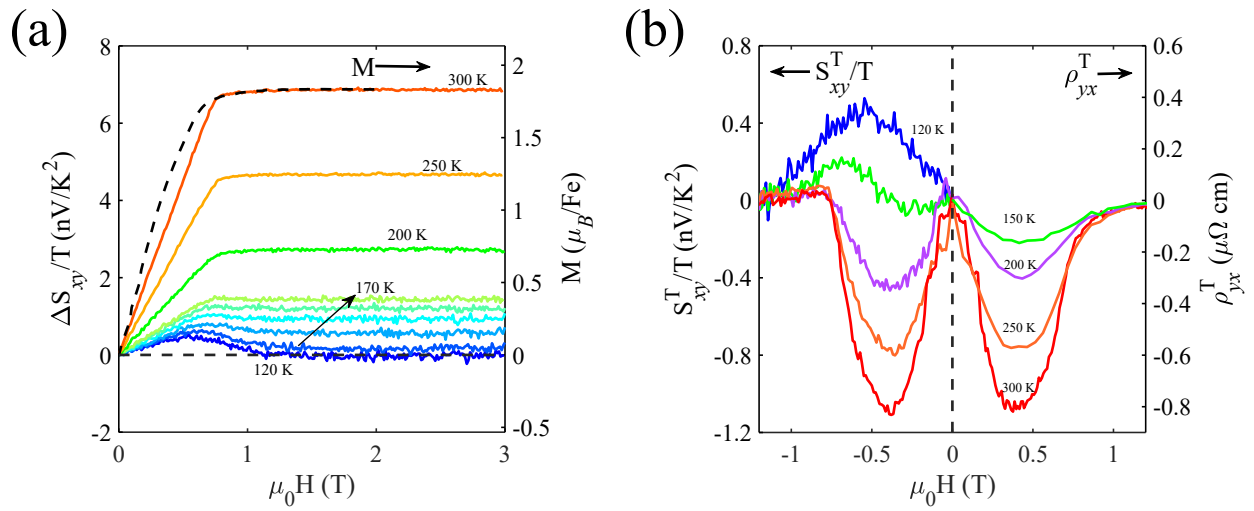

Figure 4.12: (a) Magnetic field dependence of residual Nernst coefficient measured at various temperatures after subtracting the normal Nernst coefficient ($\propto$ H). The magnetization (H$\|$c) data measured at 300 K is overplotted as the dashed line. The saturated magnetization is about 1.8 μ_B/Fe. (b) Magnetic field dependence of topological Nernst coefficient (left) and Hall resistivity (right) after subtracting out the anomalous contribution ($\propto$M).

By defining another tensor $\bar{S} = \begin{pmatrix} S_{xx} & S_{xy} \\ S_{yx} & S_{yy} \end{pmatrix} = \begin{pmatrix} E_x/\partial_x\ T & E_y/\partial_x\ T \\ E_x/\partial_y\ T & E_y/\partial_y\ T \end{pmatrix}$, one obtains $\bar{\alpha} = \bar{\sigma}\bar{S}$ [59]. Specifically, here we measure the in-plane thermoelectric linear response tensor $\alpha_{xy} = \sigma_{xx}\ S_{xy} + \sigma_{xy}\ S_{xx} = \alpha_1 + \alpha_2$ [58]. By replacing S_{xy} with $\Delta S_{xy} = S_{xy}$ - S^o_{xy} and σ_{xy} with $\Delta\sigma_{xy} = \sigma_{xy} - \sigma^o_{xy}$, where S^o_{xy} and σ^o_{xy} represent normal Nernst coefficient and Hall conductivity respectively, we plot the residual thermoelectric linear response tensor $\Delta\alpha_{xy}$/T in Figure 4.13 (a). At high temperature, $\Delta\alpha_{xy}$/T is dominated by the anomalous part α^A_{xy}/T, which is directly proportional to the integrated Berry curvature at the Fermi surface [77]. In contrast, at low temperature $\Delta\alpha_{xy}$/T is dominated by the topological contribution, α^T_{xy}, which is a manifestation of Berry curvature in real space due to the underlying skyrmion bubble phase [85].

Finally, we present the evolution of thermoelectric quantities extracted at 1.5 T (above the saturation field) as function of temperature, as shown in Figure 4.13 (b-d). In Figure 4.13

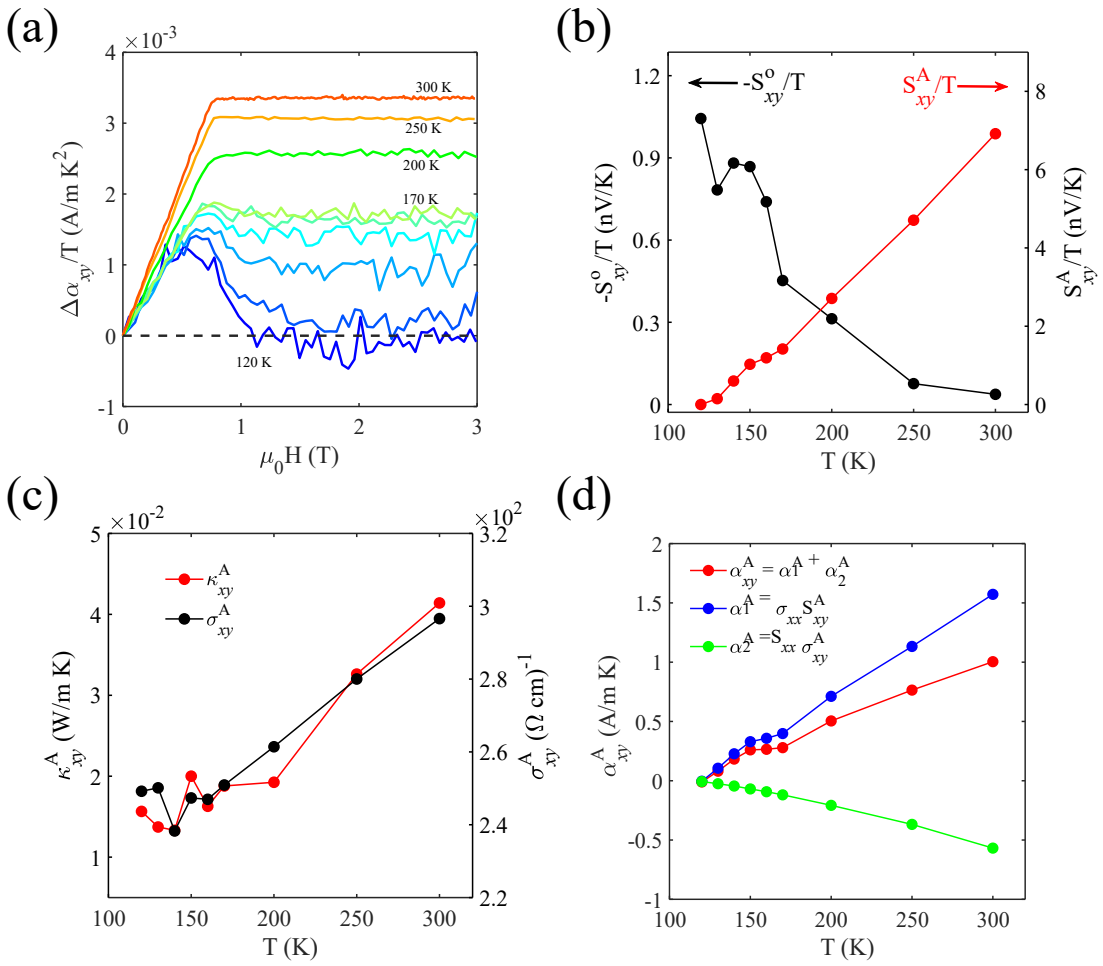

Figure 4.13: (a) Residual thermoelectric linear response tensor scaled by temperature $\Delta\alpha_{xy}/\mathrm{T}$ after subtracting the normal Nernst coefficient. (b) Normal and anomalous (1.5 T) Nernst coefficient scaled by temperature. (c) Anomalous thermal and electric Hall conductivity (1.5 T) as a function of temperature. (d) Temperature dependence of Total anomalous thermoelectric linear response tensor (α^A_{xy}) and its two components (α^A_1,α^A_2).

(b), we see that the normal Nernst coefficient and the ANE coefficient have opposite trends. Generally speaking, the ordinary Nernst effect positively correlates with carrier mobility [54]. Thus, the normal Nernst effect becomes stronger as the carrier mobility increases at low temperature. On the other hand, the ANE is independent of carrier mobility, in some cases even amplified by disorder in the system [58]. This is because the intrinsic contributions of S^A_{xy} is not affected by defects but depends on the integrated Berry curvature in the momentum space near the Fermi level [58]. Thus, S^A_{xy} is sensitive to both Fermi energy and

temperature via the Fermi distribution function. It is likely that, within the measurement temperature range, the enhanced thermal fluctuation or the closer energy spacing between the field-induced Weyl nodes and the chemical potential with the increase of temperature leads to larger contribution from the Berry curvature [66, 77]. As a result, here S_{xy}^{A} continues to increase linearly even up to 300 K, suggesting that an even larger Nernst signal is anticipated at high temperatures, which is consistent with the presence of two Dirac points revealed by ARPES with one of them positioning at E = -70meV below the Fermi energy [63]. The increase of S_{xy}^{A} as a function of temperature has been recently observed in other magnetic topological semimetals [58, 76]. In Figure 4.13 (c) we plot the temperature dependence of σ_{xy}^{A} and anomalous thermal Hall conductivities (κ_{xy}^{A}) extracted at 1.5 T. Similar to S_{xy}^{A}/(T), both σ_{xy}^{A} and κ_{xy}^{A} increase with temperature, suggesting a common mechanism of all these three anomalous electronic, thermoelectric and thermal responses in this system. Figure 4.13 (d) presents the temperature dependence of thermoelectric linear response tensor α_{xy}^{A} and its two components $\alpha_{1}^{A} = \sigma_{xx} S_{xy}^{A}$ and $\alpha_{2}^{A} = S_{xx} \sigma_{xy}^{A}$. Note that the signs of α_{1}^{A} and α_{2}^{A} are determined by the transverse and longitudinal components of Seebeck coefficients respectively, which needs to be taken into account when calculating the total α_{xy}^{A} [58, 78]. Recent theory study by Papaj and Fu [75] predicted $\alpha_{xy}^{A}|_{T=80K} = 0.67$ A/mK for Fe_3Sn_2, whereas our experiment showed that α^{A} reaches this value at T = 240 K. This inconsistency may be associated with the level of disorder used in theoretical calculation compared to the actual value in our sample [75]. To put these data in perspective, we note that among high-temperature magnetic semimetals, the largest ANE was observed in Co_2MnGa, with $S_{xy}^{A}|_{T=300K} \approx 6$ μV/K and $\alpha_{xy}^{A}|_{T=300K} \approx 2.8$ A/m K. In comparison, the Fe_3Sn_2 sample measured here has $S_{xy}^{A}|_{T=300\ K} \approx 2.1$ μV/K and $\alpha_{xy}^{A}|_{T=300K} \approx 1$ A/m K. These results place Fe_3Sn_2 as one of the materials with large anomalous thermoelectric coefficients.

Summary and future perspectives - In conclusion, we have observed a large anomalous Nernst signal (2.1 μV/K at 300 K) in Fe_3Sn_2, a value that is comparable to the largest value reported thus far. The temperature and field dependence of this Nernst signal was investigated: it is the manifestation of Berry curvatures both in real and reciprocal space. At high temperature, the Nernst signal is dominated by the anomalous contribution, the magnitude of which is proportional to the integrated Berry curvature near the Fermi surface in the momentum space. At lower temperatures, the Nernst signal is dominated by a topological term, restricted to the low field region where the skyrmion bubble phase is present, associated with the Berry curvature in real space generated by the underlying skyrmion lattice. This study demonstrates an effective strategy of investigating topological materials by measuring their transverse thermal and thermoelectric responses at different temperatures and magnetic fields.

To the best of my knowledge, topological Nernst effect has only been observed in a handful of materials, all of which host magnetic skyrmions [61, 62]. These are topologically protected magnetic textures whose physical dimensions range from nm to μm. Electrical control of these magnetic textures is being actively pursued. Alternatively, investigation into how skyrmions behave in the presence of thermal gradients may be an interesting future direction. For example, a recent experimental work demonstrated real-space observations of skyrmion dynamics in Cu_2OSeO_3 using Lorentz transmission electron microscopic [86]. In this study, the skyrmions are driven by a small thermal gradient, instead of an electric field. A similar approach may be applied to Fe_3Sn_2, which hosts skyrmion bubbles with larger dimensions and lower density [65].

Chapter 5

Quantum spin chains in Cu2(OH)3Br

This chapter is adapted from [22]. Z. Zhao synthesized the material. Huibo Cao and I performed the neutron neutron diffraction experiment. Tao Hong, Ovidiu Garlea and I performed the inelastic neutron scattering experiment. I performed magnetic susceptibility and heat capacity measurements. I analyzed the experiment data. D. Gautreau and A. Saha performed density functional theory calculations with help from Turan Birol. M. Raczkowski performed quantum Monte Carlo simulations with help from F. F. Assaad. H. O. Jeschke and Subhendra D. Mahanti wrote the analytic form of the random phase approximated (RPA) equations. I implemented numerical evaluations of the RPA equations. Xianglin Ke and I wrote the manuscript with inputs from all authors.

5.1 Introduction

In conventional magnets with magnetic long range order (LRO), low-energy excitations are carried by spin waves, represented by massless bosons called magnons with S = 1 [87]. However, in one-dimensional (1D) antiferromagnetic quantum spin systems, quantum fluctuations destroy LRO in the ground state. Such systems cannot be described using mean-field theory such as the standard Landau-Ginzburg-Wilson theory [88]. As a result, the low-energy excitations in these systems behave quite differently from their higher-dimensional counterparts. One of the prototypical systems is the Heisenberg antiferromagnetic quan-

tum spin-1/2 chain, where the low-energy excitations are carried by pairs of deconfined spinons [89, 90, 91, 92, 93, 94, 95, 96, 97, 98, 99, 100, 101, 102]. In contrast to magnons, spinons possess fractional spin S = 1/2 which could be thought of as propagating domain walls [91, 92]. On the other hand, materials hosting ferromagnetic quasi-1D spin-1/2 chains are quite rare and the magnetic quasiparticles of ferromagnetic quantum spin chains are magnons [103, 104]. Importantly, interaction between different quasiparticles has been an exciting research topic. In many cases, such interactions often lead to novel electronic and magnetic phenomena. For instance, electron-phonon interaction plays an essential role in the formation of Cooper pairs in conventional superconductors [105], while magnons have been proposed as the glue for Cooper pairs in unconventional superconductors [106]. In some metallic magnets, it has been found that electron-skyrmion interactions give rise to topological Hall effect [107], which provides a new route for spintronic applications. However, up to date there is no report on the interaction between two different types of magnetic quasiparticles. In this chapter, we report our observation of the coexistence and interaction of spinons and magnons in a quasi-1D antiferromagnetic insulator $Cu_2(OH)_3Br$ using inelastic neutron scattering measurements. These two different magnetic quasiparticles arise from the peculiar orbital ordering and spin structure of $Cu_2(OH)_3Br$, which consists of nearly decoupled, alternating antiferromagnetic and ferromagnetic chains of Cu^{2+} ions with spin-1/2. The antiferromagnetic chains support spinons and the ferromagnetic chains support magnons. Using both quantum Monte Carlo (QMC) simulations and Random Phase Approximation (RPA) calculations, we demonstrate evidence of magnon-spinon interactions via the weak but finite interchain couplings. To the best of our knowledge, such an interaction between two different magnetic quasiparticles has not been investigated even in theory due to the unusual nature of the spin structure. Our study thus opens up a new research arena and

calls for further experimental and theoretical studies.

5.2 Results

Figure 5.1 (a, b) depict the crystal structure of $Cu_2(OH)_3Br$, which is indicative of quasi-two-dimensional nature with the neighboring Cu-Cu distance along the c-axis much larger than those in the ab plane. The Cu^{2+} magnetic ions in the ab plane form a distorted triangular lattice with two inequivalent Cu sites: Each Cu1 site has 4 Cu-O bonds and 2 Cu-Br bonds while each Cu2 site has 5 Cu-O bonds and 1 Cu-Br bond. As will be discussed later, the differences in the local geometry (caused by the ordering of Br ions) of these two Cu sites are crucial: they determine the nature of orbital ordering (partially occupied d orbitals) of Cu1 and Cu2 and the sign of nearest-neighbor intra-chain exchange interactions between Cu moments, Cu1-Cu1 and Cu2-Cu2.

Heat capacity and magnetic susceptibility measurements [inset of Figure 5.1 (c)] on a single crystal sample reveal a paramagnetic-antiferromagnetic phase transition at $T_N \approx$ 9.0 K, in agreement with previous reports [108, 109]. The main panel of Figure 5.1 (c) plots the temperature dependence of neutron diffraction intensity of ordering wave vector (0.5 0 0), affirming the antiferromagnetic nature of the magnetic long-range ordered state. The magnetic structure determined by Rietveld refinement (FullProf) [110] (Fig. S1 [22]) is presented in Figure 5.1 (d). Along the b-axis, Cu1 spins align ferromagnetically with spins oriented nearly along the diagonal direction in the ac-plane, while Cu2 spins align anti-ferromagnetically with spins oriented along the a-axis. The nearest-neighbor spins of both Cu1 and Cu2 sites along the a-axis are antiparallel, as suggested by the ordering wave vector. The ordered moment for Cu1 and Cu2 sites are $\approx 0.737(6)\ \mu$B and $\approx 0.612(2)$

μB respectively; both of these values are smaller than the full saturation value of 1 μB for spin-1/2, resulting from strong quantum fluctuation.

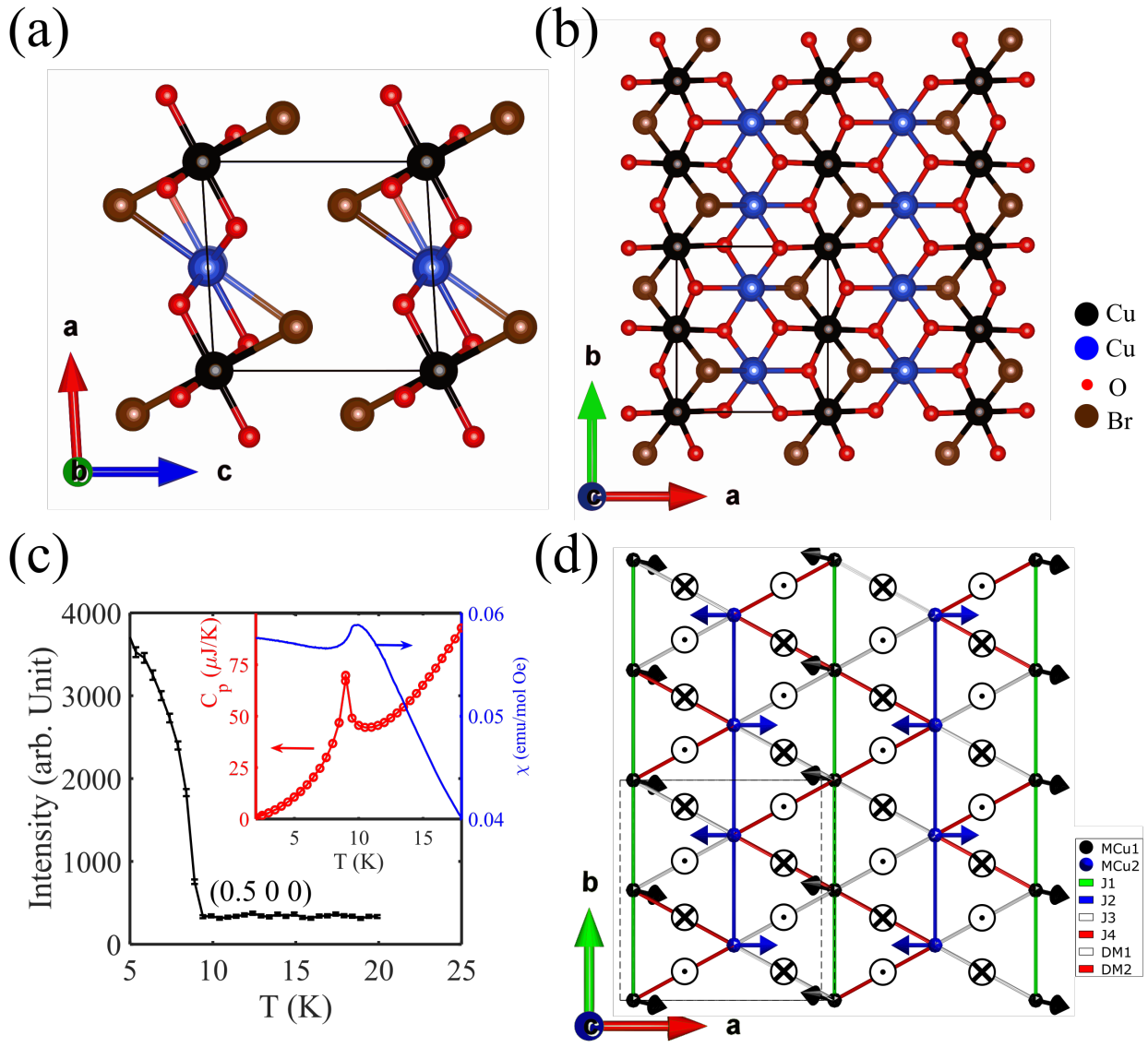

Figure 5.1: Crystal structure and magnetic structure of $Cu_2(OH)_3Br$. Crystal structure of $Cu_2(OH)_3Br$ in the ac (a) and ab (b) plane showing a quasi-two dimensional, distorted triangular lattice of Cu atoms. (c) Temperature dependence of neutron diffraction intensity of an ordering wave vector (0.5 0 0). The inset shows the temperature dependence of heat capacity and magnetic susceptibility measurements. (d) Spin structure of Cu^{2+} ions with Cu2 spins point along the a-axis while Cu1 spins pointing nearly along the diagonal direction in the ac plane. Exchange interactions of Cu1-Cu1, Cu2-Cu2, and Cu1-Cu2 as well as DM interaction are denoted.

To investigate the nature of the spin dynamics, we performed inelastic neutron scattering

measurements on co-aligned single crystals in the (H K 0) scattering plane using the HYSPEC time-of-flight spectrometer at Spallation Neutron Source [111]. Intriguingly, we find that this system shows quasi-1D nature of the exchange interactions as seen in the momentum- and energy-resolved neutron scattering intensity maps presented in Figure 5.2 (a-c). The nearly dispersionless behavior of the excitation spectrum along both H [Figure 5.2 (a)] and L [Figure 5.2 (b)] directions indicates weak coupling between Cu spins along both a- and c-axes. In contrast, the I(E, K) intensity map (integrated over all H and L) presented in Figure 5.2 (c), shows unusual excitation features with well-defined magnon dispersion and broad continuum above $\approx$ 5 meV. These observations, combined with the refined spin structure shown in Figure 5.1 (d), demonstrate that this system consists of nearly-decoupled, alternating ferromagnetic and antiferromagnetic chains. To the best of our knowledge, $Cu_2(OH)_3Br$ is the only system discovered thus far to exhibit the coexistence of quasi-1D ferromagnetic and antiferromagnetic quantum spin chains.

As an initial attempt to understand the magnetic excitations of this system, we performed Linear Spin Wave (LSW) calculations using SpinW [112]. The model magnetic Hamiltonian (H) [22] consists of nearest neighbor Heisenberg-Ising type exchange couplings with intra-chain interactions (J1 and J2), interchain interaction (J3, J4) and Dzyaloshinskii-Moriya (DM) interaction (D) [Figure 5.1 (d)]. The dominant interactions are J1 (ferromagnetic), J2 (antiferromagnetic) whereas J3 and J4 are antiferromagnetic and small. The LSW fitting spectra are shown in Figure 5.2 (c, d) and the fitting parameters are J1 = -2.6 meV, J2 = 9.9 meV, J3 = 1.2 meV, J4 = 0.3 meV and D = 1.0 meV. The anisotropy parameter of interchain interactions is are ΔF= 0.173 for J1 and ΔAF=0.045 for J2, and the DM term is on the interchain bonds between Cu1 and Cu2 [22]. The good agreement between the experimental data and the LSW results reassures us that this system indeed is composed of

quasi-1D ferromagnetic and antiferromagnetic alternating chains. The lower-energy branches associated with ferromagnetic chains have an energy gap of ≈1.2 meV at the zone center (e.g. K = 0), while the higher-energy branches associated with antiferromagnetic chains have an energy gap of ≈4.2 meV at the zone center (e.g., K = -1). These spin gaps arise from anisotropic exchange interactions and finite interchain coupling and the spectral gap in the ferromagnetic branch around 3.5 meV at K = -0.5 and -1.5 arises from the DM interaction.

As discussed in the introduction, the excitations of (quasi-) 1D spin-1/2 antiferromagnets are spinons instead. As a result, one expects a broad continuum produced by pairs of spinons, which cannot be described within the framework of LSW theory [93]. Indeed, we do observe a broad continuum above 5 meV as shown in Figure 5.2 (c), similar to the spinon continuum feature observed in the prototypical quasi-1D antiferromagnet KCuF3 [94, 98]. This again affirms quasi-1D nature of Cu^{2+} spins of $Cu_2(OH)_3Br$.

The measured magnetic excitations and their comparison within LSW theory raise two important questions. First, what is the underlying mechanism that leads to ferromagnetic and antiferromagnetic alternating chains in this system? Second, how do the two different types of magnetic quasiparticles interact with each other?

In order to shed light on the magnetic interactions and the resultant unique spin structure of $Cu_2(OH)_3Br$, we performed first-principles density functional theory (DFT) based calculations. The total energy calculated with different long-range ordered magnetic states is listed in Fig. S4 [22], with the lowest energy spin configuration agreeing with the experimental observation. Using only an isotropic Heisenberg model with nearest neighbor intra- and interchain couplings, the intra-chain (J1 and J2) and the interchain chain (J3 and J4) couplings, illustrated in Figure 5.1 (d), were calculated. Their values are listed in Fig. S5 [22]. One can see that the intra-chain interactions indeed dominate, with J1 being ferro-

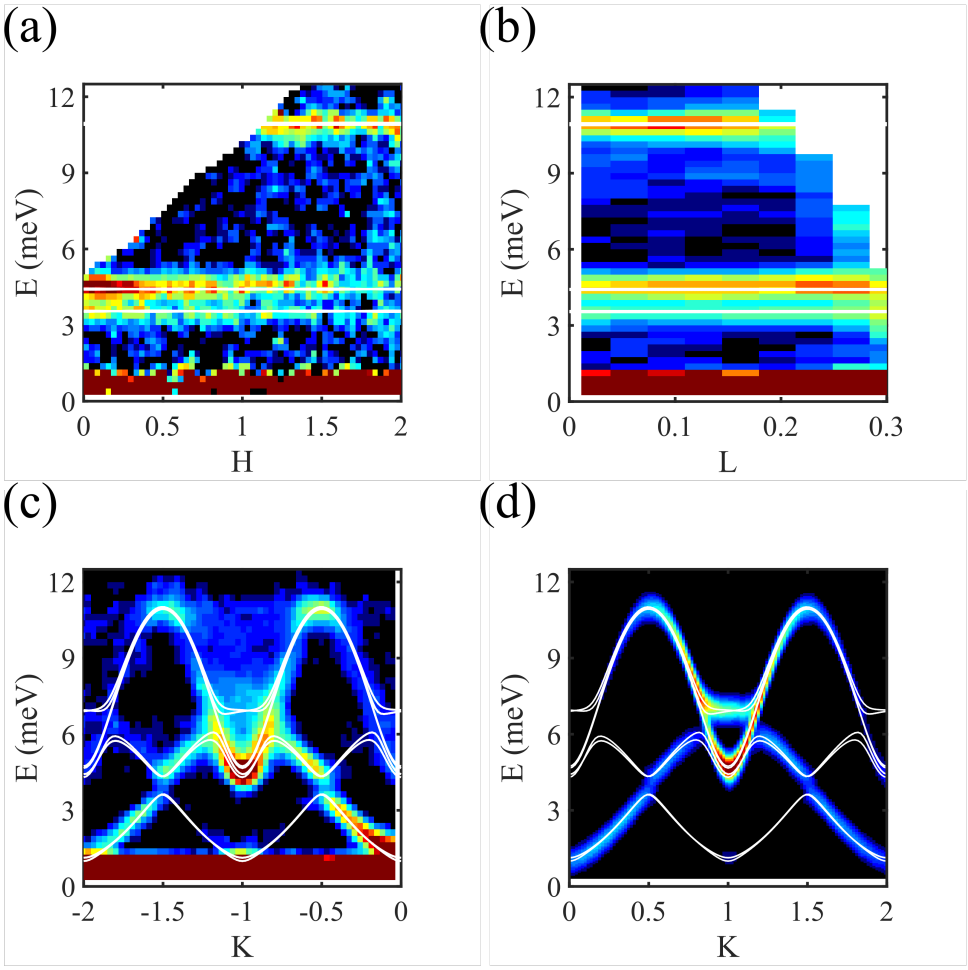

Figure 5.2: Magnetic excitation spectra and the comparison to LSW calculations. (a) The momentum- and energy-resolved neutron scattering intensity map I(E, H) (K = -0.5 and with all measured L values integrated). (b) Intensity map I(E, L) (K = -0.5 and with all measured H values integrated). These two intensity maps show nearly dispersionless magnetic excitations along both H and L directions. (c) Intensity map I(E, K) with both H and L integrated over all measured values to enhance the statistics of the signal. These intensity maps were obtained after using the data measured at T = 100 K as background and subtracting it from the data measured at T = 5 K. (d) The calculated I(E, K) spectra using LSW theory. The white curves in all panels are the calculated dispersions using LSW theory.

magnetic and J2 antiferromagnetic. The weaker interchain couplings J3 and J4 are both antiferromagnetic. The theoretical results are in qualitative agreement with the exchange parameters obtained from LSW fitting. Note that spins of neighboring Cu1 and Cu2 with antiferromagnetic J4 are not energetically favorable, while neighboring spins with antifer-

romagnetic J3 are energetically favorable. The non-zero magnetic interaction J4 leads to frustration, which facilitates the decoupling of Cu1 and Cu2 chains.

To understand the nature of these exchange interactions, in Figure 5.3 (a) we present the ground state spin density profile. The t2g orbitals of Cu^{2+} ions are completely filled while there is a single hole in the eg manifold, which splits due to local crystal field. The spin density shows the half-filled eg orbital, which has (x2-y2)-like character in a local coordinate axis system. Interestingly, all the Cu eg orbital lobes extend towards the oxygen p orbitals but not towards the Br ions. This can be understood by the weaker crystal field associated with Br ions, which have -1 charge as opposed to -2 for the oxygen ions. The resulting crystal field pushes the Cu eg orbital with electron clouds extending towards oxygen ions to higher energies, a characteristic of the hole occupying this orbital and spin density associated with it. The crystal field, combined with the geometry and local coordinate of these two Cu sites, leads to antiferro-orbital orientational order for Cu1 chains and ferro-orbital orientational order for Cu2 chains. Such an unusual orientational ordering of the active magnetic orbital, which can be considered as an improper orbital order imposed by the strongly asymmetric crystal field of the anions, gives rise to anion-mediated exchange interactions that are dominated by Cu-O-Cu exchange pathways, considering that only O orbitals e-bond with the half-filled Cu eg orbitals. This is supported by nearly zero spin density on the Br ions as illustrated in Figure 5.3 (a), which indicates that Br does not hybridize with the spin-polarized Cu orbitals, and hence does not contribute to superexchange. The projected density of states (DOS) of Br, O and the hole (i.e. the unoccupied states) of Cu^{2+} ions are shown in Figure 5.3 (b). Consequently, antiferro-orbital order along Cu1 chains leads to ferromagnetic spin coupling ($J1 < 0$) whereas ferro-orbital order leads to antiferromagnetic spin coupling along the Cu2 chains ($J2 > 0$) [113].

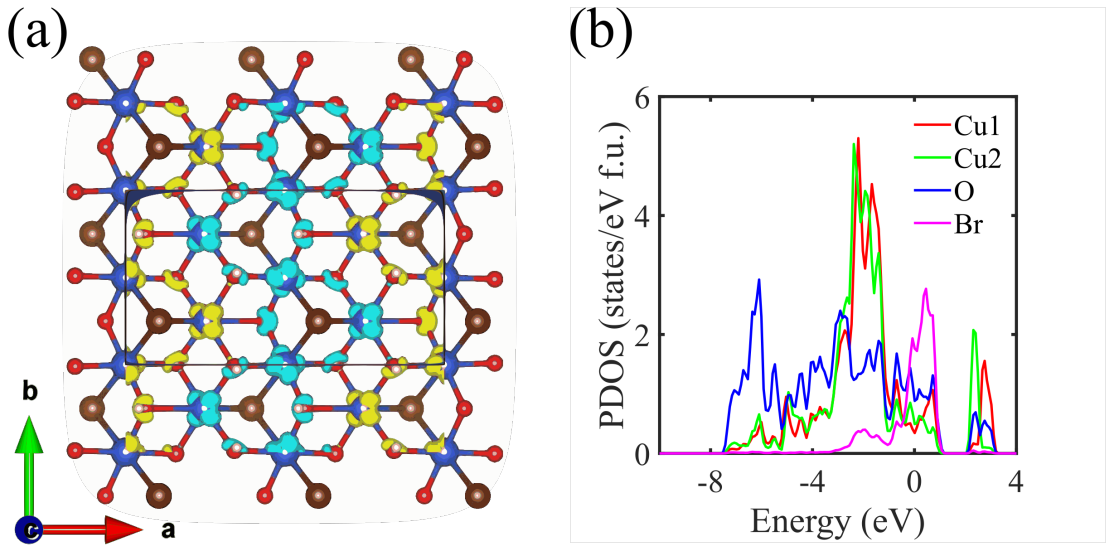

Figure 5.3: Electronic structure calculated via first principles DFT. (a) The ground state spin density of the half-filled eg orbital of Cu^{2+} ions and p orbitals of O and Br atoms. Yellow color denotes spin up and cyan color denotes spin down. Cu1 ions with ferromagnetic spin alignment show antiferro-orbital order while Cu2 ions with antiferromagnetic spin alignment show ferro-orbital order. (b) The projected density of states (PDOS) of Cu1, Cu2, Br, and O ions.

5.3 Magnon-spinon interactions

Next, we discuss magnon-spinon interaction via the weak interchain couplings (J3, J4) between neighboring AFM/FM chains. In the absence of interchain couplings, the system would host deconfined spinons propagating in the AFM chain and well-defined magnons propagating in the FM chain. With gradual increase of interchain couplings, the quasi-1D nature of the system is progressively destroyed and magnetic long-range order develops. It is known that in quasi-1D antiferromagnets composed of identical spin chains, such as KCuF3 [95], there is an energy threshold which separates spinons and magnons. Above this threshold, spinons are deconfined; below this threshold, the spinon continuum turns into classical magnons because of the finite interchain couplings and resulting in long-range order [114, 99]. Thus, in these systems, magnetic excitations are carried either by unbound spinons or clas-

sical magnons in different energy regimes, and they do not interact. In contrast, due to the coexistence of both ferromagnetic and antiferromagnetic chains in $Cu_2(OH)_3Br$, the corresponding magnon and spinon excitations can coexist in the same energy range and interact with each other through the finite interchain couplings.

To better understand the effects of interchain couplings, we have used the Algorithms for Lattice Fermions (ALF) implementation [115] of the finite temperature auxiliary field quantum Monte Carlo to carry out numerical simulations of the dynamical spin structure factor of a system consisting of ferromagnetic and antiferromagnetic spin-1/2 chains [22, 116, 117]. While this algorithm is formulated for fermionic systems, it can also be used to simulate non-frustrated spin systems [117]. For simplicity, we only consider intra-chain couplings (J1 = -1.6 meV, J2 = 5.3 meV) and antiferromagnetic interchain coupling J3 while keeping J4 = 0 (non-zero J4 would introduce magnetic frustration and a negative sign problem).

Figure 5.4 presents the simulated spectra without taking into account the magnetic form factor of Cu^{2+}. There are several important features to point out. First, both well-defined magnon dispersion and spinon continuum, which are associated with ferromagnetic chains and antiferromagnetic chains respectively, are clearly seen, consistent with the experimental observation shown in Figure 5.2 (c). Second, by introducing non-zero J3, the magnetic excitations associated with antiferromagnetic chains are pushed up to higher energy and a gap opens which increases with J3. This gap opening is the result of molecular field arising from the neighboring ferromagnetic chains. Third, compared to the decoupled spin chains, non-zero J3 introduces asymmetric spectral intensity centered about K = 1, as shown by the constant energy cut (at E = [7.7 9.7] meV) presented in Figure 5.4 (d), which suggests that the interchain coupling induces redistribution of spectral weight.

To obtain further insights on the effects of interchain couplings and the resultant magnon-

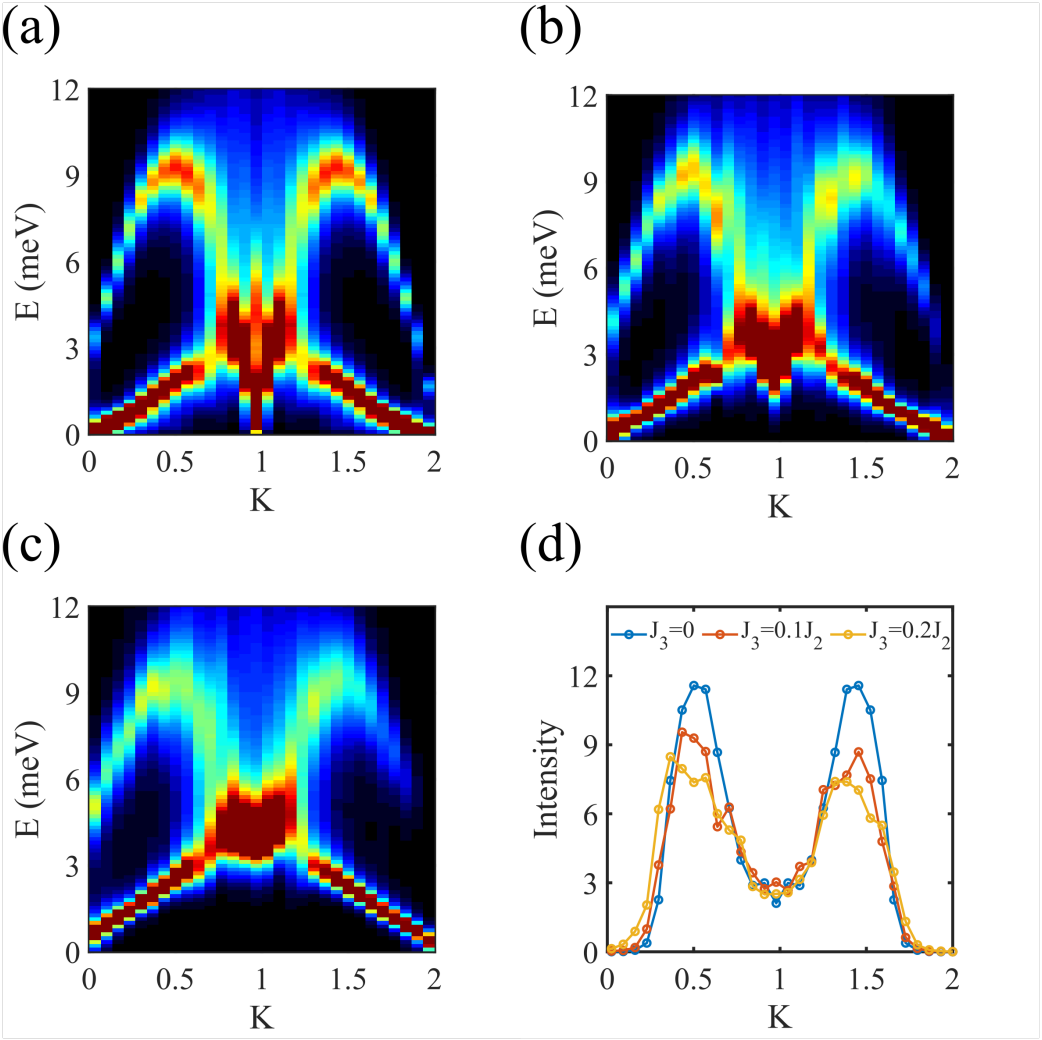

Figure 5.4: Magnetic excitation spectra via quantum Monte Carlo simulations. Simulated magnetic excitation spectra (with H = 1) of a system consisting of alternating ferromagnetic and antiferromagnetic quantum spin chains with the interchain coupling J3 = 0 (a), J3 = 0.1J2 (b), and J3 = 0.2J2 (c). (d) Constant energy cuts at E = [8.7 9.7] meV showing the asymmetric spectral intensity about K = 1 induced by non-zero J3. Note that Bose factor but not magnetic form factor of Cu^{2+} ions has been taken into account in the simulation.

spinon interactions, we perform Random Phase Approximation (RPA) calculations and compare the results with the INS excitation spectra. For this purpose, we adopt and generalize the RPA approach for coupled antiferromagnetic chains [118]. In the presence of interchain interaction, we obtain generalized susceptibilities $\chi^{F,AF}_{RPA}\left(\vec{k},\omega\right)$ for the two types of chains.

$$\chi^{F,AF}_{RPA}\Big(\vec{k},\omega\Big) = \frac{\Big[1 - J_{\perp}(\vec{k}) \cdot \chi^{AF,F}_{1D}(\vec{k}_{\parallel},\omega)\Big] \cdot \chi^{F,AF}_{1D}(\vec{k}_{\parallel},\omega)}{1 - \Big[J_{\perp}(\vec{k})\Big]^2 \cdot \chi^{AF}_{1D}(\vec{k}_{\parallel},\omega) \cdot \chi^{F}_{1D}(\vec{k}_{\parallel},\omega)} \tag{5.1}$$

$$J_{\perp}(\vec{k}) = 4(J_3 + J_4)\cos\Big(\frac{k_{\perp}a}{2}\Big)\sin\Big(\frac{k_{\parallel}b}{4}\Big) \tag{5.2}$$

where $\chi^{F,AF}_{1D}(\vec{k}_{\parallel},\omega)$ are the susceptibilities of non-interacting chains and $J_{\perp}(\vec{k})$ is the Fourier transforms of the interchain couplings. Here $k_{\parallel}$ is the component of the wave vector $\vec{k}$ along the chain direction (b-axis), and $k_{\perp}$ is perpendicular to the chain direction (a-axis). We use a Lorentzian function for $\chi^{F}_{1D}(\vec{k}_{\parallel},\omega)$ and the Muller Ansatz [93] expression for $\chi^{AF}_{1D}(\vec{k}_{\parallel},\omega)$. Detailed description of the generalized RPA approach is documented in the Supplemental Materials [22].

Figure 5.5 (a, b) present the measured excitations with H integrated over [0.85 1.15] and the corresponding RPA results, respectively. In addition to the two-spinon continuum that is clearly observed in RPA calculations [Figure 5.5 (b)], which is consistent with the experimental data shown in Figure 5.5 (a), one can see a clear modification of the spectral intensity caused by the interchain couplings. For instance, a constant energy cut at E = 10.75 meV is plotted in Figure 5.5 (c), together with the RPA calculations with (red) and without (black) interchain couplings. One can see that RPA with the inclusion of interchain couplings captures the redistribution of the spectral weight with the intensity at K = -0.5 larger than that at K = -1.5. This difference cannot be accounted for by magnetic form factor. Note that $J_{\perp}(\vec{k})$ is negative when K is in the range of [-1 0] and positive when K is in the range [-2 -1]. This difference in the sign leads to the asymmetry in the spectral weight about K = -1, which is consistent with the QMC simulation results shown in Figure 5.4 (b-d). If we reduce the constant energy cut to E = 7.75 meV [Figure 5.5 (d)] and focus on the

two peaks closest to K = -1, again the RPA spectrum with interchain couplings introduces asymmetry. The agreement near K = -1.25 is very good but not so good for K = -0.75. Further comparison between experimental data and RPA calculation results are discussed in the Supplemental Materials [22].

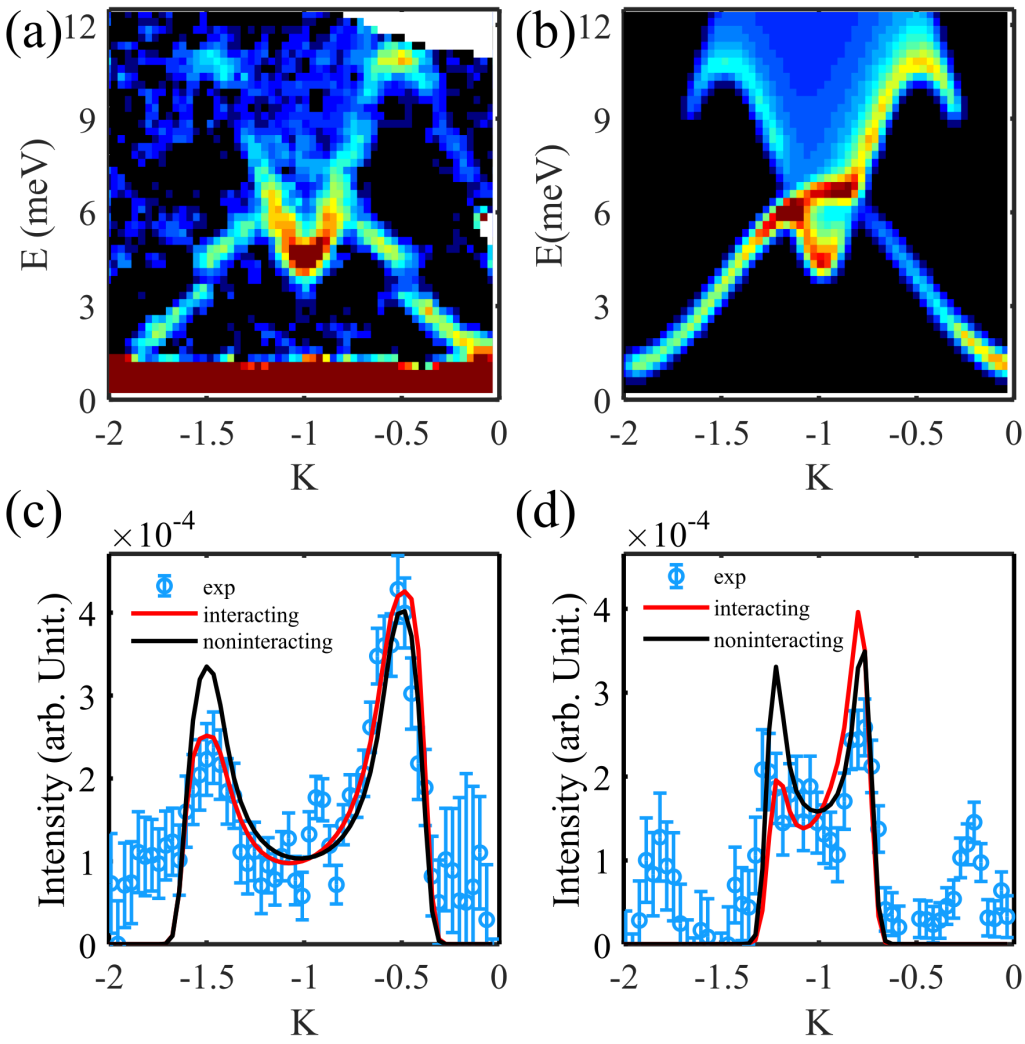

Figure 5.5: Magnetic excitation spectra and the comparison with RPA calculations. (a) I(E, K) intensity map obtained after background subtraction with H integrated over [0.85 1.1] and L integrated over all measured values. (b) The RPA calculation of I(E, K) spectra for comparison. Constant energy cuts at E = 10.75 meV (c) and at E = 7.75 meV (d) and their comparison with RPA calculations.

5.4 Summary and future perspectives

In summary, we have discovered that magnons and spinons coexist in $Cu_2(OH)_3Br$, which uniquely consists of quasi-1D ferromagnetic and antiferromagnetic quantum spin chains. Magnons and spinons interact with each other via weak but finite interchain couplings, which opens the gap of the spinon continuum and gives rise to a redistribution of the spectral weight.

Spin currents transported through one dimensional spin chain system is a topic worth of further investigations. For conventional ferromagnets, spin currents are carried by magnons. A well-known example can be found in yttrium-iron garnet $Y_3Fe_5O_{12}$, which has been widely used as a spin current conductor. For antiferromagnt spin chains, spinons can also carry spin currents [119]. In $Cu_2(OH)_3Br$, we have shown that both ferromagnetic and antiferromagnetic spin chains coexists and interact with each other. Through the finite inter-chain coupling, the spectral weight of these two quasiparticles has redistributed, leading new spin dynamics. How will such new spin dynamic affect the spin transport in this unique quantum magnet remains an open topic for discussions.

A second interesting point is the theoretical implications brought about by our study. While theories for ferromagnetic and antiferromagnetic spin chains have been developed separately, the coexistence and coupling between the two has not been studied extensively. This is partly because that it is hard to imagine a physical system realizing such a model. Yet, nature has its surprise for installed for us. Such a peculiar model can be found in a naturally occurring mineral, the botallackite [$Cu_2(OH)_3Br$]. This study highlights a new toy model and research paradigm to study the interaction between two different types of magnetic quasiparticles.

Chapter 6

Manual for TTO_v2

TTO_v2.lvproj is a Labview project located on the PPMS computer at

`C:\Users\PPMS\Desktop\Thermal Transport\2182_test\TTO_v2`.

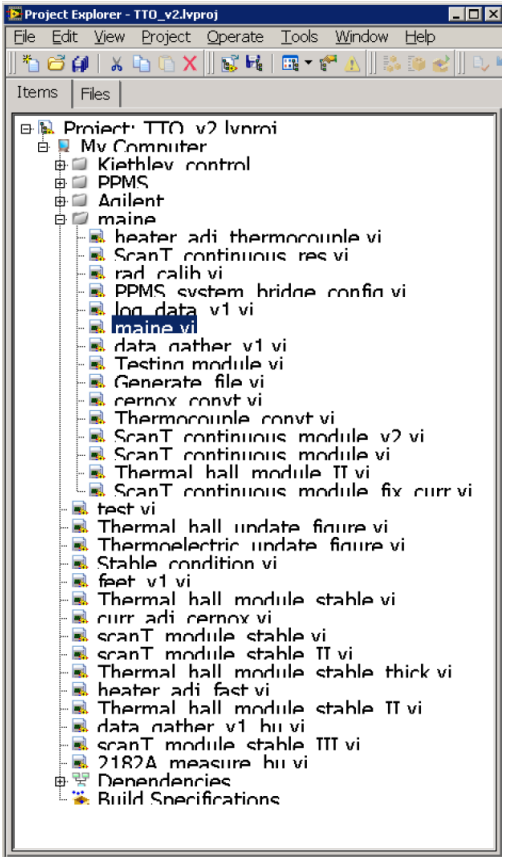

Figure 6.1: A screen shot of TTO_v2.lvproj is shown above. Although there are many .vi files in the project, a typical user would only need to access the maine.vi (highlighted) file.

6.1 The hierarchy of TTO_v2.lvproj and the maine.vi

The hierarchy structure of TTO_v2.lvproj is shown in the following figure. There are six options typically used for measurement purposes as highlighted by the orange boxes. They can all be called by the maine.vi file. For a typical user, one would need to write a *sequence* file, supply the path to maine.vi and click 'run'.

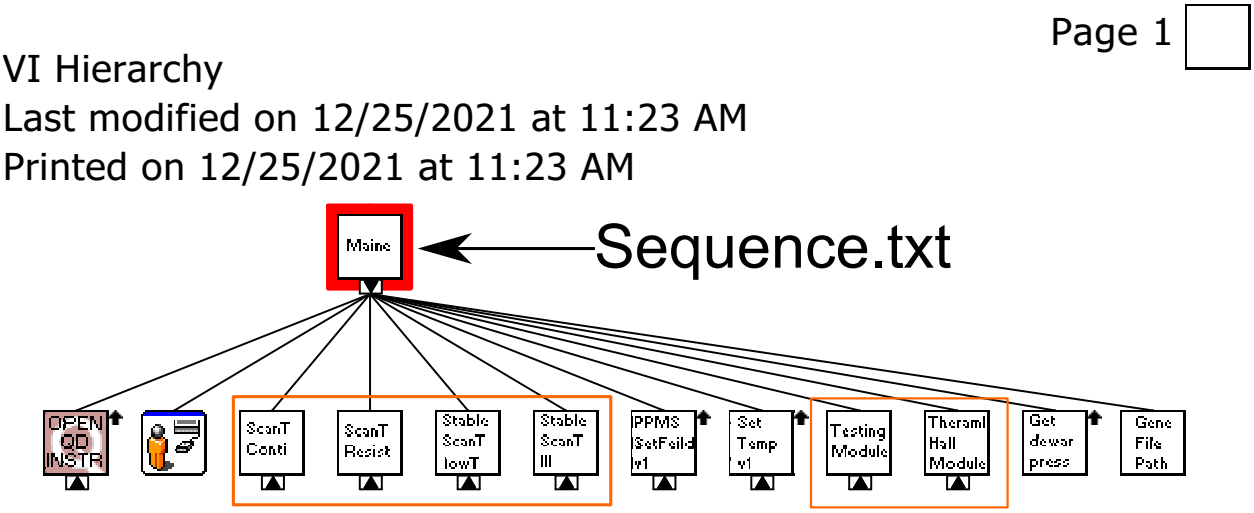

Figure 6.2: The hierarchy of TTO_v2.lvproj

maine.vi - The following figure shows a screen shot of the maine.vi file. There are three interactive levers one can click. Clicking lever one will load the sequence file from the path indicated by the text area under 'Sequence'.

`C:\Users\PPMS\GDfuf\proj\TTO_data\VI3\exp02102021\seqt`.

The loaded sequence will be displayed in the text area on the bottom left (red box). Clicking lever two will run the loaded sequence. The maine.vi will not be responsive before a sequence is finished. You will be able to stop the program by clicking the red stop button below the menu bar at the top. Clicking lever three will run the *testing module.vi*. Clicking View (menu bar) → VI Hierarchy will prompt a window with the content shown in Figure 6.2.

Double clicking any icons in the prompt window will open the front panel of the module.

Figure 6.3: The front panel of maine.vi. For the most part, a typical user should only need to access this panel.

6.2 Six frequently used options

testing module.vi - This module is represented by the icon *Testing module* in Figure 6.2. This module should be used at the beginning of each measurement to examine if all contacts are made properly and all meters are connecting correctly.

An example is shown by the following figure. The left window in the first row shows the

PPMS system temperature and temperature one/two/three as green dots and red/green/blue lines, respectively. The selection box with *Cernox/Thermocouple* determines which sensor *testing module.vi* will use. Selecting *Cernox*, the reading from the three resistance bridge channels of PPMS will be used. Selecting *Thermocouple*, the readings from the three voltage meters will be used. The relation is tabulated Table 6.1.

T	Cernox	Thermocouple
T1	bridge 1	Vl
T2	bridge 2	Vr
T3	bridge 3	Vu

Table 6.1: The mapping relation between the temperature reading, cernox bridge change and thermocouple voltage.

The middle window in the first row shows the longitudinal (ΔT_{xx}) and transverse (ΔT_{yx}) temperature difference. These two quantities needs to be defined before each run. The left and right window in the second row and the right window in the first row shows the readings from the left, right and upper voltage meters (you will know what they are when you go into the lab).

Clicking the lever under *Clear* will clear all data points. Clicking the lever next to I(mA) will turn on/off the current source, there by generating a pulse. If one of the contacts was loose, there will not be much response (for example, no temperature change) after turning on the current, then it will be necessary to take the sample out and remake the contacts. The pulse in the screen shot is produced by the following actions: run the testing module $\rightarrow$ click the lever next to I(mA) $\rightarrow$ wait $\rightarrow$ click the lever next to I(mA) again $\rightarrow$ wait $\rightarrow$ click the stop button on the lower right. (Note that Vu is not connected in this example)

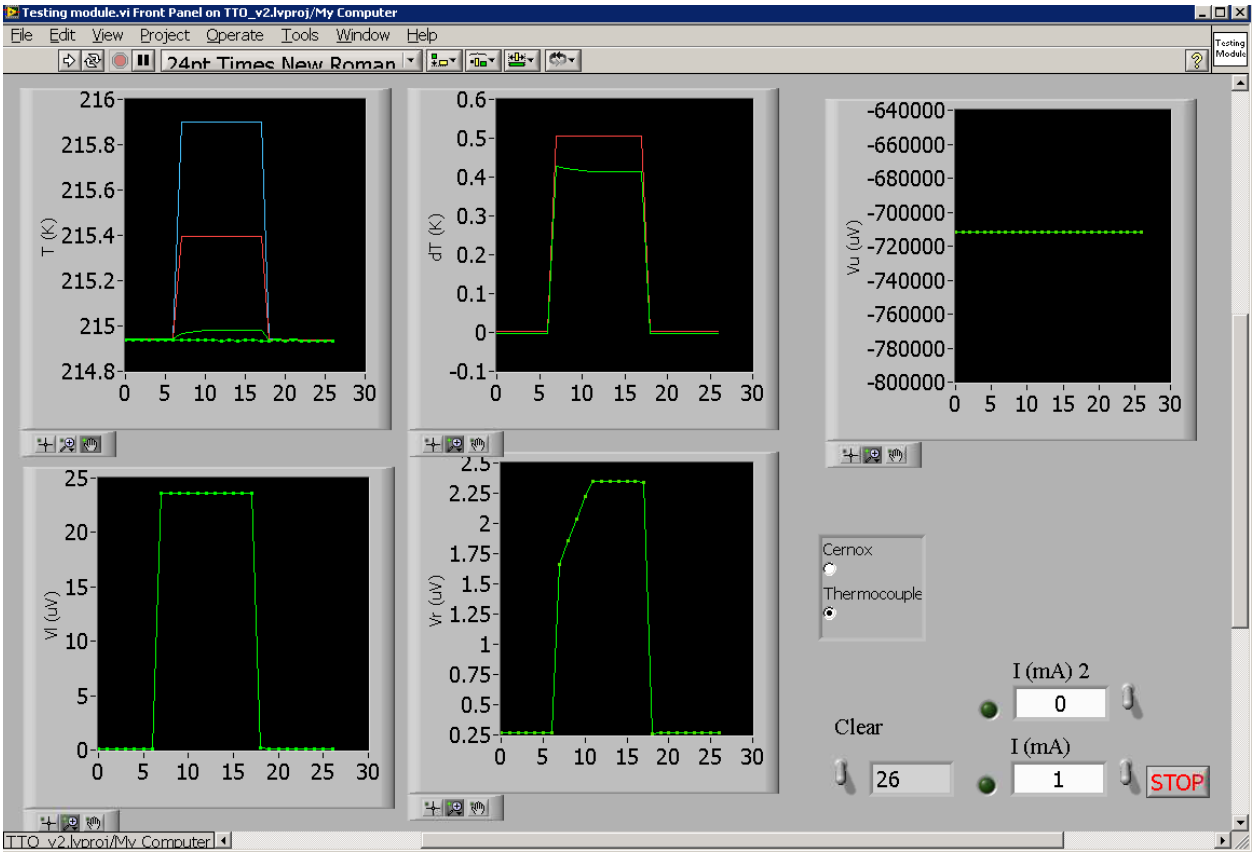

Figure 6.4: The front panel of *testing module.vi*.

ScanT_continuous_module_v2.vi - This module is represented by the icon *ScanT Conti* in Figure 6.2. This module is used for measuring the thermal conductivity and Seebeck/Nernst coefficients as functions of temperature. The module is invoked by writing the following sentence in your sequence file.

scanT, T1, T2, Trate, not_test_cur==0, curr, dT_target,raise_per_K(in mk), mode (0-SN, 1-Pi)
Example: scanT,10,305,3,0,0.5,0,0,0

Table 6.2: The meaning and usage example for *ScanT_continuous_module_v2.vi*.

ScanT is the keyword telling *maine.vi* to call *ScanT_continuous_module_v2.vi*. T1 is the

initial temperature, T2 is the final temperature and Trate is the temperature ramping rate. For the first data point measured at T1, the program assumes the user does not know what is the appropriate current to use. The program will try to find the appropriate current if not_test_cur is set to any value other than zero. The program will use the curr supplied by the user as the initial current for this finding procedure. The current for all following measurements are handled by the program. The dT_target,raise_per_K(in mk) are obsolete quantities which can be set to any value (I usually put zeros there since they are harmless). The mode should always be supplied with a zero. The example shown here translate to the following: A temperature scan from 10 K to 305 K at a ramping rate of 3 K/minute will be performed (10,305,3). An initial current of 0.5 milliampere will be used and no initial testing procedure will take place (0,0.5). We measure the Seebeck/Nernst coefficients (mode==0).

ScanT_continuous_res_v2.vi - This module is represented by the icon *ScanT Resist* in Figure 6.2. This module is used for measuring the resistivity as a function of temperature. This module is invoked by writing the following sentence in your sequence file. This module is very similar to the previous module. The not_test_cur field should always be supplied with a zero.

scanTrc, T1, T2, Trate, not_test_cur==0, curr, dT_target,raise_per_K(in mk), mode (0-SN, 1-Pi)
scanTrc,10,305,3,0,5,0,0,0

Table 6.3: The meaning and usage example for *ScanT_continuous_res_v2.vi*.

The example shown here translate to the following: A temperature scan from 10 K to 305 K at a ramping rate of 3 K/minute will be performed (10,305,3). A current of 5 milliampere

will be used and no initial testing procedure will take place (0,5). We measure the resistivity (mode==0).

ScanT_module_stable_III[1] - This module is represented by the icon *Stable ScanT III* in Figure 6.2. This module is used for measuring the thermal conductivity and Seebeck/Nernst coefficients as functions of temperature. This module is invoked by writing the following sentence in your sequence file.

scanTs, T1, T2, Tstep, test_cur==1, curr, dT_target, mode (0-constant current, 1-polynomial)
scanTs,30,120,3,1,0.2,0,0

Table 6.4: The meaning and usage example for *ScanT_module_stable_III*.

ScanTs is the keyword telling *maine.vi* to call *ScanT_module_stable_III*. In 'stable' mode, the program will set the temperature and wait for it to stabilize before each data point was taken. T1 is the initial temperature, T2 is the final temperature and Tstep is the temperature difference between each data point. The current testing procedure will take place if test_cur is set to one (and not take place otherwise). The dT_target is an obsolete quantity which can be set to any value (I usually put zeros there since they are harmless). The mode should always be supplied with a zero, the '1-polynomial' option is obsolete. The example shown here translate to the following: A series of measurements at [30 K, 33 K, 36 K ... 120 K] will be performed (30,120,3). An initial current of 0.2 milliampere will be used and initial testing procedure will take place (1,0.2). We use the same current for all measurement points (mode==0).

ScanT_module_stable_II - This module is represented by the icon *Stable ScanT lowT* in

[1]It will be necessary for the user to select the temperature sensor from the front panel of this .vi file.

Figure 6.2. This module performs the same functions as the previous module, except that it is intended for measurements at lower temperatures (2 K to 50 K). This module is invoked by writing the following sentence in your sequence file.

scanTsl, T1, T2, Tstep, test_cur==1, curr, dT_target
scanTsl,2,40,2,1,0.2,0,0

Table 6.5: The meaning and usage example for *ScanT_module_stable_II*.

Thermal_hall_module_II[2] - This module is represented by the icon *Thermal Hall Module* in Figure 6.2. This module performs a magnetic field scan at fixed temperatures. This module is invoked by writing the following sentence in your sequence file.

th, H1, H2, Hrate, loop=1, curr, dT_target, test_curr==0, mode (0-SN, 1-Pi)
th,3,-3,100,1,0.5,0,0,0

Table 6.6: The meaning and usage example for *Thermal_hall_module_II*.

th is the keyword telling *maine.vi* to call *ScanT_module_stable_III*. H1 is the initial field, H2 is the final field and Hrate is the magnetic field ramping rate in units of Oe/s. The program will take another measurement from the final field back to the initial field if loop is set to one. The curr is the initial current (mA) the program will use. The current testing procedure will take place if test_cur is set to zero (and not take place otherwise). The dT_target is an obsolete quantity which can be set to any value. The mode should always be supplied with a zero, the '1-Pi' option is obsolete. The example shown here translate to the following: A magnetic field scan 3 T $\rightarrow$ -3 T $\rightarrow$ 3T will be performed. An initial current

[2]It will be necessary for the user to select the temperature sensor from the front panel of this .vi file.

of 0.5 milliampere will be used and initial testing procedure will take place.

6.3 Performing a measurement

Performing a measurement includes the following steps: making contacts on sample → connecting meters → selecting temperature sensors → defining measured quantities → writing a sequence → run sequence.

Selecting temperature sensors - For a thermal/thermoelectric measurement, we sometimes need to test for the 'appropriate' heating power, which does not heat up the sample substantially. The program can handle this task, but we need to tell the program what readings to use by configuring the temperature sensor. We need to do this step **only** when we are using either of the two options (Section 6.2): the *ScanT_module_stable_III* and the *Thermal_hall_module_II*. To do this, open the project hierarchy → double click the module (For example, *Stable ScanT III*) → select 'Thermocouple/Cernox' → right click on the edge of the highlighted selection box → Data Operations → Make current value Default.

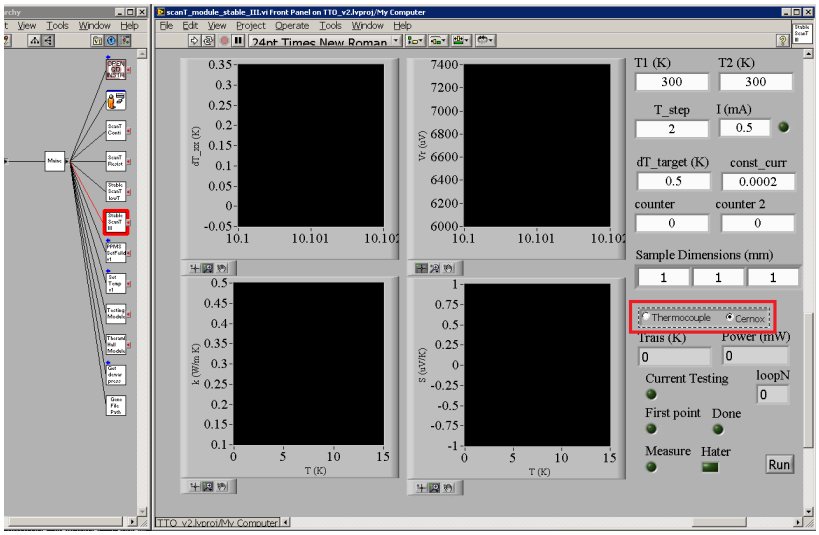

Figure 6.5: The program hierarchy and the front panel of *ScanT_module_stable_III*

Defining measured quantities - There are six quantities which 'need' to be defined:$\Delta T_{xx,t}$, $\Delta T_{yx,t}$, $\Delta T_{xx,c}$, $\Delta T_{yx,c}$, T_{heatup}, T_{heatup_c}. When making contacts on the sample, it may not be easy to make them exactly as the layout in section 2.1.1. In this case, we will be allowed to make the contacts in the most convenient way possible, and define the measured quantities such that the measurement will make sense. To do this, double click log_data_v1.vi (right above maine.vi, see Section 6) → click 'E' while holding down Ctrl on keyboard → click any of the boxes will prompt a selection menu, allowing the user to change definitions (example shown here is consistent with the layout in section 2.1.1 → click 'S' while holding down Ctrl on keyboard (to save). T1/T2/T3 means the temperature readings from cernox sensor-1/2/3. Th1/Th2/Th3 means the temperature readings from thermocouples-1/2/3. T_{heatup} and T_{heatup_c} means the temperature difference between the hot-end (depend on how the contacts are made) and system read from thermocouple/cernox, respectively.

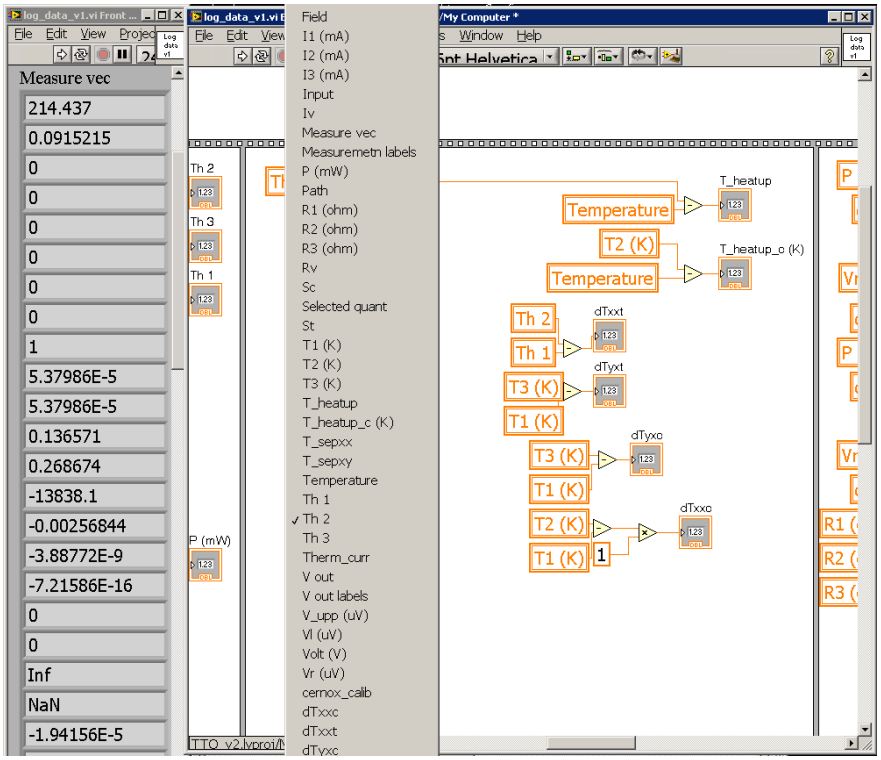

Figure 6.6: The front panel of *log_data_v1.vi*

Writing a sequence - A Sequence is a text file made up of a series of commands. The following table tabulates all commands. Each command should be typed as a newline in the sequence file. The 'waitd' command is used to conserve helium. Ramping the magnetic field will cause the dewar pressure to increase substantially. Between measurements, we can wait for the compressor to catch-up and lowers the dewar pressure before proceeding using this command. Do so will allow a helium tank to last for months. I usually set the threshold value to 4.3 kpsi.

' ': do nothing.
'*nf*': create a new file to record data from following measurements.
'*wait,XXX*': wait for XXX seconds.
'*waitd,XXX*': wait for the dewar pressure to settle below XXX kpsi.
'*set,1,Tset,rate,wait*': to set the temperature (indicated by '1') to 'Tset' (K), at a rate of 'rate' K/minute. Wait 'wait' seconds before proceeding to the next line.
'*set,2,Hset,rate'*: to set the magnetic field (indicated by '2') to 'Hset' (T), at a rate of 'rate' Oe/second.
Commands to invoke the six options described in Section 6.2.

Table 6.7: Collection of currently available commands to put in a sequence file.

BIBLIOGRAPHY

BIBLIOGRAPHY

[1] Bernhard Keimer, Steven A Kivelson, Michael R Norman, Shinichi Uchida, and J Zaanen. From quantum matter to high-temperature superconductivity in copper oxides. *Nature*, 518(7538):179–186, 2015.

[2] Y. Kurosaki, Y. Shimizu, K. Miyagawa, K. Kanoda, and G. Saito. Mott Transition from a Spin Liquid to a Fermi Liquid in the Spin-Frustrated Organic Conductor κ-$(ET)_2Cu_2(CN)_3$. *Phys. Rev. Lett.*, 95:177001, Oct 2005.

[3] Alexei Kitaev. Anyons in an exactly solved model and beyond. *Annals of Physics*, 321(1):2–111, 2006. January Special Issue.

[4] Su-Yang Xu, Ilya Belopolski, Nasser Alidoust, Madhab Neupane, Guang Bian, Chenglong Zhang, Raman Sankar, Guoqing Chang, Zhujun Yuan, Chi-Cheng Lee, Shin-Ming Huang, Hao Zheng, Jie Ma, Daniel S. Sanchez, BaoKai Wang, Arun Bansil, Fangcheng Chou, Pavel P. Shibayev, Hsin Lin, Shuang Jia, and M. Zahid Hasan. Discovery of a Weyl fermion semimetal and topological Fermi arcs. *Science*, 349(6248):613–617, 2015.

[5] Koichi Momma and Fujio Izumi. *VESTA3* for three-dimensional visualization of crystal, volumetric and morphology data. *Journal of Applied Crystallography*, 44(6):1272–1276, Dec 2011.

[6] Heda Zhang, Chunqiang Xu, Caitlin Carnahan, Milos Sretenovic, Nishchay Suri, Di Xiao, and Xianglin Ke. Anomalous Thermal Hall Effect in an Insulating van der Waals Magnet. *Phys. Rev. Lett.*, 127:247202, Dec 2021.

[7] M. Z. Hasan and C. L. Kane. Colloquium: Topological insulators. *Rev. Mod. Phys.*, 82:3045–3067, Nov 2010.

[8] A. Alexandradinata, N. P. Armitage, Andrey Baydin, Wenli Bi, Yue Cao, Hitesh J. Changlani, Eli Chertkov, Eduardo H. da Silva Neto, Luca Delacretaz, Ismail El Baggari, G. M. Ferguson, William J. Gannon, Sayed Ali Akbar Ghorashi, Berit H. Goodge, Olga Goulko, G. Grissonnanche, Alannah Hallas, Ian M. Hayes, Yu He, Edwin W. Huang, Anshul Kogar, Divine Kumah, Jong Yeon Lee, A. Legros, Fahad Mahmood, Yulia Maximenko, Nick Pellatz, Hryhoriy Polshyn, Tarapada Sarkar, Allen Scheie, Kyle L. Seyler, Zhenzhong Shi, Brian Skinner, Lucia Steinke, K. Thirunavukkuarasu, Thaís Victa Trevisan, Michael Vogl, Pavel A. Volkov, Yao Wang, Yishu Wang, Di Wei, Kaya Wei, Shuolong Yang, Xian Zhang, Ya-Hui Zhang, Liuyan Zhao, and Alfred Zong. The Future of the Correlated Electron Problem, 2020.

[9] J George Bednorz and K Alex Müller. Possible High T_c Superconductivity in the Ba-La-Cu-O System. *Zeitschrift für Physik B Condensed Matter*, 64(2):189–193, 1986.

[10] N F Mott. The Basis of the Electron Theory of Metals, with Special Reference to the Transition Metals. *Proceedings of the Physical Society. Section A*, 62(7):416–422, jul 1949.

[11] P. W. Anderson, G. Baskaran, Z. Zou, and T. Hsu. Resonating–valence-bond theory of phase transitions and superconductivity in La_2CuO_4-based compounds. *Phys. Rev. Lett.*, 58:2790–2793, Jun 1987.

[12] C. Broholm, R. J. Cava, S. A. Kivelson, D. G. Nocera, M. R. Norman, and T. Senthil. Quantum spin liquids. *Science*, 367(6475):eaay0668, 2020.

[13] Hidenori Takagi, Tomohiro Takayama, George Jackeli, Giniyat Khaliullin, and Stephen E Nagler. Concept and realization of Kitaev quantum spin liquids. *Nature Reviews Physics*, 1(4):264–280, 2019.

[14] Lucile Savary and Leon Balents. Quantum spin liquids: a review. *Reports on Progress in Physics*, 80(1):016502, nov 2016.

[15] M.S. Dresselhaus, G. Dresselhaus, and A. Jorio. *Group Theory: Application to the Physics of Condensed Matter*. Springer Berlin Heidelberg, 2007.

[16] Daniel Arovas. Lecture Notes on Group Theory in Physics (A Work in Progress).

[17] M. Born and V. Fock. Beweis des Adiabatensatzes. *Zeitschrift für Physik*, 51(3):165–180, 1928.

[18] Michael Victor Berry. Quantal phase factors accompanying adiabatic changes. *Proceedings of the Royal Society of London. A. Mathematical and Physical Sciences*, 392(1802):45–57, 1984.

[19] F. D. M. Haldane. Model for a Quantum Hall Effect without Landau Levels: Condensed-Matter Realization of the "Parity Anomaly". *Phys. Rev. Lett.*, 61:2015–2018, Oct 1988.

[20] Heda Zhang, Jahyun Koo, Chunqiang Xu, Milos Sretenovic, Binghai Yan, and Xianglin Ke. Exchange-biased topological transverse thermoelectric effects in a Kagome ferrimagnet. *Nature Communications*, 13(1):1091, 2022.

[21] H. Zhang, C. Q. Xu, and X. Ke. Topological Nernst effect, anomalous Nernst effect, and anomalous thermal Hall effect in the Dirac semimetal Fe_3Sn_2. *Phys. Rev. B*, 103:L201101, May 2021.

[22] H. Zhang, Z. Zhao, D. Gautreau, M. Raczkowski, A. Saha, V. O. Garlea, H. Cao, T. Hong, H. O. Jeschke, Subhendra D. Mahanti, T. Birol, F. F. Assaad, and X. Ke.

Coexistence and Interaction of Spinons and Magnons in an Antiferromagnet with Alternating Antiferromagnetic and Ferromagnetic Quantum Spin Chains. *Phys. Rev. Lett.*, 125:037204, Jul 2020.

[23] H. Zhang, X. Feng, T. Heitmann, A. I. Kolesnikov, M. B. Stone, Y.-M. Lu, and X. Ke. Topological magnon bands in a room-temperature kagome magnet. *Phys. Rev. B*, 101:100405, Mar 2020.

[24] H. Zhang, Y. L. Zhu, Y. Qiu, W. Tian, H. B. Cao, Z. Q. Mao, and X. Ke. Field-induced magnetic phase transitions and the resultant giant anomalous Hall effect in the antiferromagnetic half-Heusler compound DyPtBi. *Phys. Rev. B*, 102:094424, Sep 2020.

[25] Y. Onose, T. Ideue, H. Katsura, Y. Shiomi, N. Nagaosa, and Y. Tokura. Observation of the Magnon Hall Effect. *Science*, 329(5989):297–299, 2010.

[26] Z.-X. Li, Yunshan Cao, and Peng Yan. Topological insulators and semimetals in classical magnetic systems. *Physics Reports*, 915:1–64, 2021. Topological insulators and semimetals in classical magnetic systems.

[27] Lifa Zhang, Jie Ren, Jian-Sheng Wang, and Baowen Li. Topological magnon insulator in insulating ferromagnet. *Phys. Rev. B*, 87:144101, Apr 2013.

[28] R. Chisnell, J. S. Helton, D. E. Freedman, D. K. Singh, R. I. Bewley, D. G. Nocera, and Y. S. Lee. Topological Magnon Bands in a Kagome Lattice Ferromagnet. *Phys. Rev. Lett.*, 115:147201, Sep 2015.

[29] Max Hirschberger, Robin Chisnell, Young S. Lee, and N. P. Ong. Thermal Hall Effect of Spin Excitations in a Kagome Magnet. *Phys. Rev. Lett.*, 115:106603, Sep 2015.

[30] Michael A. McGuire. Crystal and Magnetic Structures in Layered, Transition Metal Dihalides and Trihalides. *Crystals*, 7(5), 2017.

[31] P. Doležal, M. Kratochvílová, V. Holý, P. Čermák, V. Sechovský, M. Dušek, M. Míšek, T. Chakraborty, Y. Noda, Suhan Son, and Je-Geun Park. Crystal structures and phase transitions of the van der Waals ferromagnet VI_3. *Phys. Rev. Materials*, 3:121401, Dec 2019.

[32] Thomas Marchandier, Nicolas Dubouis, Fran çois Fauth, Maxim Avdeev, Alexis Grimaud, Jean-Marie Tarascon, and Gwenaëlle Rousse. Crystallographic and magnetic structures of the VI_3 and $LiVI_3$ van der Waals compounds. *Phys. Rev. B*, 104:014105, Jul 2021.

[33] T. Ideue, T. Kurumaji, S. Ishiwata, and Y. Tokura. Giant thermal Hall effect in multiferroics. *Nature Materials*, 16(8):797–802, 2017.

[34] BingBing Lyu, YiFan Gao, Yujun Zhang, Le Wang, Xiaohua Wu, Yani Chen, Jiasheng Zhang, Gaomin Li, Qiaoling Huang, Naipeng Zhang, Yuanzhen Chen, Jiawei Mei, Hugen Yan, Yue Zhao, Li Huang, and Mingyuan Huang. Probing the Ferromagnetism and Spin Wave Gap in VI3 by Helicity-Resolved Raman Spectroscopy. *Nano Letters*, 20(8):6024–6031, 2020.

[35] Ryo Matsumoto and Shuichi Murakami. Theoretical Prediction of a Rotating Magnon Wave Packet in Ferromagnets. *Phys. Rev. Lett.*, 106:197202, May 2011.

[36] Hyunyong Lee, Jung Hoon Han, and Patrick A. Lee. Thermal Hall effect of spins in a paramagnet. *Phys. Rev. B*, 91:125413, Mar 2015.

[37] X. S. Wang, H. W. Zhang, and X. R. Wang. Topological Magnonics: A Paradigm for Spin-Wave Manipulation and Device Design. *Phys. Rev. Applied*, 9:024029, Feb 2018.

[38] H. Lane, E. Pachoud, J. A. Rodriguez-Rivera, M. Songvilay, G. Xu, P. M. Gehring, J. P. Attfield, R. A. Ewings, and C. Stock. Two-dimensional ferromagnetic spin-orbital excitations in honeycomb VI_3. *Phys. Rev. B*, 104:L020411, Jul 2021.

[39] Y. Aharonov and D. Bohm. Significance of Electromagnetic Potentials in the Quantum Theory. *Phys. Rev.*, 115:485–491, Aug 1959.

[40] Naoto Nagaosa, Jairo Sinova, Shigeki Onoda, A. H. MacDonald, and N. P. Ong. Anomalous Hall effect. *Rev. Mod. Phys.*, 82:1539–1592, May 2010.

[41] Robert Karplus and J. M. Luttinger. Hall Effect in Ferromagnetics. *Phys. Rev.*, 95:1154–1160, Sep 1954.

[42] T. Jungwirth, Qian Niu, and A. H. MacDonald. Anomalous Hall Effect in Ferromagnetic Semiconductors. *Phys. Rev. Lett.*, 88:207208, May 2002.

[43] Di Xiao, Yugui Yao, Zhong Fang, and Qian Niu. Berry-Phase Effect in Anomalous Thermoelectric Transport. *Phys. Rev. Lett.*, 97:026603, Jul 2006.

[44] Muhammad Ikhlas, Takahiro Tomita, Takashi Koretsune, Michi-To Suzuki, Daisuke Nishio-Hamane, Ryotaro Arita, Yoshichika Otani, and Satoru Nakatsuji. Large anomalous Nernst effect at room temperature in a chiral antiferromagnet. *Nature Physics*, 13(11):1085–1090, 2017.

[45] Masaki Mizuguchi and Satoru Nakatsuji. Energy-harvesting materials based on the anomalous Nernst effect. *Science and Technology of Advanced Materials*, 20(1):262–275, 2019. PMID: 30956732.

[46] Yuya Sakuraba, Kota Hasegawa, Masaki Mizuguchi, Takahide Kubota, Shigemi Mizukami, Terunobu Miyazaki, and Koki Takanashi. Anomalous Nernst Effect in

$L1_0-FePt/MnGa$ Thermopiles for New Thermoelectric Applications. *Applied Physics Express*, 6(3):033003, mar 2013.

[47] JunSen Xiang, SiLe Hu, Meng Lyu, WenLiang Zhu, ChaoYang Ma, ZiYu Chen, Frank Steglich, GenFu Chen, and PeiJie Sun. Large transverse thermoelectric figure of merit in a topological Dirac semimetal. *Science China Physics, Mechanics & Astronomy*, 63(3):1–7, 2020.

[48] B.Chafik El Idrissi, G. Venturini, B. Malaman, and D. Fruchart. Magnetic structures of TbMn6Sn6 and HoMn6Sn6 compounds from neutron diffraction study. *Journal of the Less Common Metals*, 175(1):143–154, 1991.

[49] C. Mielke III, W. Ma, V. Pomjakushin, O. Zaharko, S. Sturniolo, X. Liu, V. Ukleev, J. S. White, J. X. Yin, S. S. Tsirkin, C. B. Larsen, T. A. Cochran, M. Medarde, V. Poree, D. Das, R. Gupta, C. N. Wang, J. Chang, Z. Q. Wang, R. Khasanov, T. Neupert, A. Amato, L. Liborio, S. Jia, M. Z. Hasan, H. Luetkens, and Z. Guguchia. Intriguing magnetism of the topological kagome magnet $TbMn_6Sn_6$, 2021.

[50] W. H. Meiklejohn and C. P. Bean. New Magnetic Anisotropy. *Phys. Rev.*, 102:1413–1414, Jun 1956.

[51] J Nogués and Ivan K Schuller. Exchange bias. *Journal of Magnetism and Magnetic Materials*, 192(2):203–232, 1999.

[52] Jia-Xin Yin, Wenlong Ma, Tyler A. Cochran, Xitong Xu, Songtian S. Zhang, Hung-Ju Tien, Nana Shumiya, Guangming Cheng, Kun Jiang, Biao Lian, Zhida Song, Guoqing Chang, Ilya Belopolski, Daniel Multer, Maksim Litskevich, Zi-Jia Cheng, Xian P. Yang, Bianca Swidler, Huibin Zhou, Hsin Lin, Titus Neupert, Ziqiang Wang, Nan Yao, Tay-Rong Chang, Shuang Jia, and M. Zahid Hasan. Quantum-limit Chern topological magnetism in TbMn6Sn6. *Nature*, 583(7817):533–536, 2020.

[53] R. Engel-Herbert and T. Hesjedal. Calculation of the magnetic stray field of a uniaxial magnetic domain. *Journal of Applied Physics*, 97(7):074504, 2005.

[54] Kamran Behnia. *Fundamentals of thermoelectricity*. OUP Oxford, 2015.

[55] Muhammad Ikhlas, Takahiro Tomita, Takashi Koretsune, Michi-To Suzuki, Daisuke Nishio-Hamane, Ryotaro Arita, Yoshichika Otani, and Satoru Nakatsuji. Large anomalous Nernst effect at room temperature in a chiral antiferromagnet. *Nature Physics*, 13(11):1085–1090, 2017.

[56] Di Xiao, Yugui Yao, Zhong Fang, and Qian Niu. Berry-Phase Effect in Anomalous Thermoelectric Transport. *Physical Review Letters*, 97(2):026603, 2006.

[57] Naoto Nagaosa, Jairo Sinova, Shigeki Onoda, A. H. MacDonald, and N. P. Ong. Anomalous Hall effect. *Reviews of Modern Physics*, 82(2):1539–1592, 2010.

[58] Linchao Ding, Jahyun Koo, Liangcai Xu, Xiaokang Li, Xiufang Lu, Lingxiao Zhao, Qi Wang, Qiangwei Yin, Hechang Lei, Binghai Yan, Zengwei Zhu, and Kamran Behnia. Intrinsic Anomalous Nernst Effect Amplified by Disorder in a Half-Metallic Semimetal. *Physical Review X*, 9(4):041061, 2019.

[59] Tian Liang, Jingjing Lin, Quinn Gibson, Tong Gao, Max Hirschberger, Minhao Liu, R. J. Cava, and N. P. Ong. Anomalous Nernst Effect in the Dirac Semimetal Cd_3As_2. *Physical Review Letters*, 118(13):136601, 2017.

[60] Satya N. Guin, Kaustuv Manna, Jonathan Noky, Sarah J. Watzman, Chenguang Fu, Nitesh Kumar, Walter Schnelle, Chandra Shekhar, Yan Sun, Johannes Gooth, and Claudia Felser. Anomalous Nernst effect beyond the magnetization scaling relation in the ferromagnetic Heusler compound Co2MnGa. *NPG Asia Materials*, 11(1):16, 2019.

[61] Y. Shiomi, N. Kanazawa, K. Shibata, Y. Onose, and Y. Tokura. Topological Nernst effect in a three-dimensional skyrmion-lattice phase. *Physical Review B*, 88(6):064409, 2013.

[62] Max Hirschberger, Leonie Spitz, Takuya Nomoto, Takashi Kurumaji, Shang Gao, Jan Masell, Taro Nakajima, Akiko Kikkawa, Yuichi Yamasaki, Hajime Sagayama, Hironori Nakao, Yasujiro Taguchi, Ryotaro Arita, Taka-hisa Arima, and Yoshinori Tokura. Topological Nernst Effect of the Two-Dimensional Skyrmion Lattice. *Physical Review Letters*, 125(7):076602, 2020.

[63] Linda Ye, Mingu Kang, Junwei Liu, Felix von Cube, Christina R. Wicker, Takehito Suzuki, Chris Jozwiak, Aaron Bostwick, Eli Rotenberg, David C. Bell, Liang Fu, Riccardo Comin, and Joseph G. Checkelsky. Massive Dirac fermions in a ferromagnetic kagome metal. *Nature*, 555(7698):638–642, 2018.

[64] Qianheng Du, Myung-Geun Han, Yu Liu, Weijun Ren, Yimei Zhu, and Cedomir Petrovic. Room-Temperature Skyrmion Thermopower in Fe3Sn2. *Advanced Quantum Technologies*, n/a(n/a):2000058, 2020.

[65] Zhipeng Hou, Weijun Ren, Bei Ding, Guizhou Xu, Yue Wang, Bing Yang, Qiang Zhang, Ying Zhang, Enke Liu, Feng Xu, Wenhong Wang, Guangheng Wu, Xixiang Zhang, Baogen Shen, and Zhidong Zhang. Observation of Various and Spontaneous Magnetic Skyrmionic Bubbles at Room Temperature in a Frustrated Kagome Magnet with Uniaxial Magnetic Anisotropy. *Advanced Materials*, 29(29):1701144, 2017.

[66] F. Caglieris, C. Wuttke, S. Sykora, V. Süss, C. Shekhar, C. Felser, B. Büchner, and C. Hess. Anomalous Nernst effect and field-induced Lifshitz transition in the Weyl semimetals TaP and TaAs. *Physical Review B*, 98(20):201107, 2018.

[67] M. N. Chernodub, Alberto Cortijo, and María A. H. Vozmediano. Generation of a Nernst Current from the Conformal Anomaly in Dirac and Weyl Semimetals. *Physical Review Letters*, 120(20):206601, 2018.

[68] Mingu Kang, Linda Ye, Shiang Fang, Jhih-Shih You, Abe Levitan, Minyong Han, Jorge I. Facio, Chris Jozwiak, Aaron Bostwick, Eli Rotenberg, Mun K. Chan, Ross D. McDonald, David Graf, Konstantine Kaznatcheev, Elio Vescovo, David C. Bell, Efthimios Kaxiras, Jeroen van den Brink, Manuel Richter, Madhav Prasad Ghimire, Joseph G. Checkelsky, and Riccardo Comin. Dirac fermions and flat bands in the ideal kagome metal FeSn. *Nature Materials*, 19(2):163–169, 2020.

[69] Enke Liu, Yan Sun, Nitesh Kumar, Lukas Muechler, Aili Sun, Lin Jiao, Shuo-Ying Yang, Defa Liu, Aiji Liang, Qiunan Xu, Johannes Kroder, Vicky Süß, Horst Borrmann, Chandra Shekhar, Zhaosheng Wang, Chuanying Xi, Wenhong Wang, Walter Schnelle, Steffen Wirth, Yulin Chen, Sebastian T. B. Goennenwein, and Claudia Felser. Giant anomalous Hall effect in a ferromagnetic kagome-lattice semimetal. *Nature Physics*, 14(11):1125–1131, 2018.

[70] L. A. Fenner, A. A. Dee, and A. S. Wills. Non-collinearity and spin frustration in the itinerant kagome ferromagnet Fe3Sn2. *Journal of Physics: Condensed Matter*, 21(45):452202, 2009.

[71] R. Franz and G. Wiedemann. Ueber die Wärme-Leitungsfähigkeit der Metalle. *Annalen der Physik*, 165(8):497–531, 1853.

[72] M. Jonson and G. D. Mahan. Mott's formula for the thermopower and the Wiedemann-Franz law. *Physical Review B*, 21(10):4223–4229, 1980.

[73] P. W. Bridgman. The Connections between the Four Transverse Galvanomagnetic and Thermomagnetic Phenomena. *Physical Review*, 24(6):644–651, 1924.

[74] Neeraj Kumar, Y. Soh, Yihao Wang, and Y. Xiong. Magnetotransport as a diagnostic of spin reorientation: Kagome ferromagnet as a case study. *Physical Review B*, 100(21):214420, 2019.

[75] Michał Papaj and Liang Fu. Enhanced anomalous Nernst effect in disordered Dirac and Weyl materials. *Enhanced anomalous Nernst effect in disordered Dirac and Weyl materials, arXiv:2008.07974*, 2020.

[76] Akito Sakai, Yo Pierre Mizuta, Agustinus Agung Nugroho, Rombang Sihombing, Takashi Koretsune, Michi-To Suzuki, Nayuta Takemori, Rieko Ishii, Daisuke Nishio-Hamane, Ryotaro Arita, Pallab Goswami, and Satoru Nakatsuji. Giant anomalous Nernst effect and quantum-critical scaling in a ferromagnetic semimetal. *Nature Physics*, 14(11):1119–1124, 2018.

[77] Christoph Wuttke, Federico Caglieris, Steffen Sykora, Francesco Scaravaggi, Anja U. B. Wolter, Kaustuv Manna, Vicky Süss, Chandra Shekhar, Claudia Felser, Bernd Büchner, and Christian Hess. Berry curvature unravelled by the anomalous Nernst effect in Mn_3Ge. *Physical Review B*, 100(8):085111, 2019.

[78] Haiyang Yang, Wei You, Jialu Wang, Junwu Huang, Chuanying Xi, Xiaofeng Xu, Chao Cao, Mingliang Tian, Zhu-An Xu, Jianhui Dai, and Yuke Li. Giant anomalous Nernst effect in the magnetic Weyl semimetal $Co_3Sn_2S_2$. *Physical Review Materials*, 4(2):024202, 2020.

[79] Liangcai Xu, Xiaokang Li, Linchao Ding, Taishi Chen, Akito Sakai, Benoît Fauqué, Satoru Nakatsuji, Zengwei Zhu, and Kamran Behnia. Anomalous transverse response of Co_2MnGa and universality of the room-temperature $\alpha_{ij}^A/\sigma_{ij}^A$ ratio across topological magnets. *Physical Review B*, 101(18):180404, 2020.

[80] Liangcai Xu, Xiaokang Li, Xiufang Lu, Clément Collignon, Huixia Fu, Jahyun Koo, Benoît Fauqué, Binghai Yan, Zengwei Zhu, and Kamran Behnia. Finite-temperature violation of the anomalous transverse Wiedemann-Franz law. *Science Advances*, 6(17):eaaz3522, 2020.

[81] Hang Li, Bei Ding, Jie Chen, Zefang Li, Zhipeng Hou, Enke Liu, Hongwei Zhang, Xuekui Xi, Guangheng Wu, and Wenhong Wang. Large topological Hall effect in a geometrically frustrated kagome magnet Fe3Sn2. *Applied Physics Letters*, 114(19):192408, 2019.

[82] Yangmu Li, Qi Wang, Lisa DeBeer-Schmitt, Zurab Guguchia, Ryan D. Desautels, Jia-Xin Yin, Qianheng Du, Weijun Ren, Xinguo Zhao, Zhidong Zhang, Igor A. Zaliznyak, Cedomir Petrovic, Weiguo Yin, M. Zahid Hasan, Hechang Lei, and John M. Tranquada. Magnetic-Field Control of Topological Electronic Response near Room Temperature in Correlated Kagome Magnets. *Phys. Rev. Lett.*, 123:196604, Nov 2019.

[83] Su Do Yi, Shigeki Onoda, Naoto Nagaosa, and Jung Hoon Han. Skyrmions and anomalous Hall effect in a Dzyaloshinskii-Moriya spiral magnet. *Physical Review B*, 80(5):054416, 2009.

[84] Kamran Behnia and Hervé Aubin. Nernst effect in metals and superconductors: a review of concepts and experiments. *Reports on Progress in Physics*, 79(4):046502, 2016.

[85] C. Franz, F. Freimuth, A. Bauer, R. Ritz, C. Schnarr, C. Duvinage, T. Adams, S. Blügel, A. Rosch, Y. Mokrousov, and C. Pfleiderer. Real-Space and Reciprocal-Space Berry Phases in the Hall Effect of $Mn_{1-x}Fe_xSi$. *Physical Review Letters*, 112(18):186601, 2014.

[86] Xiuzhen Yu, Fumitaka Kagawa, Shinichiro Seki, Masashi Kubota, Jan Masell, Fehmi S. Yasin, Kiyomi Nakajima, Masao Nakamura, Masashi Kawasaki, Naoto Nagaosa, and Yoshinori Tokura. Real-space observations of 60-nm skyrmion dynamics in an insulating magnet under low heat flow. *Nature Communications*, 12(1):5079, 2021.

[87] Charles Kittel and Paul McEuen. *Introduction to solid state physics*, volume 8. Wiley New York, 1996.

[88] Evgenii Mikhailovich Lifshitz and Lev Petrovich Pitaevskii. *Statistical physics: theory of the condensed state*, volume 9. Elsevier, 2013.

[89] A. K. Bera, B. Lake, F. H. L. Essler, L. Vanderstraeten, C. Hubig, U. Schollwöck, A. T. M. N. Islam, A. Schneidewind, and D. L. Quintero-Castro. Spinon confinement in a quasi-one-dimensional anisotropic Heisenberg magnet. *Physical Review B*, 96(5):054423, 2017.

[90] R. Coldea, D. A. Tennant, A. M. Tsvelik, and Z. Tylczynski. Experimental Realization of a 2D Fractional Quantum Spin Liquid. *Physical Review Letters*, 86(7):1335–1338, 2001.

[91] L. D. Faddeev and L. A. Takhtajan. What is the spin of a spin wave? *Physics Letters A*, 85(6):375–377, 1981.

[92] F. D. M. Haldane. "Spinon gas" description of the S=1/2 Heisenberg chain with inverse-square exchange: Exact spectrum and thermodynamics. *Physical Review Letters*, 66(11):1529–1532, 1991.

[93] Michael Karbach, Gerhard Müller, A. Hamid Bougourzi, Andreas Fledderjohann, and Karl-Heinz Mütter. Two-spinon dynamic structure factor of the one-dimensional s=1/2 Heisenberg antiferromagnet. *Physical Review B*, 55(18):12510–12517, 1997.

[94] B. Lake, D. A. Tennant, and S. E. Nagler. Novel Longitudinal Mode in the Coupled Quantum Chain Compound KCuF3. *Physical Review Letters*, 85(4):832–835, 2000.

[95] Bella Lake, D. Alan Tennant, Chris D. Frost, and Stephen E. Nagler. Quantum criticality and universal scaling of a quantum antiferromagnet. *Nature Materials*, 4(4):329–334, 2005.

[96] Bella Lake, Alexei M. Tsvelik, Susanne Notbohm, D. Alan Tennant, Toby G. Perring, Manfred Reehuis, Chinnathambi Sekar, Gernot Krabbes, and Bernd Büchner. Confinement of fractional quantum number particles in a condensed-matter system. *Nature Physics*, 6(1):50–55, 2010.

[97] Martin Mourigal, Mechthild Enderle, Axel Klöpperpieper, Jean-Sébastien Caux, Anne Stunault, and Henrik M. Rønnow. Fractional spinon excitations in the quantum Heisenberg antiferromagnetic chain. *Nature Physics*, 9:435, 2013.

[98] S. E. Nagler, D. A. Tennant, R. A. Cowley, T. G. Perring, and S. K. Satija. Spin dynamics in the quantum antiferromagnetic chain compound KCuF3. *Physical Review B*, 44(22):12361–12368, 1991.

[99] Marcin Raczkowski and Fakher F. Assaad. Spinon confinement: Dynamics of weakly coupled Hubbard chains. *Physical Review B*, 88(8):085120, 2013.

[100] D. Alan Tennant, Stephen E. Nagler, Detmar Welz, Gen Shirane, and Kazuyoshi Yamada. Effects of coupling between chains on the magnetic excitation spectrum of KCuF3. *Physical Review B*, 52(18):13381–13389, 1995.

[101] A. Zheludev, M. Kenzelmann, S. Raymond, T. Masuda, K. Uchinokura, and S. H. Lee. Spin dynamics in the quasi-one-dimensional S=1/2 antiferromagnet BaCu2Si2O7. *Physical Review B*, 65(1):014402, 2001.

[102] A. Zheludev, M. Kenzelmann, S. Raymond, E. Ressouche, T. Masuda, K. Kakurai, S. Maslov, I. Tsukada, K. Uchinokura, and A. Wildes. Energy Separation of Single-Particle and Continuum States in an S = 1/2 Weakly Coupled Chains Antiferromagnet. *Physical Review Letters*, 85(22):4799–4802, 2000.

[103] S. K. Satija, J. D. Axe, R. Gaura, R. Willett, and C. P. Landee. Neutron scattering studies of spin waves in one-dimensional Heisenberg ferromagnet $CuCl_2 \cdot$ DMSO (dimethyl sulfoxide). *Phys. Rev. B*, 25:6855–6859, Jun 1982.

[104] Minoru Takahashi, Philippe Turek, Yasuhiro Nakazawa, Masafumi Tamura, Kiyokazu Nozawa, Daisuke Shiomi, Masayasu Ishikawa, and Minoru Kinoshita. Discovery of a quasi-1D organic ferromagnet, p-NPNN. *Physical Review Letters*, 67(6):746–748, 1991.

[105] J. Bardeen, L. N. Cooper, and J. R. Schrieffer. Microscopic Theory of Superconductivity. *Physical Review*, 106(1):162–164, 1957.

[106] D. J. Scalapino. A common thread: The pairing interaction for unconventional superconductors. *Reviews of Modern Physics*, 84(4):1383–1417, 2012.

[107] A. Neubauer, C. Pfleiderer, B. Binz, A. Rosch, R. Ritz, P. G. Niklowitz, and P. Böni. Topological Hall Effect in the A Phase of MnSi. *Physical Review Letters*, 102(18):186602, 2009.

[108] Z. Y. Zhao, H. L. Che, R. Chen, J. F. Wang, X. F. Sun, and Z. Z. He. Magnetism study on a triangular lattice antiferromagnet $Cu_2(OH)_3Br$. *Journal of Physics-Condensed Matter*, 31(27), 2019.

[109] X. G. Zheng, T. Yamashita, M. Hagihala, M. Fujihala, and T. Kawae. Magnetic transitions in botallackite-structure $Cu_2(OH)_3Br$ and Cu2(OH)3I. *Physica B: Condensed Matter*, 404(5):680–682, 2009.

[110] Juan Rodríguez-Carvajal. Recent advances in magnetic structure determination by neutron powder diffraction. *Physica B: Condensed Matter*, 192(1):55–69, 1993.

[111] Igor A Zaliznyak, Andrei T. Savici, V. Ovidiu Garlea, Barry Winn, Uwe Filges, John Schneeloch, John M. Tranquada, Genda Gu, Aifeng Wang, and Cedomir Petrovic. Polarized neutron scattering on HYSPEC: the HYbrid SPECtrometer at SNS. *Journal of Physics: Conference Series*, 862:012030, jun 2017.

[112] S. Toth and B. Lake. Linear spin wave theory for single-Q incommensurate magnetic structures. *Journal of Physics-Condensed Matter*, 27(16), 2015.

[113] D. I. Khomskii. Role of Orbitals in the Physics of Correlated Electron Systems. *Physica Scripta*, 72(5):CC8–CC14, 2005.

[114] Masanori Kohno, Oleg A. Starykh, and Leon Balents. Spinons and triplons in spatially anisotropic frustrated antiferromagnets. *Nature Physics*, 3:790, 2007.

[115] Martin Bercx, Florian Goth, Johannes Stephan Hofmann, and Fakher F Assaad. The ALF (Algorithms for Lattice Fermions) project release 1.0. Documentation for the auxiliary field quantum Monte Carlo code. *SciPost Phys.*, 3(arXiv: 1704.00131):013, 2017.

[116] F. Assaad and H. Evertz. *Computational Many-Particle Physics*, volume 739 of *Lecture Notes in Physics*. Springer-Verlag, Berlin, 2008.

[117] R. Blankenbecler, D. J. Scalapino, and R. L. Sugar. Monte Carlo calculations of coupled boson-fermion systems. I. *Physical Review D*, 24(8):2278–2286, 1981.

[118] D. J. Scalapino, Y. Imry, and P. Pincus. Generalized Ginzburg-Landau theory of pseudo-one-dimensional systems. *Physical Review B*, 11(5):2042–2048, 1975.

[119] Daichi Hirobe, Masahiro Sato, Takayuki Kawamata, Yuki Shiomi, Ken-ichi Uchida, Ryo Iguchi, Yoji Koike, Sadamichi Maekawa, and Eiji Saitoh. One-dimensional spinon spin currents. *Nature Physics*, 13(1):30–34, 2017.